Optical thin film stacks integrating spectral and angular control of solar energy and thermal radiation

University of Technology Sydney

Maryna Bilokur

5 August 2019

Sydney, Australia

STATEMENT OF ORIGINAL AUTHORSHIP

I, Maryna Bilokur, declare that this thesis is submitted in fulfilment of the requirements for the award of PhD degree, in the School of Mathematical and Physical Sciences, Faculty of Science, University of Technology Sydney. This thesis is wholly my own work unless otherwise referenced or acknowledged. In addition, I certify that all information sources and literature used are indicated in the thesis. This document has not been submitted for qualifications at any other academic institution. This research is supported by the Australian Government Research Training Program.

Production Note:
Signature removed prior to publication.

Date: August 5, 2019

ACKNOWLEDGEMENTS

I would like to express my special appreciation and thanks to my supervisors Prof. Michael Cortie, Dr Matthew Arnold, Dr Angus Gentle and Prof. Geoff Smith for providing me a unique opportunity to become a part of their research team and their on-going support during these years. I deeply appreciate the experience I have received working closely with them and the professional knowledge and expertise they have shared with me, which helped me to grow a lot as a research scientist! A special thanks to Angus Gentle and Geoff McCredie for the thorough technical training and assistance they have provided, making the lab environment a very professional and friendly place. A very big thank to Geoff Smith for his stimulating discussions and a great deal of encouragement in the process of growing my scientific expertise. He shared his wealth of experience with me during our discussions and I have learnt a lot from him! A very big thank to Matthew Arnold for his encouragement, constructive criticism and guidance through my PhD journey. And, finally, I am very grateful to my principal supervisor, Michael Cortie, for his constant support and sympathy, being a highly professional academic advisor, who helped me all the time during my research and thesis writing. Also, I would like to thank Katie McBeam and Mark Berkahn for their assistance with the SEM and XRD training.

A special and sincere gratitude to Dr Marie Manidis for her tremendous moral support and becoming a good friend of mine, who lit up the moments of my PhD life with her generosity, sincerity, sharp intelligence and just a wonderful personality.

A special thanks to my family, sister, mom and dad, my godfather and my brother-in-law for being with me all these time despite separation of thousands of kilometers and being an infinite source of love, inspiration, support and strength and encouraging my scientific journey.

Also, I thank my fellow labmates and colleagues for becoming the part of my PhD journey and being very supportive during these times, sharing their experience and creating a family like environment at the work-place we shared altogether: Marc Gali, Aaron Colusso, Matthew Tai, Sujeewa de Silva, Chris Wolf, Igor Aharonovich, Daniel Pasin, Alba Santin Garcia, Mahmoud El Safadi, Smith Panicer, Minh Nguyen, Blake Regan, Daniel Totonjian, Matthew Cappaddona, Behnaam Mlk, John Scott, Chris Elbadawi, Mehran Kianinia, Noah Mendelson, Jacqueline Loyola-Echeverria, Mark Barash, Anirudha Saha, Olivier Lee, James Bishop, Trong Toan Tran.

THESIS FORMAT

The thesis has been prepared using conventional structure, comprised of a series of chapters. There are seven chapters with an abstract outlining the main results that have been achieved in the conducted research. Chapter 1 is dedicated to an introduction into the topic of the research (concentrated solar thermal applications), with a review of the principal physical phenomena behind photo-thermal conversion and spectrally-selective mechanisms to enhance solar-to-heat conversion. The chapter is concluded with the literature review, analysing the spectrally-selective surfaces developed to date and the key problems they face if applied in high temperature concentrated solar thermal applications.

Chapter 2 revises the methodology that has been used, explaining the principal work and mechanisms of device operation and physical processes behind it.

Chapter 3, Chapter 4 and Chapter 5 describe the main results that have been achieved during my PhD research. Chapter 3 describes new findings in the family of spectrally-selective surfaces based on noble metal cermets. Chapter 4 reflects on the semiconductor based approach of the solar absorber coatings using TiAlN family as the main solar absorbing component. Chapter 5 demonstrates a novel spectrally-selective solar absorber that is comprised of a multilayer stack with two Ta:SiO_2 cermets.

Chapter 6 analyses the deposition conditions of one of the main components of the spectrally-selective surface, an infrared back reflector leading to the highest possible ramp up in reflectance starting from 2500 nm.

Finally, Chapter 7 is devoted to a discussion and conclusion of the main findings with some overlook for the future work.

LIST OF PUBLICATIONS

***M. BILOKUR*; A. GENTLE; M. ARNOLD; M. B. CORTIE; G. B. SMITH (2017)** High temperature optically stable spectrally-selective Ti1-xAlxN-based multilayer coating for concentrated solar thermal applications. *Solar energy materials and solar cells*. Volume 200, 15 September 2019, 109964. Available from: https://www.sciencedirect.com/science/article/pii/S0927024819302934 [Accessed: 23 July 2019].

***M. BILOKUR*; A. GENTLE; M. ARNOLD; M. B. CORTIE; G. B. SMITH (2017)** High Temperature Spectrally Selective Solar Absorbers Using Plasmonic $AuAl_2$:AlN Nanoparticle Composites. *Solar RRL*. 1(10). WILEY-VCH Verlag GmbH & Co. KGaA, Berlin, Germany. Available from: http://onlinelibrary.wiley.com/doi/10.1002/solr.201700092/full [Accessed: 7 September 2017].

***M. BILOKUR*; A. GENTLE; M. ARNOLD; M. B. CORTIE; G. B. SMITH (2017)** An advanced plasmonic cermet solar absorber for high temperature solar energy conversion applications. In – "SPIE 10356, Nanostructured Thin Films X, 103560C", San Diego, USA, 30 August 2017. Available from: https://www.spiedigitallibrary.org/conference-proceedings-of-spie/10356/103560C/An-advanced-plasmonic-cermet-solar-absorber-for-high-temperature-solar/10.1117/12.2273598.short [Accessed: 30 August 2017.].

***M. BILOKUR*; A. GENTLE; M. ARNOLD; M. B. CORTIE; G. B. SMITH (2015)** Optical properties of refractory TiN, AlN and (Ti,Al)N coatings. In – "*SPIE 9668, Micro+Nano Materials, Devices, and Systems*", Sydney, Australia, December 7-9. University of Sydney. Available from: https://opus.lib.uts.edu.au/bitstream/10453/43924/1/BilokurSPIE9668.pdf [Accessed: January 2016].

CONTENTS

LIST OF ILLUSTRATIONS AND TABLES

Abstract

The objective of this project is to enhance the efficiency of photo-thermal conversion by improving the optical and other properties of solar-absorbing surfaces. Designing a suitable coating for these surfaces involves a delicate balance between thermal stability, reflectance and emittance. As an added complication, it is necessary to have a coating with a spectral response that switches from highly absorptive in the visible and near-IR range to reflective at longer wavelengths. Despite extensive prior investigations in this area, there are still several problems that remained unsolved — in particular the maintenance of structural integrity and optical response of solar absorbers operating at higher temperatures (>500ºC). The results of the present work are highly relevant to various kinds of high temperature concentrated solar power (CSP) applications as well as to thermo-photovoltaic (TPV) systems.

A number of advanced new spectrally-selective solar absorbers: Al/AlN/Au-$AuAl_2$:AlN/AlN/SiO_2, Al/AlN/Au-$AuAl_2$:AlN/AlN/ Au-$AuAl_2$:AlN/AlN/SiO_2, Pt/AlN/TiAlN/ AlN/SiO_2, Pt/Ta:SiO_2/Ta:SiO_2/AlN/SiO_2 and Ta/Ta:SiO_2/ Ta:SiO_2/AlN/SiO_2 were investigated. All were produced by magnetron sputtering, and their optical properties and thermal stability assessed.

This work has shown that the Au-based solar absorbing structures are strongly oxidation-resistant, however, their exploitation in CSP applications is currently limited due to coarsening and agglomeration of the Au inclusions in the dielectric host temperatures greater than 400ºC. A solution to this problem is proposed : the Au nanoparticles in the cermet layer are allowed to alloy with Al. This converts them to the intermetallic compound $AuAl_2$, which is considerably more resistant to coarsening than pure gold. This was achieved by an introduction of the Al substrate to serve both as an IR-reflecting layer and as a source of the Al species to form more structurally and temperature stable $AuAl_2$ nanoparticles in the AlN host. The alloying process was thermally induced at 200ºC and was finalised at 500ºC, where alloying of all Au inclusions present in the matrix was achieved. The resultant new structure was able to endure 168 hours annealing in vacuum at 500ºC without major change. Such stability has apparently not been achieved before for Au-based solar absorbers. Furthermore, the $AuAl_2$ formation was shown to be also beneficial for the solar absorptance (α_s) enhancement, leading to an increase in α_s by 3%, from its initial 92% to a final 95%, while preserving low emittance.

Spectrally-selective coatings based on the$Ti_xAl_{1-x}N$ system were also considered due to their known diffusion barrier properties, high thermal tolerance, and very suitable optical properties. The composition of $Ti_xAl_{1-x}N$, (effectively, the Ti/Al ratio) was selected to achieve a maximized solar absorptance of the overall stack. A tandem absorber, which included top anti-reflective layers, was tested on a stainless-steel substrate in order to see how the stack design would serve in parabolic trough-based power plants that used stainless steel pipe to carry the heat-transfer fluid. The diffusion of the Fe present in stainless steel into the coating is known to normally start at 600ºC but this was successfully suppressed in the present work by an application of an AlN diffusion barrier. The whole $Ti_xAl_{1-x}N$-based stack, despite some structural modifications upon heating up to 900ºC, preserved its optical integrity with solar absorptance remaining unchanged at 92%.

Finally, a new algorithm for designing a nearly ideal cermet-based spectrally-selective absorber was developed. This enabled achievement of α_s> 97%. There are only a few structures known to absorb solar energy with α_s in the 97-98% range, however, their optical performance is degraded in the range 250ºC-500ºC due to surface oxidation, diffusion of the back reflector into the coating, shape and/or phase transformation of the nanoparticles. The result may be a significant drop in solar absorptance down to 84%. The new algorithm was exploited in the present project to design a novel spectrally-selective coating, the heart of which was composed of two absorbing Ta:SiO_2 layers with different Ta content, which showed not only an efficient light absorptance with α_s = 97.6%, but also preservation of its value up to 900ºC with simultaneously improved spectrally-selective performance due to recrystallization of the Pt or Ta back-reflectors. These effects lowered thermal emittance to 0.04 and 0.15 from initial values of 0.18 and 0.21, respectively. The Ta:SiO_2 cermet-based absorber on a Pt reflector showed good thermal stability up to 1000ºC, with a minor solar absorptance reduction to 95%, but high enough for an enhanced photo-thermal conversion. This would appear to be an unprecedented degree of stability at 1000°Ç for a cermet-based solar absorber.

In summary, this project has resulted in the development of new stack designs for use in high temperature conversion devices. A new way of enhancing thermal stability in a Au-based coating has been discovered, and a new procedure for designing coatings demonstrated.

Chapter 1

Introduction

1.1 Introduction to solar thermal

The global energy system is facing inevitable changes. While the availability of cheap electricity has become essential for a modern high-tech economy, there are associated problems due to environmental pollution, heavy exploitation of traditional but finite energy sources such as coal, oil and gas, and generation of CO_2 (a greenhouse gas) leading to a rise in global temperature, including of the oceans.

Furthermore, a constant increase in the world's population, increasing economic development and the urbanization phenomenon is associated with growing consumption of energy sources. According to Figure 1.1, the world's energy consumption will increase by around 15-34% by the year 2040 [1]. It is almost universally accepted that there is an urgent need to replace traditional sources of energy with non-fossil or renewable alternatives.

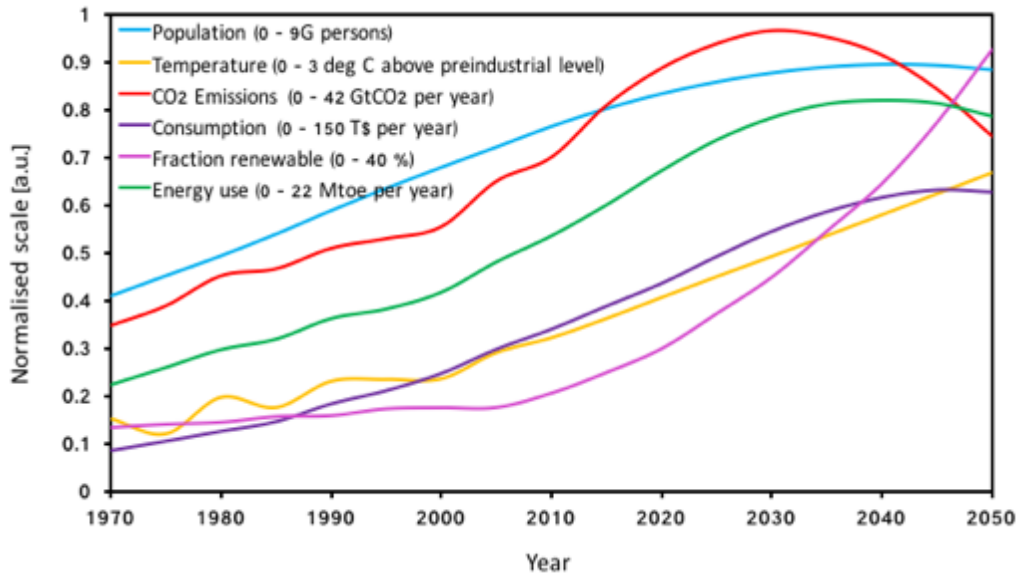

Figure 1.1 – A global forecast for the next forty years , based on spreadsheet data from [1]

The most abundant and consistent source of energy available on Earth is the UV-vis-NIR radiation generated by the Sun. Due to interior fusion processes resulting in a mass to energy conversion and further photon generation, the Sun acts as a perfect black body radiator emitting solar radiation in a particular wavelength range, which further on reaches the Earth and is distributed around the planet. The value of this irradiance depends on geometric factors, represented by latitude (the angular position relative to the Equator), declination angle (the Sun's angular position, which varies seasonally because of the Earth tilting and revolution across the Sun's orbit), hourly angle due to rotation of the Earth, and angle of incidence due to surface topography. Hence, the solar irradiation around the Earth exhibits a dynamic distribution and shows preferential areas of concentration, Figure 1.2. According to Figure 1.2, the areas with the most exposure to the Sun are Australia, West and South of United States and Europe, the majority of South America and Africa, west of Asia and countries close to the Equator. The solar flux in space above the Earth's atmosphere is close to 1361 W/m^2 but falls to an average midday peak of about 1000 W/m^2 at the Equator due to attenuation through the upper layers of the atmosphere [16]. Nevertheless, when the vast surface area of the Earth is considered, this is more than enough energy to satisfy growing world's energy demands.

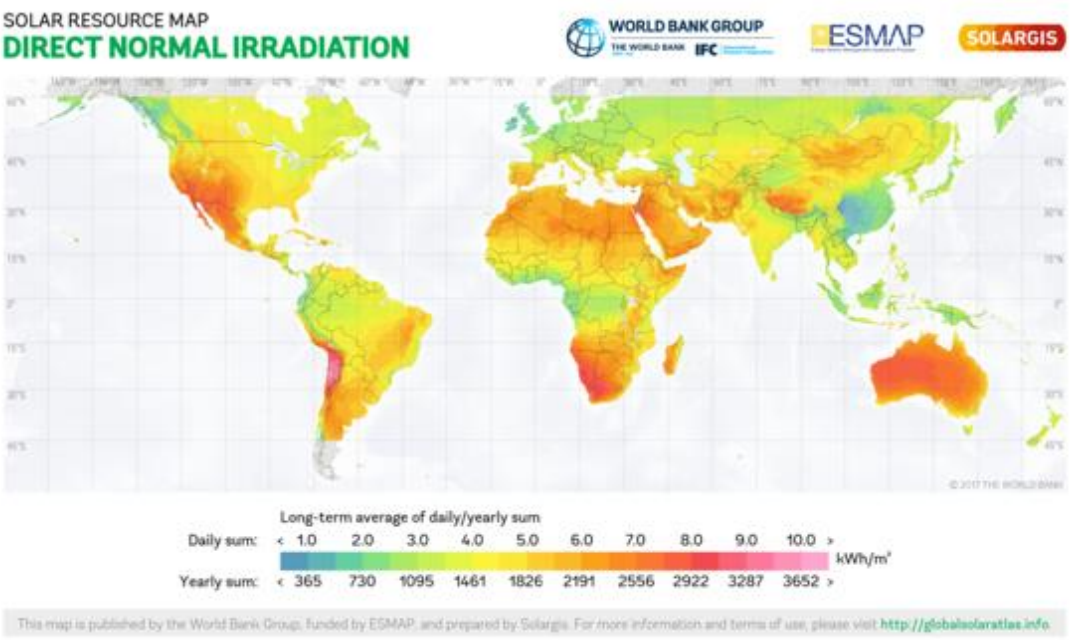

Figure 1.2 – Solar energy irradiance across the Earth retrieved from [2]

The countries currently leading in solar energy collection are China, Japan, Germany, United States and Italy. However, such territories as Australia, Africa and some parts of South America have a very high solar energy potential, but, unfortunately, are not well invested in a solar energy sector due to a well-established traditional energy industry and/or absence of government subsidies. In this connection, Australia has been widely criticized by commentators in the social media for not fully exploiting its solar potential, while being among top ten solar countries in the world in terms of potential [17].

At this stage, solar energy production around the planet is a growing industry, but solar still provides a much smaller proportion of energy needs than coal, oil and gas do. For 2016 the proportion of electricity produced by solar was close to 1% of the worldwide total although it reached 3.3% in Australia [18-20]. Fortunately, advances in solar science beyond simple photovoltaics offer the prospect of society having less reliance in future on the global non-renewable energy suppliers. In principle there could be total independence from the depleting fossil fuel resources and a significant reduction in cost. This is achievable by the means of a new generation of solar collecting systems. Concentrated parabolic troughs (CPTC), solar thermophotovoltaic (STPV) and solar thermoelectric generator (STEG) technologies (Figure 1.2) can produce electrical energy through an efficient use of the downwelling solar radiation at the Earth's surface, Figure 1.3. These technologies are currently being widely investigated and have the potential to bring efficient and cost effective transfer of sunlight into electricity through a heating stage. STPVs (Figure 1.3a) use concentrated solar energy absorbed by a spectrally selective solar absorbing coating transferred to a selective emitter heated to temperatures >>800°C to radiate photons in the wavelength range matching a photovoltaic module. Such construction does not require a conversion of mechanical energy into electricity like in CPTC and a direct heat to electricity conversion can be achieved. Likewise, STEG (Figure 1.3c) uses sunlight, a solar absorbing coating and thermoelectric generator to produce electricity. A straight conversion of heat into electricity is allowed by Seebeck effect, where electric carriers flow through the thermoelectric material due to a temperature gradient and then, if a thermoelectric module is connected in a circuit with electric load, electrical energy can be extracted. Contrary to STPV and STEG, concentrated solar thermal systems (Figure 1.3b) including CPTC use three-step process where sunlight is converted into heat, heat into mechanical energy and finally mechanical energy is converted into electricity. Of course these technologies are in competition with

conventional solar photovoltaics (PV), which operate using straightforward electricity generation from the Sun. In the present thesis, however, discussion will be mostly devoted to solar power technologies utilizing concentrated sunlight, and especially to the development of materials with the right optical materials for concentrated solar power systems, in particular for CPTCs.

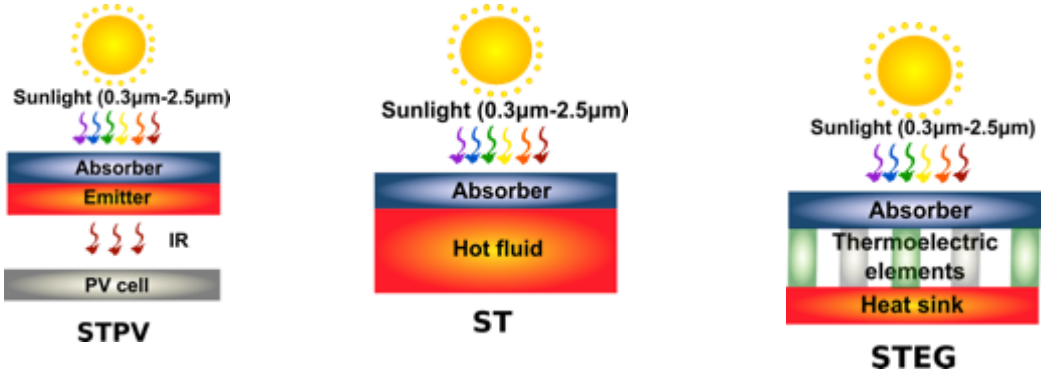

a) b) c)

Figure 1.3 - Harnessing of solar energy through solar thermal conversion through a) solar thermophotovoltaics b) solar thermal c) solar thermoelectric generation

One of the biggest advantages of concentrated solar power systems is simplicity in building the solar plant on site, production of both heat and electrical power, scalability, opportunity for cost reduction with an increase in plant size and capacity [21, 22]. CSP plants use direct solar irradiation and hence cannot collect diffused light, contrary to the PV cells, where both direct and diffused solar radiation can be used for electricity generation. This puts a constraint on the location of a CSP. Desert areas with low cloud coverage are best for CSP. Another big advantage of CSP plants is that the heat energy can be stored relatively cheaply for about 24 hours, compared to expensive battery storage required for PV systems. This enables CSP plants to generate electricity even at cloudy or rainy weather and also at night, and the most importantly in the peak hours when the electricity consumption shows a higher demand.

There are four main types of CSP technologies that are commercially available. Depending on the light concentration technique, they can be represented as: 1) Parabolic trough collectors 2) Linear Fresnel reflectors 3) Parabolic dish 4) Solar tower, Figure 1.4.

Figure 1.4 – Types of concentrated solar power plants. a) Parabolic trough b) Linear Fresnel reflector c) Parabolic dish d) Solar power tower, photos are from reference [3] with the permission under the terms of the Creative Commons Attribution 3.0 License

Overall, there are two principal parts of the solar thermal concentrating systems, represented by *mirrors* concentrating sunlight onto a *receiver*. In its turn, depending on the design and geometrical assembly of the mirrors, the CSP configurations represented in Figure 1.3, can be further classified as 1) *line focusing* (parabolic trough, linear Fresnel reflector), where the solar energy is focused onto a linear receiver and 2) *point focusing* (parabolic dish, solar power tower), where the sunlight is focused onto a point receiver. Different concentration ratios of sunlight are used in order to achieve the target operational temperature range for each type of the CSP plant.

Solar power plants exploiting concentrating parabolic trough collectors (CPTC) are the most mature technology amongst the various CSP configurations. The CPTC includes reflectors (mirrors) curved into a parabolic trough (PT) to focus solar radiation onto a receiver, Figure 1.5. A receiver is represented by a metal pipe typically made of stainless steel carrying a heat transfer fluid (HTF) and enclosed in an evacuated glass tube in order to minimise convective heat transfer from the hot pipe. To facilitate the solar absorption process, the metal pipe is covered by a spectrally selective coating (SSC) which enables

it to heat the HTF to the temperature required for the further stages the power plant operation.

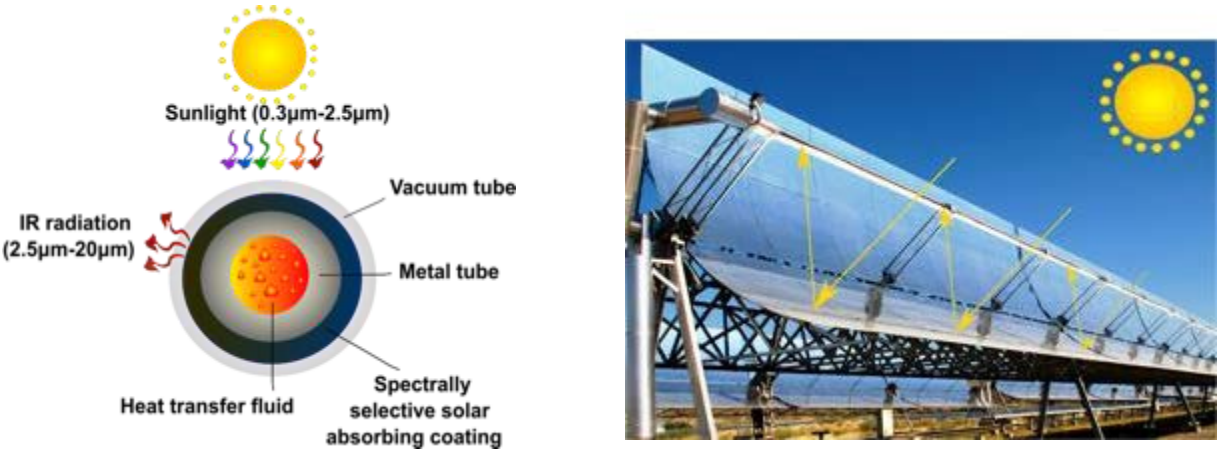

a) b)

Figure 1.5 – Parabolic trough collector. a) Schematic and b) a photo of parabolic trough solar power plant with arrows showing the principle of light focusing by mirrors

The overall process of the CSP operation based on PTs is reflected in Figure 1.6.

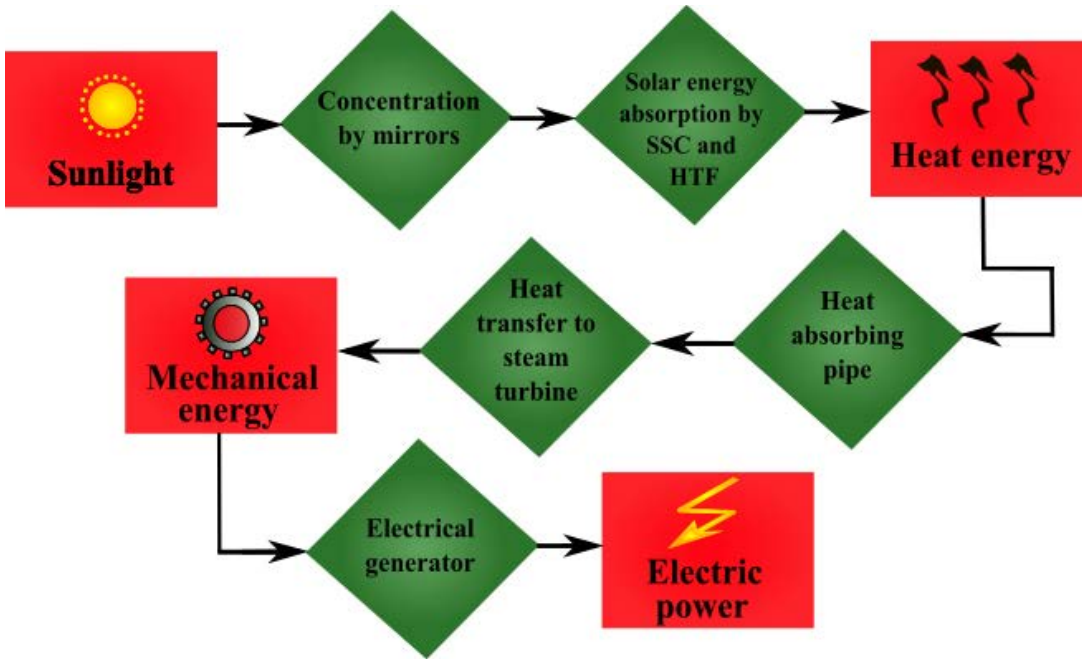

Figure 1.6 – Process diagram of CPTC solar power plant highlighting the key stages of solar to electricity conversion

The conversion of solar energy to electrical power starts with a concentration of solar radiation by the parabolic reflectors onto a receiver with a single-axis tracking. The energy is absorbed by the spectrally selective solar absorbing coating covering the metal pipe and passed to the HTF inside. Here, depending on the concentration factor, the fluid temperature can reach up to 500°C. For the CPTCs the concentration factor varies mainly between 30 and 100 suns, where each "sun" accounts for an average direct incident solar irradiation of 800 W/m^2. The HTF is typically a molten salt, liquid sodium, synthetic thermal oil or pressurized (non-condensable) gas.. After this, the collected heat is transferred into a steam-generator for high pressure super-heated steam generation to run a steam-turbine in combination with generator to produce electrical power, which further on is transferred to the electrical grid.

According to Figure 1.6, and the cycle description of the CSP PT plant, it can be seen that the fluid temperature plays one of the key roles for efficient electricity generation. Furthermore, efficiency of a heat engine taking heat from a high-temperature source (the Carnot efficiency) can be expressed as:

$$\eta_e = \frac{T_H - T_C}{T_H} \tag{1.1}$$

where η_e is efficiency of the steam engine, T_H is the temperature of the heat source and T_C is the temperature of the reservoir where the heat is released to.

Hence, it can be concluded, that the efficiency will never achieve 100%, but still can be enhanced if an optimal combination of T_H and T_C is achieved. In the current case, since T_C can be considered to be roughly the atmospheric temperature, efficiency can be improved by increasing T_H, the HTF temperature, which in its turn, is affected by the optical behavior and thermal stability of the solar absorbing coating on top of the metal tube.

Simultaneously, another factor, the re-radiation of thermal radiation away from the hot collector, should be considered. From Figure 1.7 it is seen that the collector efficiency decreases with a rise in temperature, but goes up with the concentration factor.

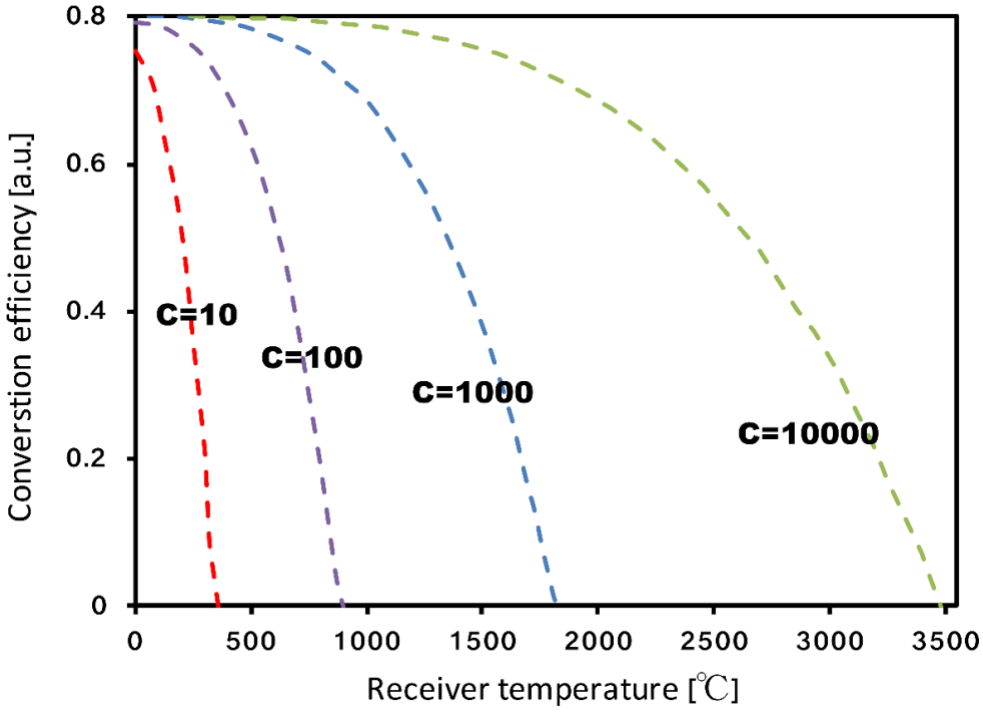

Figure 1.7 – Efficiency of a solar receiver in relation to fluid temperature and a concentration factor. Modified from [4]

Hence, it can be concluded that a balanced operating temperature should be found leading to a maximized efficiency of the whole system, which in its turn depends on both Carnot efficiency and efficiency of the solar receiver.

Lee *et al.* have examined this issue [5]. Their calculations reflect the optimum temperature of the solar collector leading to the maximum achievable efficiency of the overall system. Figure 1.8 shows that the heat engine efficiency can be continuously increased with a rise in temperature reaching about 50% at 1200°C. Contrary to this, the collector's efficiency keeps diminishing with temperature, however, it can be seen that the resultant efficiency as a factor of two components has a parabolic trend with a maximum power output at around *630°C*.

Additionally, according to Price and Kearny [21], the right selection of the solar absorbing coating with enhanced properties can reduce the electricity cost by more than 10% and this is only due to optimized performance of the coating, such as enhanced solar absorptance (2% electricity cost reduction), reduced thermal radiation (5% electricity cost reduction) and increased lifespan and reliability of the receiver tube due to reliable, age-and-oxidation resistant spectrally selective solar absorbing coating (SSSAC).

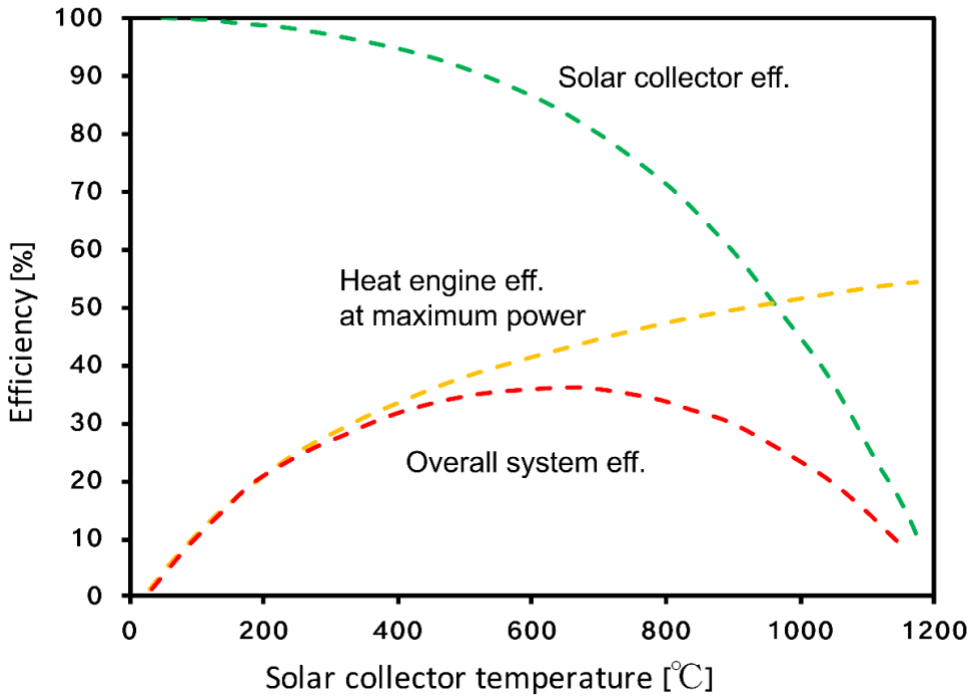

Figure 1.8 – The influence of solar collector temperature on efficiency of solar collector, heat engine and overall system with the concentration factor of C=1.52, calculated using Carnot equation (1.1). Modified from [5]

Taking into account the listed factors, the key requirements for the spectrally selective solar absorbing coating for the high temperature CSP can be defined in the following way and are represented in Figure 1.9.

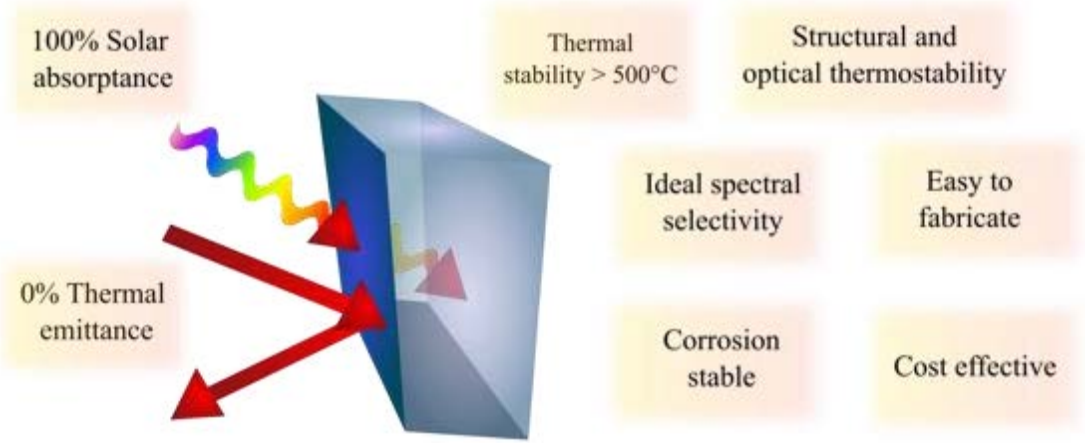

Figure 1.9 – Ideal spectrally selective solar absorbing coating for high temperature solar thermal applications

The ideal coating should harness the maximum amount of solar radiation while minimizing thermal emission to prevent re-radiation of the collected solar energy at higher temperatures. Since the CSP systems operate with a concentrated sunlight, where an absorber element gets to temperatures above 400°C, the next most important demand for a solar absorbing material is an ability to withstand elevated temperatures with a simultaneous preservation of a structure and optical response. In this way, the sunlight-to-heat conversion efficiency is maintained being a pivotal and necessary pathway towards electrical power generation, as was shown in Figure 1.6. Corrosion stability is required in order to prevent deterioration of the coating and minimize the environmental effect in case of the vacuum tube breakage in a solar collector. The solar absorbing coating should also be cost effective in order to reduce the final electricity price for the grid distribution. Hence, it implies that not only an improved optical response should be achieved, but also the fabrication process should be simplified and materials (e.g. metals and dielectrics) for the absorber components should not be expensive.

1.2 Physical background

1.2.1 Electromagnetic radiation

The electromagnetic spectrum is made up of electromagnetic waves (Figure 1.10) of all physically possible frequencies, starting from the shortest wavelengths having the highest frequencies, the length of which can be much smaller than an angstrom (e.g. gamma-rays) and ending up with the longest waves with the lowest frequencies (e.g. radio waves of hundreds of meters length). The spectrum can be divided in the following way starting from the shortest wavelengths: gamma rays (<0.01nm), X-rays (0.01nm – 10nm), ultraviolet (10nm – 400nm), visible (390 nm – 750 nm), near-infrared (750 nm – 2500 nm), mid-far-infrared (2500 nm – 1 mm), microwave (1mm – 1m), radiowave (1m – 1km).

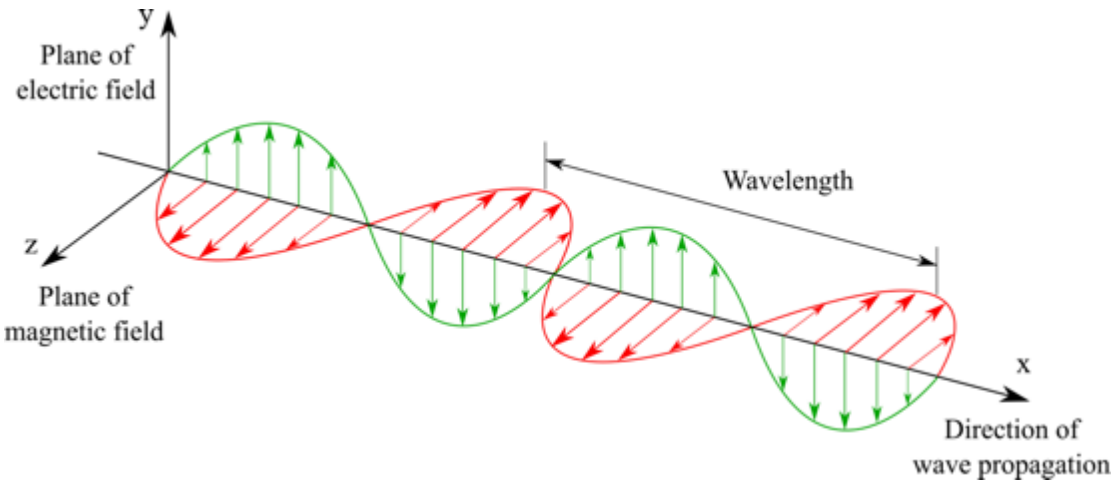

Figure 1.10 – A schematic representing two components of electromagnetic wave (electric and magnetic) propagating along *x* axes

The relation between frequency and the length of the wave can be represented in the following form:

$$\lambda = \frac{c}{f} \tag{1.2}$$

Where c is a speed of light in a medium and c = 2.99792458×10^8 m/s for electromagnetic waves travelling in the vacuum.

It is well known that all objects above absolute zero temperature (-273.15ºC) continuously emit electromagnetic radiation due to a continuous random motion of the particles. A black body (BB) is a theoretical physical model for a surface that can perfectly absorb or emit a maximum of incident electromagnetic energy. The intensity and position of the emitted radiation depends only on the object's temperature. The intensity of the radiation emitted by the BB and its wavelength distribution is described by Plank's law:

$$P_\lambda(T) = \frac{2hc^2}{\lambda^5} \frac{1}{e^{\frac{hc}{\lambda k_B T}} - 1} \tag{1.3}$$

Where P is power density emitted by a BB as a function of wavelength (λ), measured in W/m^2/nm; h is Planck's constant, k_B is Boltzmann's constant, c is a speed of light, T is an absolute temperature of the BB.

Figure 1.11 is based on the Planck's formula and shows distributions of emitted radiation by the BB at different temperatures. It can be noticed that the curve describing the irradiation by a BB at 4500ºC lies below the radiation spectrum at 5000ºC, followed by 5500ºC, 6000ºC and 6500ºC, without any cross over of the irradiation curves.

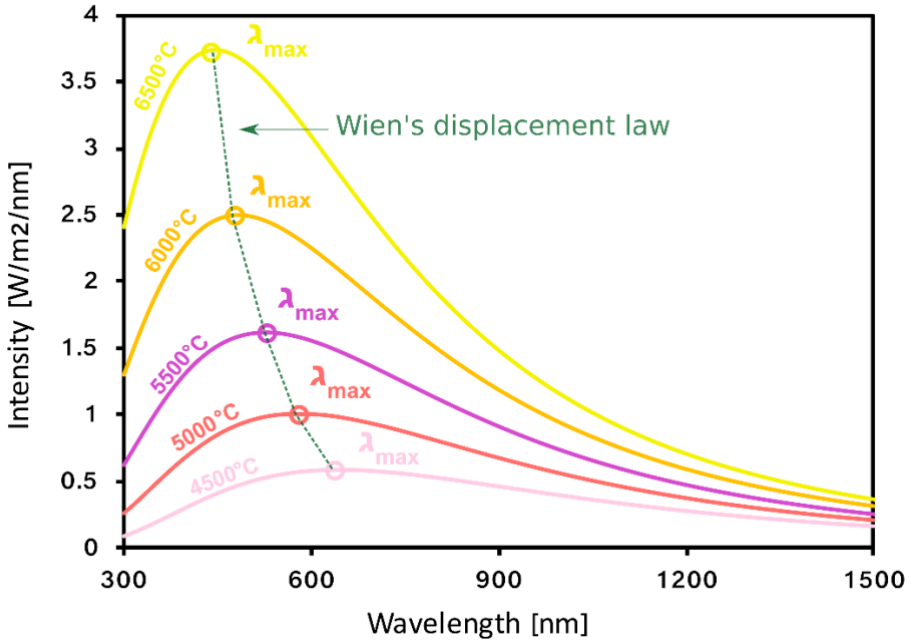

Figure 1.11 – Planck's law describing the amount of the emitted electromagnetic energy by a black body at different temperatures. The green dotted line represents the Wien's displacement law

This implies that more radiation is emitted at higher temperatures and the amount of this energy is proportional to the fourth power of the BB temperature. This is described by the Stefan-Boltzmann law:

$$B_H(T) = \sigma T^4 \tag{1.4}$$

where B is power emitted into a hemisphere, measured in and H denotes a hemisphere.

From Figure 1.11 it can be observed that not only the intensity of the emitted radiation is changing but also its peak is shifting towards shorter wavelengths with the rise in temperature. This is known as Wien's displacement law. Hence, Wien's displacement law predicts that for the objects heated at less than 800ºC the emitted radiation would be mostly located in the IR region.

From Planck's distribution, Figure 1.11, it is also seen that for the Sun, which has the approximate temperature of about 5500ºC, the emitted electromagnetic radiation is mostly distributed in the UV- to near-IR part of the electromagnetic spectrum. After passing through the Earth atmosphere, however, the solar electromagnetic spectrum is attenuated, Figure 1.12, due to ozone absorption of the short wavelengths below 290 nm, and H_2O, CO_2 beyond 2500 nm with partial absorption of the solar spectrum by water vapor. Hence, the solar spectrum at the Earth is primarily located in the range 290 to 2500 nm. Figure 1.12 also shows that the main portion of the solar radiation at the Earth's surface is divided between visible and near IR spectrum, 43% and 52%, respectively with the peak located at around 500 nm, and minor portion of the solar energy in the UV, less than 5%.

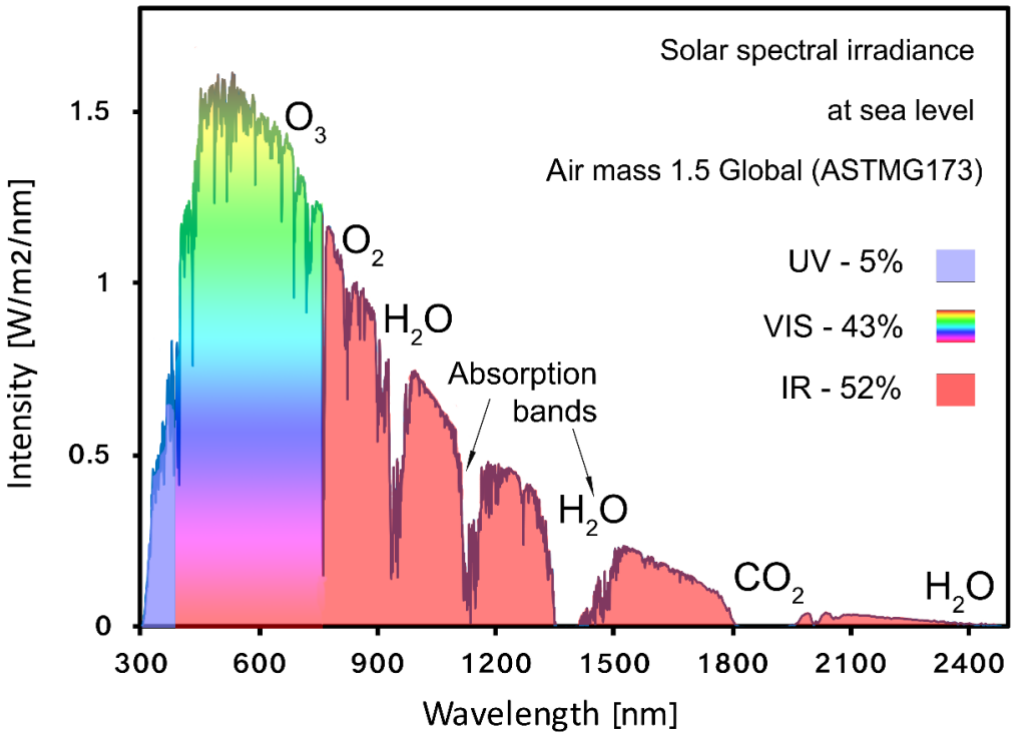

Figure 1.12 – Global solar spectral irradiance at the Earth according to the standard, AM 1.5 (ASTM G173) with the absorption bands due to atmospheric gases identified. Also shown in the percentage of the radiation concentrated in the UV, VIS and IR regions.

Hence, it can be concluded that the region of interest for solar thermal applications is between the middle of the *visible* and the *infrared* because this overlaps both the spectral distribution of the energy radiated by the Sun and the BB emission spectra.

1.2.2 Light/matter interaction

Electromagnetic theory can be used to study the optical behavior of materials. It explains the nature of spectral selectivity, why some materials are transparent to incident light, while others are reflective in some part of the spectrum. For example, human skin absorbs near- ultraviolet light, but it is transparent to X-rays. The UV-light is only distinguished from the X-rays by its lower frequency. Likewise, dielectrics do not absorb visible light and are transparent to it, while metals absorb (and reflect) in the visible solar range and are opaque. In contrast, semiconductors combine both properties.

A multilayer combination of dielectric, semiconducting and metallic films is often applied for STPV and CPTC absorbers. This is so that they can achieve a desired absorptance (A), reflectance (R) or transmittance (T) in the range of wavelengths being considered.

Knowledge of the nature of light propagation through thin films and multilayer systems is necessary in order to describe characteristics such as dispersion, optical constants or optical thickness.

The main optical phenomena that occur during light propagation in a material can be described by the following parameters, Figure 1.13:

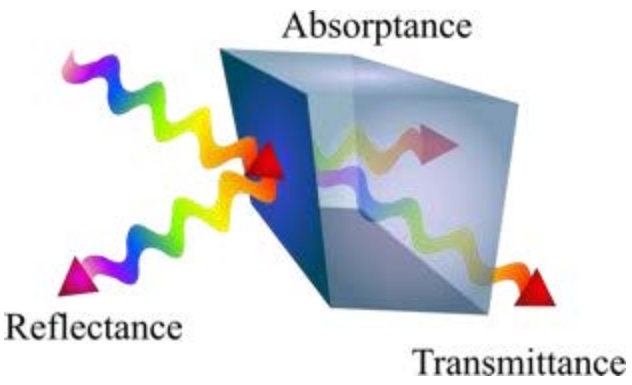

Figure 1.13 – The three main outcomes when light strikes matter.

1) Refraction and attenuation of electromagnetic wave

As it is shown in Figure 1.13, when light interacts with a matter several phenomena can occur. In particular, electromagnetic waves can be refracted and attenuated, Figure 1.14. To characterize the refraction and absorption of optical waves in the matter, coefficient of refraction (n) and extinction (k) are used. These optical processes may be combined via the following formula and are derived from Maxwell's equation:

$$m = n + ik \tag{1.5}$$

where m is a complex refractive index; n is the real part and characterizes the optical density of the medium; k is the imaginary part, which indicates extinction of the wave in the matter [23].

As is shown in Figure 1.14, in vacuum light travels at a constant speed without any refraction, and the refractive index of this medium equals 1. Once the light enters an optically denser medium, it is refracted and travels with a different speed and a shorter wavelength, but with an unchanged frequency, which is schematically shown in Figure 1.14. The refractive index of such media is higher than 1 and the value depends on the intrinsic properties of the material and does not change with a thickness.

Characterization of optical thin films may require using reference data for refractive index and extinction coefficient. However, the various authors obtain slightly different values of optical constants. The reasons for this are differences in deposition methods or in the methods of evaluation of the optical coefficients. Deposition parameters are one of the principle factors in tuning the properties of the material. It is important to note that the refractive index must have required value in the certain spectral range for applications in high temperature CSP. Hence, it is important to ensure that all the factors affecting the value of optical constants are thoroughly controlled and a minimum deviataion from the predictable theoretical value is achieved.

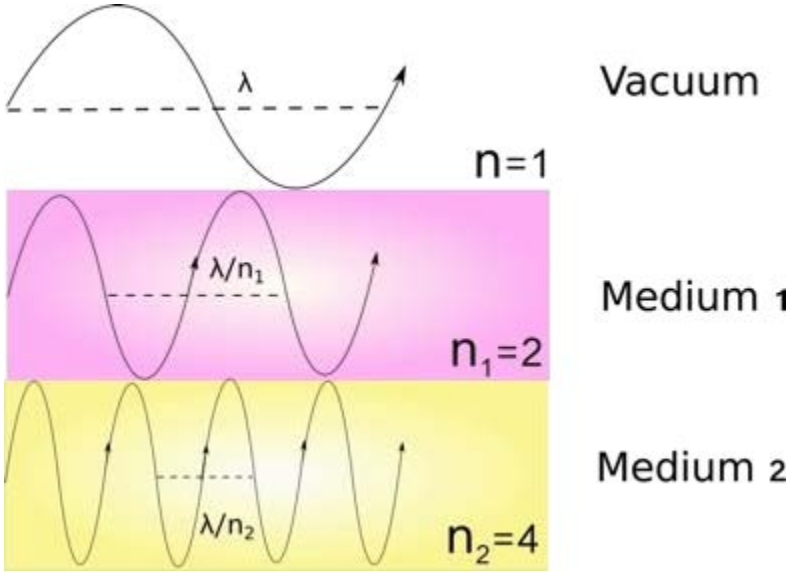

Figure 1.14 – Light propagation through three different medias: vacuum, medium 1 with refractive index n = 2 and medium 2 with n = 4

2) Absorptance, which is characterized by an absorptivity A, absorption coefficient α and extinction coefficient k.

$$A = I_a/I_i \tag{1.6}$$

where I_a is the intensity of absorbed light and I_i is the intensity of incident light. The reduction in the intensity of light can be described by the expression sometimes known as the Beer-Lambert law) [24]:

$$I(x)=I(x_0)exp(-4kt/\lambda_0) \tag{1.7}$$

where $I(x)$ is the intensity of light at the point x below the surface of the material, $I(x_0)$ is the intensity of incident light, t is thickness of a thin film, λ_0 is wavelength of the incident light.

The absorption coefficient α can interpreted as a probability of photon absorption in the material of one unit thickness [25]. Respectively, α^{-1} can be considered as the free length path of the photon in the material and α^{-1} shows the effective length at which the intensity of the incident wave is decreased by e times.

The extinction coefficient and absorption coefficients are connected in the following way:

$$\alpha=4\pi fk/c \tag{1.8}$$

where π is a constant, f is frequency of light and c is speed of light.

From a physical point-of-view absorptance is a transformation of photon energy into other types of energy. It can be expended on 1) modification of energy states of free or bound electrons; or 2) change in the oscillating atomic energy [25].

3) Reflectance, which is characterized by the coefficient of reflectance R and

$$R=I_r/I_i \tag{1.9}$$

where I_r is the intensity of reflected light and I_i is the intensity of incident light. The specifics of light reflectance from an interface are connected with the nature of valence electrons in the materials. The forced oscillation of electrons, which are induced by the field of incident electromagnetic wave, generates reflected waves. For good conductors, which have a high density of free electrons, the intensity of the reflected light may approach the intensity of the incident light. Therefore, metals have found application as reflective surfaces, for instance, mirrors.

4) Transmittance, which is characterized by the coefficient of transmittance T:

$$T=I_t/I_i \tag{1.10}$$

where I_t is intensity of transmitted light and I_i is the intensity of incident light. Transparent bodies weakly absorb in the applicable (*eg*. visible) range of light. Glass, for example, transmits visible light, but highly absorbs in the far infrared and ultraviolet parts of the spectrum.

According to the principle of energy conservation, all of the parameters have to be connected by the following formula:

$$A+R+T = 100\% \tag{1.11}$$

Depending on the functionality of the optical coatings and working wavelength range, they are required to have certain values of absorptance, reflectance and transmittance. Hence, coatings for the CSP applications typically combine a few

materials with different *A*, *R*, and *T* characteristics in order to achieve a desired complex functionality.

1.2.4 Mechanisms of spectral selectivity

As was shown in Figures 1.3 and 1.6, a spectrally selective solar absorbing coating (SSSAC) is a one of the key components in the solar-thermal conversion in CSP applications. A performance of a solar receiver can be described by the following formula, reflecting an efficiency of solar energy into a heat conversion for the normal incidence solar radiation for an evacuated tube collector (Figure 1.5, 1.7, 1.8), where convection losses can be neglected:

$$\eta = \frac{\alpha_s S_{total} - \varepsilon\sigma\left(T^4_{absorber} - T^4_{ambient}\right)}{S_{total}} \tag{1.12}$$

where η is efficiency of heat generation, $\sigma\,(T^4_{absorber} - T^4_{ambient})/S_{total}$ is a weighting factor that defines the contribution of thermal emittance to total performance and σ is Stefan – Boltzmann constant. In this case six parameters are required to define final performance. Two material factors (α_s the integrated solar absorptance and ε the hemispherical emittance), two environmental factors ($T_{ambient}$ the ambient temperature and S_1, the AM1.5 or one sun insolation) and two power and mirror system design parameters (the generator operating temperature determined mainly by $T_{absorber}$, and S_{total} = CS_1, the total incident solar flux with C the solar concentration factor from the mirror –absorber optics).

According to equation (1.12) (which defined the efficiency of photo-thermal conversion) there are two key parameters contributing to the enhancement of heat generation, α_s solar absorptance and ε_s thermal emittance. There are also another two important parameters $T_{absorber}$, the absorber temperature and S_{total} = CS_1 the incident solar flux multiplied by the concentration factor. If one separates the right side of equation (1.13) into two parts by dividing by S_{total} then the weighting factor is obtained which acquires the following format:

$$f_w = \frac{\sigma\left(T^4_{absorber} - T^4_{ambient}\right)}{S_{total}} \tag{1.13}$$

The weighting factor defines the importance of geometrical parameters such as the concentration factor, C, and the power parameter $T_{absorber}$.. For the weighting factor below unity, the contribution into the photo-thermal conversion efficiency is mainly defined by α_s along with the ε_s being important but contributing less to the efficiency of solar conversion to heat energy.

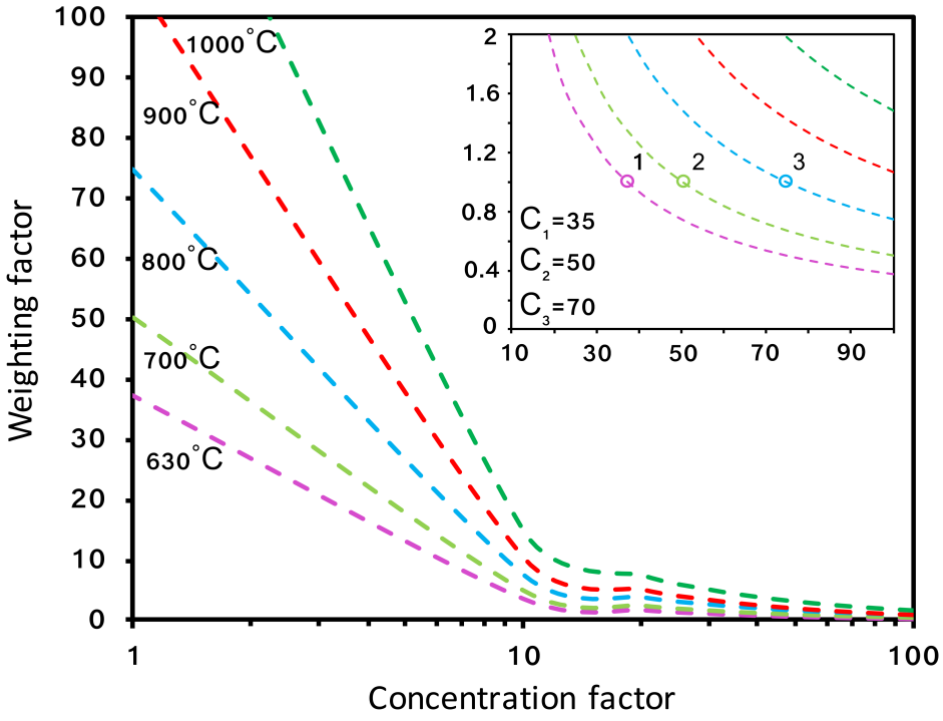

Figure 1.15 – The weighting factor as function of concentration factor at different temperatures.

Figure 1.15 shows this relation. With an increase in the absorber temperature, the weighting factor also rises, showing the growing importance of emittance ε_s. On the other hand, an increase in the concentration factor shows that ε_s plays a secondary role and continues to do so with a further rise in C. The inset in Figure 4.9 shows that, for each temperature, the value of concentration factor at which the rise in solar absorptance by 1% would contribute to much higher solar thermal conversion than reduction in ε_s by 1%. For the selected temperature of 630ºC, at which the maximum efficiency of the parabolic trough power plant would be achieved, the solar flux S_1 should be concentrated at least by a factor of 35. A further increase in the concentration factor causes a reduction in f_w signifying a higher level of α_s contribution to the efficiency η. For higher operating temperatures, this trend is even more pronounced.

The integrated solar absorptance α_s is defined as a weighted sum of the absorbed incident electromagnetic radiation. For the opaque samples, it is typically calculated using the experimental data for the measured spectral reflectance R(λ) at ambient and the known values of ASTM AM 1.5D solar extra-terrestrial spectrum S(λ):

$$\alpha_s = \frac{\int_{0.3\ \mu m}^{2.5\ \mu m}(1-R(\lambda))S(\lambda)\mathrm{d}\lambda}{\int_{0.3\ \mu m}^{2.5\ \mu m}S(\lambda)\mathrm{d}\lambda} \tag{1.14}$$

The thermal emittance ε_s (at normal incidence) at the given temperature can be calculated from IR reflectance spectra using the following formula:

$$\varepsilon_s = \frac{\int_{2.5\ \mu m}^{25\ \mu m}(1-R(\lambda))P_\lambda(T)\mathrm{d}\lambda}{\int_{2.5\ \mu m}^{25\ \mu m}P_\lambda(T)\mathrm{d}\lambda} \tag{1.15}$$

where $P_\lambda(T)$ is the black body radiation as a function of temperature, and is conveniently given by

$$P_\lambda(T) = \frac{C_1}{\lambda^5\left[e^{\frac{C_2}{\lambda T}}-1\right]} \tag{1.16}$$

where C_1 and C_2 are 3.74×10^{-16} W/m^2 and 1.4388×10^{-2} m.K respectively [26].

At this point, it can be concluded that a higher photo-thermal conversion efficiency is achieved if α_s approximates 100% and ε approaches 0%. Fortunately, both conditions can be satisfied due to the differing distribution of solar irradiation and black body radiation in different regions of the spectrum, Figure 1.16. It is seen from Figure 1.16 that solar irradiance spectra and black body radiation spectra at two targeted PTC operation temperatures, 500ºC and 630ºC, are located in solar (300 nm – 2500 nm) and IR region, respectively, with a shift towards shorter wavelengths at higher temperatures due to Wien's displacement for the BB radiation, Figure 1.11. The solar irradiation and BB spectra share a region with minor amount of overlapping energies, but this does not prevent the attainment of nearly idealized behaviour for a spectrally selective solar absorber. In Figure 1.16, a solid squared curve shows the reflectance behaviour of the

idealized SSC depending on the operating point of the PTC. As it should be, the minimum of reflectance is achieved in the solar region, enabling maximum absorption of the solar radiation for enhanced solar to heat conversion efficiency, as shown in formula (1.13). At the same time the possible maximum amount of heat is retained due to minimized emittance in the IR region. Hence, the cut-off wavelength distinguishing maximized solar absorption and maximized IR reflectance is located at 2500 nm for 500ºC operation temperature and at 2000 nm for 630ºC operation.

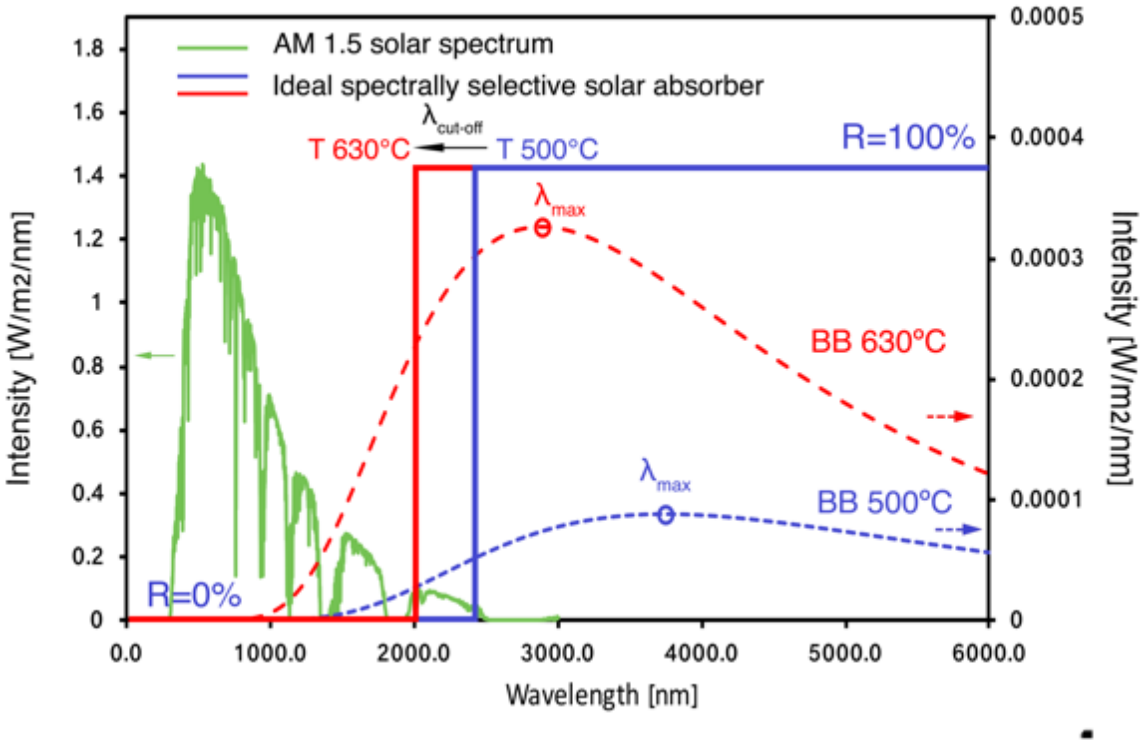

Figure 1.16 – Ideal operation of a solar absorber at 500ºC and 630ºC, with AM 1.5 solar spectrum and black body radiation (BB 500ºC and BB 630ºC) for a more clarified picture of optical behaviour of SSC.

However, naturally occurring materials and thin films made out of them do not have the abrupt spectral transitions of reflectance or absorptance shown in Figure 1.16 and their emittance does not reach zero in the infrared spectrum. Therefore, many scientists have worked to improved existing optical materials and designed new optical coatings to approach the ideal characteristics for solar absorbers. Some of the new designs that have been proposed are shown in Figure 1.17.

Typically, two types of solar absorbing surfaces can be identified, selective and non-selective, Figure 1.17. The main difference between two types is the ability of the non-selective surfaces to achieve higher absorption at a wider angle range (e.g. flatter spectral response to higher angles of incidence) and at a lower cost of production, however, selective surfaces are at least 10%-20% more efficient due to their ability suppress re-radiation, indicating that the lower concentration ratio of suns is required to raise the collector's temperature [14]. The focus in the present thesis will be on the selective type of solar absorbing surfaces.

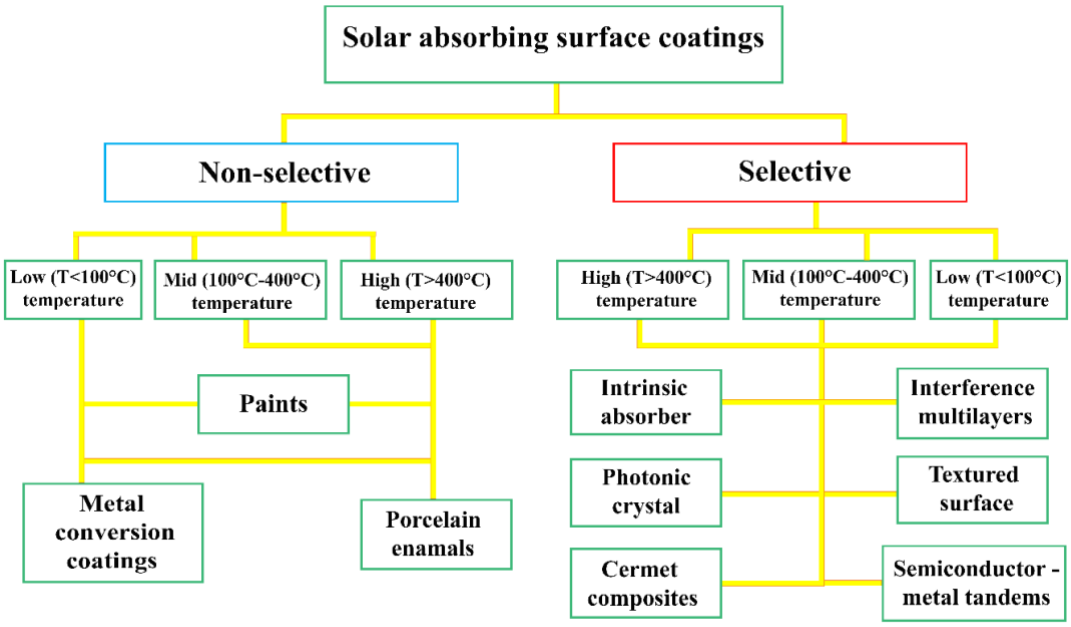

Figure 1.17 – Types of solar absorbing surface coatings developed for solar thermal applications

To date, there are six main designs of the spectrally selective solar absorbers: intrinsic absorbers, metal-dielectric tandems, semiconductor-metal tandems, structured surfaces, cermets and photonic crystals, Figure 1.18.

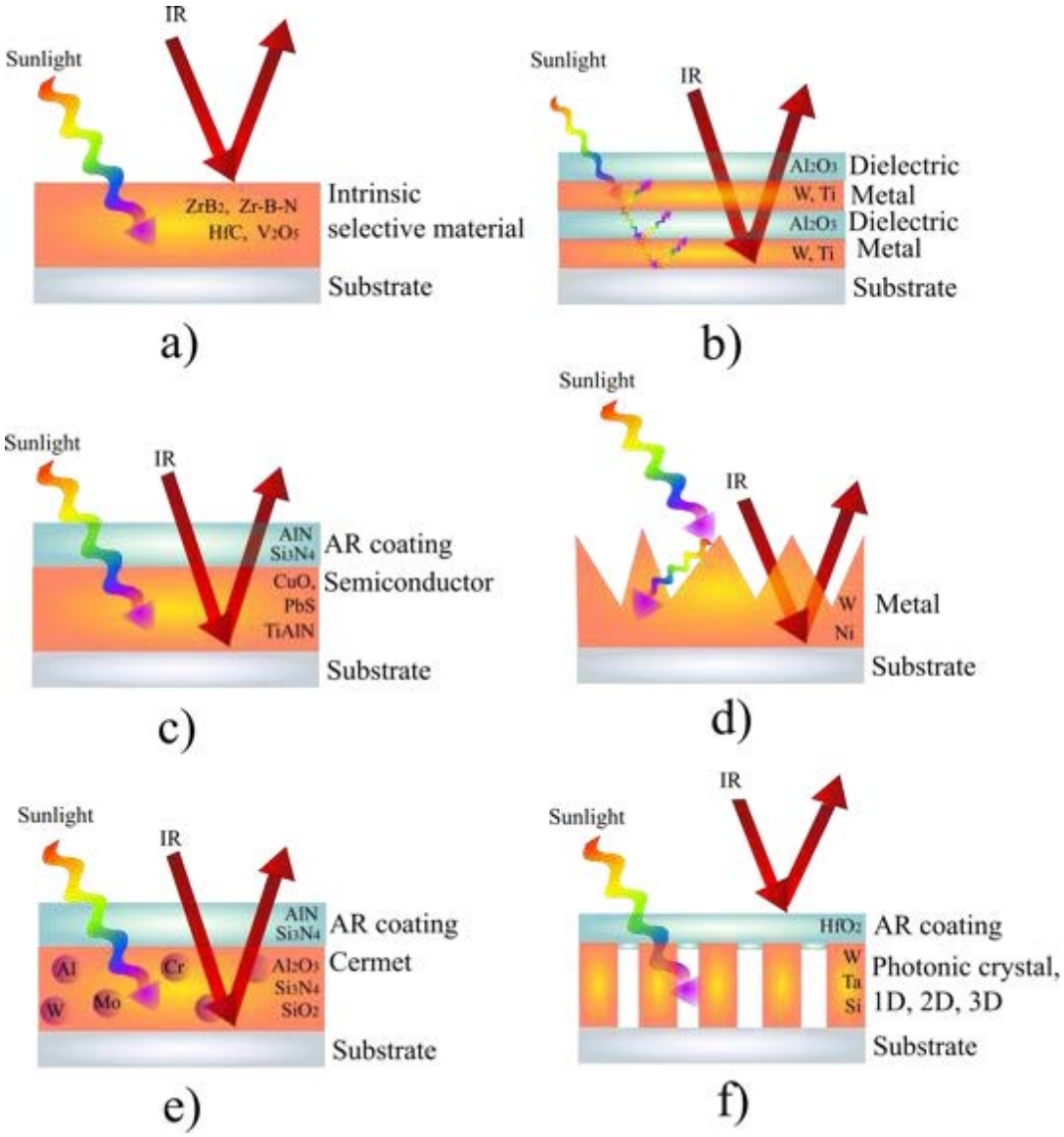

Figure 1.18 – Design types of spectrally selective solar absorbing coatings for CSP applications with some example elements used in a fabrication process: a) Intrinsic absorber, b) metal-dielectric tandem, c) semiconductor-metal tandem, d) structured surface, e) cermet composite with metal nanoparticles dispersed in the dielectric matrix, f) photonic crystal

Intrinsic solar absorbers, Figure 1.18a, are easy to fabricate and have intrinsic spectral selectivity, which is attributed to the presence of both metallic and covalent bonds [27]. They also exhibit structural integrity and excellent physical properties as ceramics, such as high melting point, and which makes them suitable candidates for high temperature CSP applications. Although, there are no naturally occurring ideal spectrally selective solar absorbers, many semiconductors and transition metal nitrides, oxynitrides,

oxides, carbides and borides can exhibit moderate spectral selectivity if they are modified by co-doping or an additional antireflective (AR) layer is utilized. The examples include ZrB_2, TaB_2, TaC, Zr-B-N, HfC, HfB_2, SiC, ZrC, V_2O_5, TiN, ReO_3, and Eu_2O_3 [28-35]. Tungsten (W) also shows an intrinsic spectral selectivity, being one of the exceptions among the pure metals where abrupt rise in the reflectance in the near-visible would normally start. The main disadvantages of such structures is non-ideal spectral selectivity. This is evident as a gradual transition in the cut-off region around 2500 nm unlike the sharp change shown in Figure 1.16. In addition, the transition from absorption to reflection occurs at too short wavelengths, and absorption in the solar range does not reach the highest value possible. Hence, intrinsic solar absorbing thin films are often integrated into other more complex structures like multilayers or cermets, in order to further improve their performance. These issues will be discussed further later.

Metal – dielectric tandems employ alternating ultrathin films of semitransparent metal and a dielectric material to create an interference effect on the IR-reflective substrate, Figure 1.18b. There are two main factors that contribute to the solar absorption and spectral selectivity of the light.

The first contribution is the capture of the light between the two layers of the stack based on the destructive interference phenomenon. The passing of the light through the semitransparent and dielectric layers with a defined phase light is reflected at the interface of the two layers, where the complex phase shift occurs and the value of which depends on the optical constants of the thin film. Hence, the light interferes destructively with the light beam reflected from the top of the surface with the light multiple times reflected from the back of the lower layers of the stack, Figure 1.18b. This phenomenon can be maximized if the thicknesses of the stacked thin films and their corresponding optical constants are selected carefully.

The second factor is attributed to the nature of ultrathin dielectric and metallic layers, the thickness of which varies in the range of several dozens angstrom to no more than 20 nm for the metal and up to 150 nm for the dielectric. Due to a wide band gap of the dielectric thin film, an absorption of the solar radiation is pushed towards longer wavelengths. The main absorption occurs inside of the metallic film.

Some examples of such systems are AlN/Ti/AlN/Ti/Cu [36], SiO_2/Ti/SiO_2/Al [37], SiO_2/Cr/SiO_2/Al [38], and Al_2O_3/Mo/ Al_2O_3/Mo [39]. The stack may also employ any other metals or dielectrics that are stable at high temperature.

Semiconductor – metal tandems, also known as absorber-reflector tandems, Figure 1.18c, are based on the semiconductors with a certain value of a band gap (0.5 eV – 1.5 eV) designed to absorb visible and near-IR light on top of the IR reflector aimed to suppress the IR emittance from the heated substrate. In this way, the photons with energy high enough to overcome the bandgap of the semiconductor are absorbed and photons with low energy pass through the semiconductor resulting in the IR transparency of the layer.

The better-known examples of this type of coating are Si, Ge, PbS, CuO, while more recently nitride-based semiconductors became widely investigated due to an ability to modify the band gap and tune an absorption spectra by addition of additional elements (e.g. TiAlN) [40].. Due to a high refractive index of the semiconducting material, there are undesired reflectance losses, which can be avoided by applying an AR layer on top of the semiconducting layer to enhance light transmission and reduce reflectance losses. The refractive index of the AR layer typically lays between 1.5 and 2.1, depending on the type of the dielectric used, deposition method and, possibly as in the case of AlN, metal to non-metal ratio.

Such a design can result in a high spectral selectivity and solar absorption. However, the drawbacks include oxidation of the semiconductor and possible diffusion due to instability at elevated temperatures. Both of these issues can be overcome by applying a dielectric layer on top of the stack and introducing a diffusion barrier layer between the semiconductor and the IR reflector [41].. Another challenge is emission losses at elevated temperatures due to electron – hole pair generation and free carrier radiative emission [10].

Structured surface, Figure 1.18d, illustrates the principle of surface texturing of the metal with the feature size comparable with the wavelengths in the visible and near-IR range. Such a design enables optical trapping of the light in the solar range where the solar photons are multiply reflected and lost between the metal "needles" giving an amplified solar absorptance [42]. In contrast, the longer wavelengths of the IR spectrum are reflected due a shorter distance between the needles compared to the size of the IR wavelength, thus, preserving low emission. This type of design enables a reasonable control over the degree of selectivity due to the ability to modify the height, separation and angle of the metallic "needles" during fabrication. High solar absorptance (95% - 99%) and an ability to provide scalability and cost - effectiveness for commercial production is feasible.

The typical materials for textured surfaces are refractory metals such as Ni, W, Mo, [43-45], however, the concept is not restricted to metals only and new materials such as SiGe and CuO have been recently suggested [46, 47].

The main disadvantage of this type of structure is instability at higher temperatures and quick optical degradation above 300ºC and 450ºC [45, 48].

Cermet composites, Figure 1.18e, employs the use of a ceramic and a metallic material, where the metal particles of a nanometer size are distributed in the ceramic matrix deposited on top of a highly reflective metal. The reflective underlayer reduces IR radiative losses at higher temperatures. There is often an AR coating on top of the coating for reduced reflection in the solar range and oxidation stability. The cermet itself is transparent for the mid- and far-IR wavelengths, while absorbing strongly in the solar. The solar absorptance is secured by the combination of two mechanisms both occurring in the metal particles. The first is absorption due to interband electronic transitions that absorbing the photons of the certain energy range and the second is the phenomenon known as plasmon resonance. Further optical tunability can be provided by grading the coating to get a transition from a high index of refraction starting from the substrate to a low one at the surface. The latter should approach the value of the refractive index for the AR coating. The metal nanoparticles are present at high volume fraction to start with but are usually randomly dispersed inside the dielectric layer and deposited on top of the IR reflector, followed by a second cermet layer with a lower volume of metallic inclusions. Such a transition can provide a more effective light capturing effect due to the varied refractive index.

Cermet composites have gained high popularity among researchers due to their ability to offer a wide range of optical behaviour by changing the type of the metal nanoparticles and the dielectric host, the density and the size of the metallic inclusions and the layer thickness. The typical dielectric hosts are AlN, SiO_2, Al_2O_3, Cr_2O_3 and the metals are Al, Cr, Mo, W, Ag, Ni, SS, Cu [7]. The selection of both metal and the ceramic matrix are crucial in order to obtain thermal stability and prevent any diffusion or oxidation.

Due to their high temperature stability in combination with relatively inexpensive manufacturing routes, a number of these cermets have been a commercial success. The examples include Cr: Cr_2O_3, Mo: Cr_2O_3, Ni:NiO_x, Co: Al_2O_3,Mo: Al_2O_3,and W: Al_2O_3 [49].

The drawbacks of the cermet design are possible diffusion of the metal particles and/or atomic species, agglomeration, and oxidation through possible porosity or the oxide host matrix.

Photonic crystals, Figure 1.18f, are a relatively new approach to achieve high solar absorptance and spectral selectivity. They employ periodic nano-scale patterns (e.g. nanocons, nanopyramids, nanowires) with the size comparable with a particular wavelength distributed in the direction of a light propagation [50]. Due to a replication of the photonic crystal (PhC) nano-features along which the light is propagated, there is a generation of allowed and forbidden photonic states, which is a useful tool in order to achieve enhanced absorption of photons in the solar range and create forbidden states for the IR region to approach near-ideal spectral selectivity [51]. On the other hand, the presence of allowed and forbidden bands gives a rise to a non-ideal solar absorption and appearance of the "reflection humps" in the solar region due to a diffraction phenomenon. This depends on the periodicity of the photonic crystal. It has been shown in [52] that this might be the case for the photonic crystal structures having periodicity of the cavities bigger than the incident wavelength causing a gap in the absorption band in the solar spectrum. To overcome this problem different types of antireflective coatings can be deposited on top of the PhC.

The majority of the current researches is devoted to development of the photonic crystals for the STPV applications, where the temperatures of more than 700ºC are involved, hence, the materials of interest are represented by refractory metals, since they naturally can provide IR reflectance as well.

There are three types of PhC, 1D, 2D and 3D. 2D structures are thermally advantageous due to reduced number of interfaces compared to 1D multilayer structures and 3D. The currently developed photonic crystals use Ta, W, Ni and Si to create nano-scale structures [53]. Although, refractory metals can withstand elevated temperatures well enough, some structural degradation is still observed due to a presence of high number of interfaces contributing to faster surface diffusion and thermal stresses [54]. Some attempts were made to avoid these issues by applying a high temperature stable AR coating such as HfO_2, which also has an additional function, that of boosting solar absorptance [52].

The drawback of the photonic crystal absorbers is expensive fabrication due to the complicated techniques involved, such as ion etching or atomic layer deposition along with the difficulty in realization of mass production for commercial purposes.

1.3 Survey of currently available coatings

The production of solar absorbing and spectrally selective coatings with acceptable thermal stability is an important problem in its own right. The important applications of such coatings in new technologies such as thermophotovoltaics and concentrated solar power ensure that there is widespread interest in solving this problem. The main challenge is to combine the required optical response and thermal stability. Even if a desired spectral selectivity and low emittance is achieved, the material may not be stable at high temperatures and vice versa. Nevertheless, a number of spectrally selective coatings utilizing the designs discussed above have been commercialized. Some even employ "hybrid" designs, where several approaches were used in one structure to achieve boosted spectral selectivity.

The following short literature review sheds a light on the currently available solar absorbing coatings and the difficulties they face when exposed to severe temperatures.

The majority of the production techniques involve physical vapour deposition (PVD) (eg. evaporation, sputtering, pulsed laser deposition, ion plating), chemical vapour deposition CVD processes, wet-chemical techniques (e.g. solution based method), electrochemical depositions, such as electroplating/anodization and spray processes (e.g. flame spray pyrolysis). Sputtering has gained the biggest popularity due to possibility to its ability to produce dense and reasonably uniform thin films on a wide area scale, and widespread commercialization of the sputtering technique. Nevertheless, a disadvantage is a comparatively high cost of the technique replacement with machinery compared to solution-based methods.

Figure 1.19 shows some of the solar absorbers developed to date. These are based on the different designs shown before, such as multilayers, cermets, interference stacks etc. The plot was constructed based on the key metallic element contributing to the absorptance process.

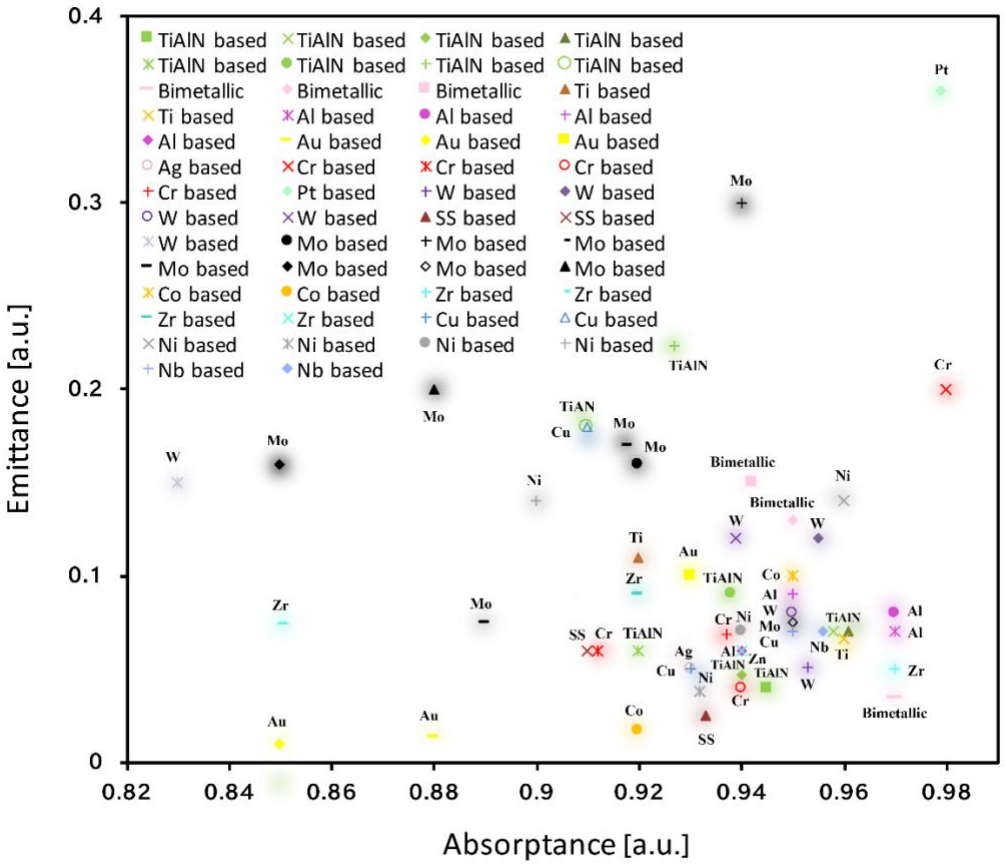

Figure 1.19 – Comparison of the currently developed spectrally selective solar absorbers based on data from [7-11]

It is seen from Figure 1.19 that the solar coating with the desired optical response are to be located in the right bottom corner of the plot, thus, identifying maximized absorptance of the solar radiation and an ability to suppress thermal radiation, with emittance value approaching zero. It is clear that to date no ideal SSC has been developed, however, there are few solar absorbers that approach the desired functionality.

The best candidates in terms of optical response before annealing are represented by the Al-based absorbers, the Zr-based and the absorbers employing bimetallic nanoparticle inclusions in the cermet, followed by the Ti-based selective coatings.

In case of the *Al-based SSC*, a nearly ideal spectral selectivity ($\alpha = 97\%, \varepsilon = 0.07$) was achieved by using a graded cermet layer with the high and low volume of the Al nanoparticles in the AlN matrix. The further reduction in reflectance was achieved by

applying the AR AlN layer and self-assembled nanostructured AlN layer, which enabled an increase in solar absorptance by almost 3% due to a presence of small nanopores trapping the light [55]. For the *Zr-based SSC* α was 96% and ε was 0.05. The researches also used the cermet approach with the Zr nanoparticles distributed in the ZrO_2 host matrix [56]. Three parameters were varied in order to achieve an enhanced solar absorptance and thermal emittance. The authors increased the number of cermet layers, varying the volume fraction of the Zr particles. Replacement of the ZrO_2 AR layer with an Al_2O_3 layer and the Zr IR reflective layer with anAl reflector caused the solar to thermal conversion efficiency to rise to nearly 90%, compared to an efficiency of 85% for the un-optimized SSC studied in this work. The authors also claimed that the coating possessed good thermal stability in air at 300ºC – 350ºC, but the results were not reflected in the paper.

The Cr-based and the Pt-based absorbers show the highest value of the solar absorptance, 98%. The Pt-based SSC used a graded cermet design, Pt:Al_2O_3 with Pt IR reflector, and textured SiO_2 as the AR coating. The boosted solar absorptance was achieved by using a very thick solar absorbing cermet layer with a textured SiO_2 layer on top, with a very low index of refraction, enhancing solar absorptance by 4%. However, such a design results in the increased value of emittance (0.37 at 200ºC) due to absorption of the SiO_2 layer in the IR [57]. The Cr-based design included an Al reflective layer and a graded Cr:Al_2O_3 cermet prepared by electroplating [58]. A remarkable 98% solar absorptance was achieved and the coating remained stable up to 250ºC with the degradation starting at 350ºC. In this example, the biggest challenge in the manufacture of spectrally selective solar absorbers for high temperature CSP applications is seen: a remarkable solar absorptance is secured at the room temperature, but undergoes a big change at the mid-temperatures, not considering the elevated value of the thermal emittance before annealing, 0.2, compared to other designed absorbers.

The refractory metals-based solar absorbers take rather a transitional position with the value of solar absorptance being lower than 96% but still high enough to achieve reasonable solar-to-thermal efficiency. Some of the best candidates are the Mo:MoO_2 (black molybdenum), Mo:SiO_2, W:WO_2 (black tungsten), W:AlN [43, 59-61].

Developed by Zhang, the W:AlN solar absorber employs a sophisticated cermet design (Figure 1.18e) with the addition of a secondary cermet layer with a different volume fraction of W metal particles in the dielectric AlN host matrix [61]. Al was used as the IR reflector and AlN was used as an AR coating. The author managed to achieve

an excellent thermal stability at 350ºC with the initial solar absorptance and thermal emittance being almost unchanged after the heat treatment, α =93.9%, ε =0.039 and α =93.8%, ε =0.037, respectively, where "excellent"/"good" implies having an optical and/or structural stability at a particular temperature with the absence of changes or minor changes not affecting crucially the optical perfomance. This is a good result, however, for high temperature CSP applications the heat test should be conducted at much higher temperatures and the optical behaviour should be monitored carefully, since outwards diffusion of the Al from the IR reflector is expected. This suggests that the stack should be further modified.

Contrary to the W:AlN SSC, the W:WO_2 SSC developed by Thomas and Chain [61] shows weaker solar absorptance, by nearly 11% along with the emittance being higher by 0.011. The authors also report significant structural changes during annealing above 600ºC. At this point, the ratio of the present elements has changed due to an oxygen reduction and appearance of the different tungsten oxides in the cermet layer. This implies also changes in the optical behaviour, which is not suitable for CSP applications in the >500ºC temperature range.

The Mo:SiO_2 SSC was designed by Wang using the cermet approach [60], where the IR reflector was introduced by the Mo, the main absorbing layer was introduced by the dispersed Mo particles in the SiO_2 , the AR layer was represented by the SiO_2 film. Such a design resulted in α =95% and ε =0.097 with no change in α after cyclic thermal annealing at 800ºC in vacuum for 2 hours for ten times. Simultaneous decrease in thermal emittance by 0.022 was also noticed facilitating even better optical performance after heat treatment. This was attributed to the crystallization of the metallic fraction in the coating leading to enhanced conductance and, as a result, better IR reflectance. The Mo:SiO_2 SSC is a good candidate for ta CSP, however, further heat treatment experiments are needed to confirm long term thermal stability.

Au-based absorbers are interesting candidates for the solar thermal applications due to the oxidation resistance of Au and the ability of Au nanoparticles to sustain localized surface plasmon resonances. However, according to the literature review plot, Figure 1.19, the published Au-based absorbers show one of the weakest solar absorptances, only reaching a value of around 85% to 88%. This implies that any SSC using Au nanoparticles should be further investigated and redesigned to fully exploit promising plasmonic and anti-oxidation properties of the Au.

It is also interesting to consider TiAlN-based SSCs. From Figure 1.19 it can be seen that the currently developed TiAlN SSC are located between 90% and 96% solar absorptance but the emittance varies between 0.25 and 0.05. The best TiAlN candidate in terms of optical response was introduced by Jyothi *et al.* in 2015 [62]. Their design for an absorber consisted of an IR reflector and five individual layers, with each layer containing the Ti and the Al with varied percentage and different non-metals such as C, N, Si, O in order to create a graded index of refraction throughout the coating. The resulting coating showed a good long term stability in vacuum up to 600ºC with no change in solar absorptance of 93.1% but suffered degradation during a short-term anneal at 900ºC. The stack was also unaffected by air annealing at 300ºC with the unchanged solar absorptance of 95.9%. The TiAlN based and oxynitride based SSCs should be further investigated. In particular, the new designs and/or different additives to push the thermal tolerance limit and boost spectral selective properties should be explored.

It is worthwhile highlighting one of the key problems of a SSC when it is exposed to high temperatures: this is the difficulty to secure optical stability simultaneously with structural stability. The studies mentioned above reveal that currently developed SSCs experience structural changes when the temperature is raised and that this generally leads to some modifications in optical response. Table 1.1 represents some key problems that a SSC may face during annealing.

As seen from Table 1, the most common problems include the migration of the metallic particles in the cermet layer or the out-diffusion of the metal in the back reflector. These problems can be solved by finding matrix/metal combinations with a lower coefficient of diffusivity for the metal. As will be shown in Chapter 3, this could include limiting the diffusivity of the metal phase by alloying it with another metal.

Table 1.1 – Common degradation problems a SSC undergoes during thermal annealing, where thermal stability implies the absence of any optical changes or negligible changes may occur and a threshold temperature implies irreversible changes occur. The further details of studies can be found in

Solar absorber	α as-deposited	α annealed	ε at the given temperature	Thermal stability	Threshold temperature	Cause of degradation
Mo:SiO_2 [60]	94.7%	92.1%	0.015 (400°*C*)	600°*C* *(vacuum)*	800°*C* *(vacuum)*	Grain growth, diffusion of the Mo particles and/or atomic species

Mo:Al_2O_3 [63]	91%	-	0.027 (800°*C*)	500°*C* *(vacuum)*	800°*C* *(vacuum)*	Diffusion of the Mo particles and/or atomic species
W:Al_2O_3 [64]	93.9%	93.7%	0.13 (580°*C*)	580°*C* *(vacuum)*	-	Oxidation of the W particles
Au:Al_2O_3 [65]	93.8%	93.3%	0.04 (300°*C*)	300°*C*	400°*C*	Particle agglomeration
Cr:Cr_2O_3 [58]	98%	84%	0.2 (27°*C*)	250°*C* *(air)*	350°*C* *(air)*	Shape and phase transformation of the NPs
Au:MgO [66]	93%	93%	0.1 (400°C)	300°C (air)	500°C (air)	Crack formation, surface aggregation
Al:AlN [55]	97%	96%	0.07 (80°C)	-	250°C (air)	diffusion of the Al back reflector into the coating, surface oxidation

Oxidation of the metallic particles in the cermet is also a possible problem. Typically this can be attributed to factors such as 1) chamber impurities with the presence of residual oxygen on the walls and contamination of the coating during deposition; 2) insufficiently dense structure of the SSC and presence of the nanopores or short pathways for potential oxidation; 3) presence of oxygen in the host matrix itself such as Al_2O_3; Cr_2O_3; SiO_2; MgO; 4) high reactivity of the metal itself with oxygen, like Al, which can aggravate the oxidation process if any of the aforementioned factors are contributing. The oxidation issue in the as-manufactured coating can be solved by ensuring a high level of vacuum in the chamber in order to reduce the amount of the residual oxygen. Oxidation during service can be alleviated by replacing the host matrix; achieving a more densified structure of the film which can be achieved by choosing proper parameters during deposition process (such as flow rate, current); selecting an oxidation resistant metal, or as it will be shown in chapter 3, alloying the metallic nanoparticles.

The formation of thermal cracks is yet another issue to be considered. These are attributed to the difference in the thermal expansion coefficients of the different materials present in the coating. This issue can be minimized if materials with low or similar coefficients of thermal expansion are selected.

The diffusion of the metal back reflector into the coating is also one of the common issues which can be prevented if a diffusion barrier is placed between the reflector and coating above it. Alternatively, the materials for the upper layers must be chosen to have low reactivity with the reflector material.

Concluding the short survey, it can be seen that a large proportion of the spectrally selective solar absorbers currently manufactured or reported use three main constituent design elements, represented by:

1. Anti-reflecting layer to extinguish reflected light and ensure further light transmission to the absorber

2. Absorbing layer to collect solar energy and usually represented by dispersed metallic particles in a dielectric host matrix.

3. Strongly reflective bottom layer to enhance reflectivity in the certain wavelength region and deflect the light that was not absorbed by the absorbing layer.

By applying these concept, energy conversion efficiencies using formula (1.12) of around 90% were achieved in the majority of the SSCs developed to date. To further increase the efficiency of solar collectors or other concentrated solar thermal units, each layer can be enhanced separately or more layers can be added to the stack. However, as I will show later, extra layers do not always lead to significant efficiency improvement.

Chapter 2
Methodology

2.1 Thin film deposition

There are diverse methodologies for manufacturing high quality optical thin films for high temperature spectral selectivity. Mainly these involve chemical and physical vapor deposition (PVD). Among these, PVD techniques of vacuum evaporation and vacuum/cathode sputtering are the most widely used techniques for solar coating production.

In general, it could be said that the process of the thin film deposition in a vacuum includes three main steps:

1) Generation of flux of particles towards a substrate

2) Condensation of the particles on the substrate

3) Formation of the thin film

There are some differences between various techniques however. The simplest configuration of the sputtering system is represented by the two electrodes: cathode (a target) and anode (substrate) enclosed in the vacuum chamber and connected to a power supply. There are two types of sputtering: DC (direct current) and RF (radio frequency). Vacuum sputtering does not require heating of the sputtering material to deliver energy and eject atoms from a target, instead of this, plasma ions bombard the target to produce atoms for the deposition.

In DC sputtering, directed ion flux is provided by the applied electric field between cathode (target) and anode (substrate). Plasma is maintained by the electric field and introduction of chemically pure gases such as argon. These factors ensure creation of discharge in a vacuum chamber, which is characterized by the creation of a high density of ions and electrons [1]. Atoms of the desired material are dislodged from the cathode and then deposited onto a substrate in the form of thin film. Figure 2.1a shows a setup of cathode deposition equipment using magnetrons (discussed further below).

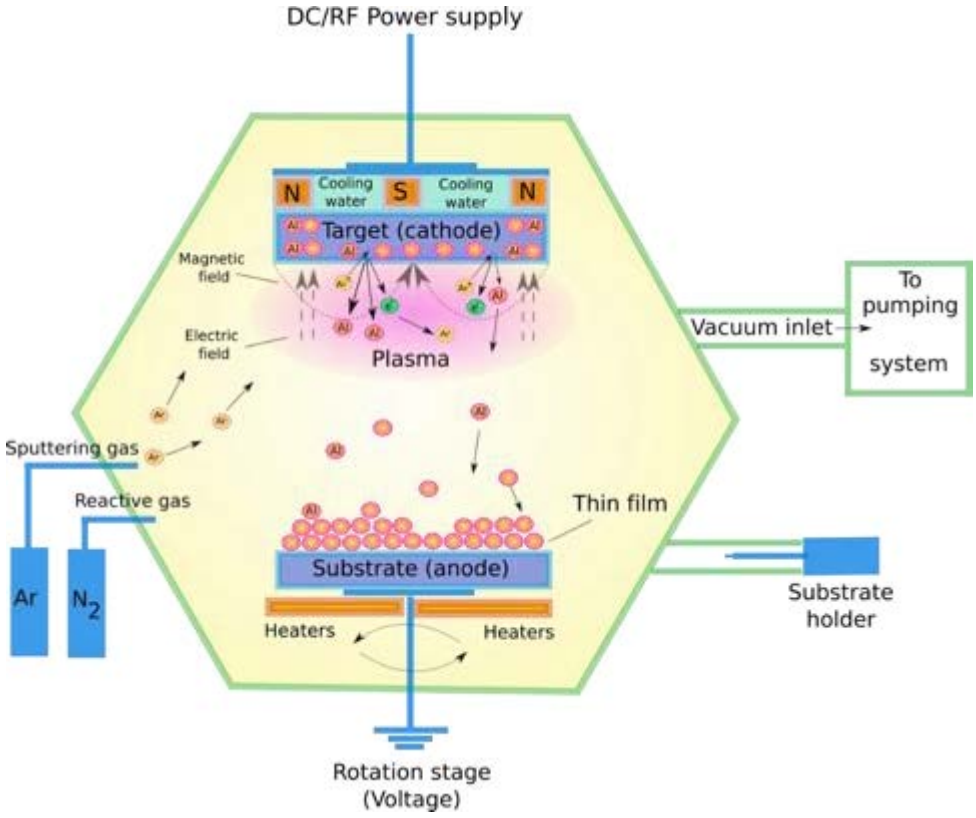

a)

b)

Figure 2.1 – a) A schematic of magnetron sputtering system using Al target as an example; b) a dual target magnetron sputter used to deposit the coatings for CSP

For deposition of insulating materials, RF sputtering is used, where the idea is to prevent accumulation of the positively charged particles on the cathode by application of an alternating current.

It is worth mentioning that deposition rate depends on energy, angle of incidence and nature of bombardment ions, type of sputtering material and geometrical factors. All these factors influence the structural and, hence, the optical properties of the deposited coating.

DC sputtering capabilities can be broadened: by introducing additional reactive gases (e.g. oxygen, nitrogen). In this manner, dielectric or semiconducting coatings like AlN or TiAlN can be obtained.

In the case of magnetron sputtering, a magnetic field is applied to achieve efficient sputtering at lower pressure. The main difference between trivial vacuum sputtering systems and systems with magnetic field (that is magnetron sputtering systems) lies in denser plasma, which generates denser ion flux and higher sputtering speed. Other advantages are that use of a magnetron system enables a decrease in substrate temperature by 100-200K and the possibility to use targets composed of metallic alloys or insulating materials by using DC or RF regimes, respectively [67]. It also allows one to obtain homogenous coatings over a big area. Hence, magnetron sputtering enables improved characteristics and broader capabilities. This technique is widely applied for production of high quality thin films.

Regardless of the type of manufacturing used, there are some general factors that affect the performance of optical thin films. One of the key requirements is high homogeneity of the film. The thickness of optical thin films is typically in the nanometer range (from several hundreds of nanometers to few tens of nanometers). Thus, the requirement for homogeneity is stringent compared to other types of films. Optically inhomogeneous films have lower performance efficiency and, hence, have limited applications.

In general, there are two sources of inhomogeneity. Firstly, the homogeneity of deposited thin films depends not only on the purity of the initial material, but also on the impurities that can be introduced during deposition. There are several sources of such impurities. For example, the impurity particles may come to the film after being sputtered off the target holder or chamber wall. The main issue here is that the melting temperature of the particles that came from target holder or chamber may be considerably lower than that of the intended film and/or they may destabilize the phase composition of the film.

Secondly, the residual gasses in a vacuum chamber may be a source of inhomogeneous thin films. During deposition the condensing material may bind atoms of oxygen or other residual gasses resulting in porous or rough films. As an example of the second effect, the addition of oxygen to a TiN alloy weakens the influence of nitrogen as a stabilizer of the α-phase [68]. To avoid such contamination high vacuum has to be provided. High vacuum ensures the linearity of atom trajectory from the sputter target to the substrate and the purity of the condensed layer. In general, inhomogeneity of the film decreases if high sputtering speed and low pressure of residual glasses is provided [24].

2.2 Scanning electron microscopy (SEM), energy dispersive X-ray spectroscopy (EDS) and high resolution transmission electron microscopy (HR-TEM)

The *scanning electron microscope (SEM)*, Figure 2.3, enables determination of a structural, morphological and elemental composition by using highly focused electron beam (1 nm to 10 nm in width and with energy of 0.1 – 30 keV) generated by an electron gun and further focused by lenses and apertures onto a solid sample in a high vacuum (~ 10^{-6} - 10^{-7} Torr) in order to prevent any beam interaction with residual gas molecules [69]. The exploitation of electrons instead of conventional light is necessary to achieve high resolution due to the shorter wavelength of the electrons. The electron beam interaction with the material is associated with several useful phenomena, leading to the appearance of different types of emission, Figure 2.2. Consequentially, emission of secondary electrons, backscattered and Auger electrons, X-rays occurs giving an opportunity to detect these signals and obtain an image containing morphological and structural information. Most often, however, the secondary and backscattered electrons are used.

The preparation of SEM samples does not involve as sophisticated a procedure compared to the TEM (which will be discussed further) as the electrons do not have to penetrate through the sample. However, if the sample is insulating then imaging it is difficult due to electrostatic charging from the electron beam. In this case, a conductive tape is often placed onto the investigating sample or the sample is coated with a thin film of metal (usually gold) or carbon. Another solution is using a low voltage electron beam. In general, lower voltages using secondary and backscattered electron regimes enable the

imaging of fine scale morphological features of the sample due to lower penetration depth into the material.

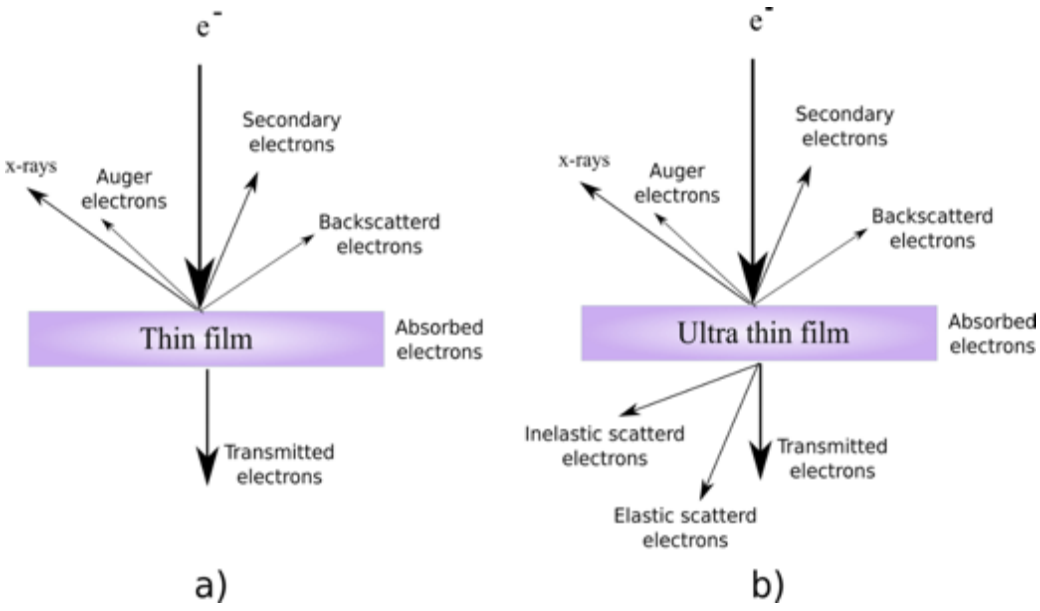

Figure 2.2 – Electron beam interaction with a sample for a) scanning electron microscopy and b) transmission electron microscopy

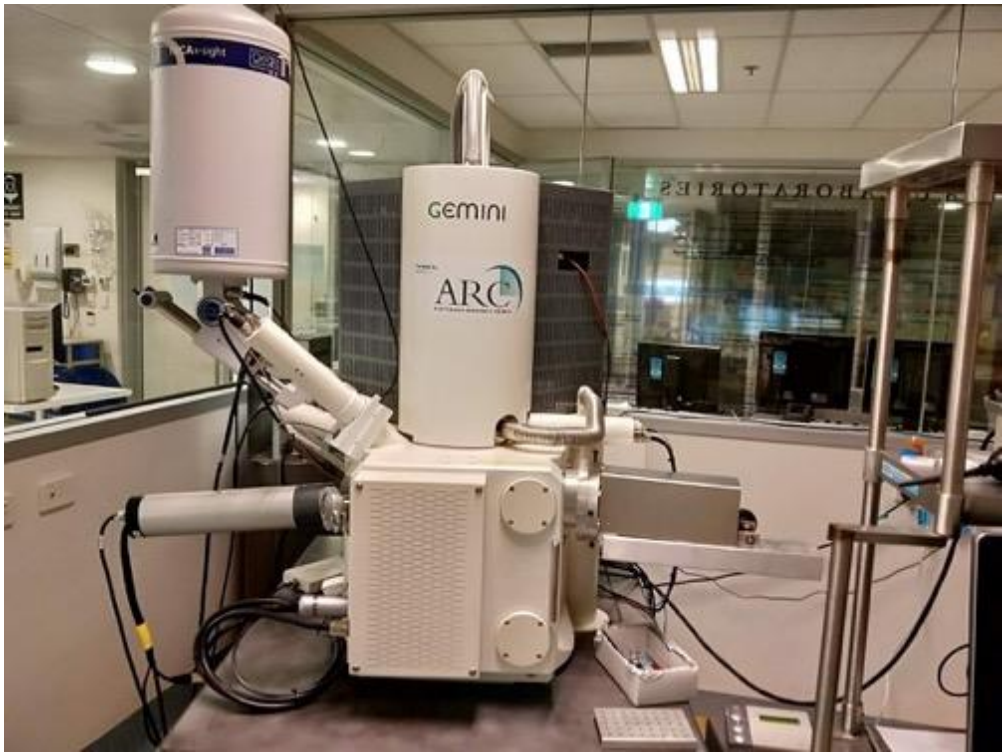

Figure 2.3 – The SEM used to investigate the structural features and morphology of the deposited samples

In the current work, different types of thin films were used including dielectrics, semiconductors and metals. In some cases these were combined in one sample, raising the difficulty. This problem was solved by firmly sticking the sample to the substrate in order to ensure the absence of any movement, applying a conductive copper tape onto the sample, and using a moderate accelerating voltage (within 5 keV – 15 keV range). The right adjustment of the objective-lens current, astigmatism correction created by the lenses and contrast was also necessary to capture a sharp and clear features of the investigated thin films and coatings.

Energy dispersive X-ray spectroscopy (EDS) is widely used to detect an elemental composition of a material. In this case, the X-ray waves that are generated by electron transitions between the shells of different energy levels are measured. The electron transitions occur when the electron beam excites some electrons in the material to higher energy levels. When these electrons return back to their initial state, the energy difference is emitted as an X-ray. This X-ray emission is characteristic for each element and enables its identification. The SEM is equipped with an X-ray detector which is used to collect the emitted X-rays.

Transmission electron microscopy (TEM) uses a similar principle to the SEM but the electron beam has a higher voltage and penetrates an ultra-thin sample. A TEM is comprised of the electron gun, a column of electromagnetic lenses with a high vacuum (~ 10^{-7} Torr) and an imaging system [70]. The higher accelerating voltage for the TEM electron beam also decreases the electron wavelength and consequently increases the resolution of the microscopic image. In this case, not only the directly transmitted electrons can be detected, but also inelastically (with a loss of energy) and elastically (without a loss of energy) scattered electrons, Figure 2.2b. These can provide additional information about the presence precipitates and defects. The technique allows one to determine structural features, morphology, phase composition, chemical composition. The sample preparation process for the TEM is more complicated and requires a thinning of the investigating material, so that the electron beam can be transmitted through the sample.

The TEM uses information from the phase shift of the electron beam after interaction with the thin film. *The high resolution TEM (HRTEM)* uses two interfered electron beams transmitted through the sample to form an interference pattern at the atomic scale represented as fringes, the alternating dark and white spots with atomic scale resolution.

2.3 X-ray diffraction

X-ray diffraction is a non-invasive technique used to determine the crystal structure of a material. The X-ray has a wavelength in the range of few angstroms. The wavelength of the X-rays is much smaller than that of visible light implying higher energy of the rays and higher penetration depth. Once penetrated into the sample, the X-rays diffract from the atomic planes, Figure 2.4a. This is possible due to similar size of the interatomic planes compared to the wavelength of the X-rays. After this, a constructive or destructive interference is possible. If the X-rays diffract constructively the signal is detected by the detector and is recorded as spots of different intensities. As a crystalline sample must contain different types of planes with different spacings, the variation of the position and intensity of the spots will depend on the crystal structure of the sample. The diffraction angle 2Θ is recorded and displayed versus the intensity of the constructively interfered X-rays. Hence, collected information can provide information about interplanar distance, phase identity, and preferential growth orientation (if any) of the studied material. The sample can be prepared as a thin film or as a powder. Any crystalline material, whether metallic, organic or dielectric, can be studied.

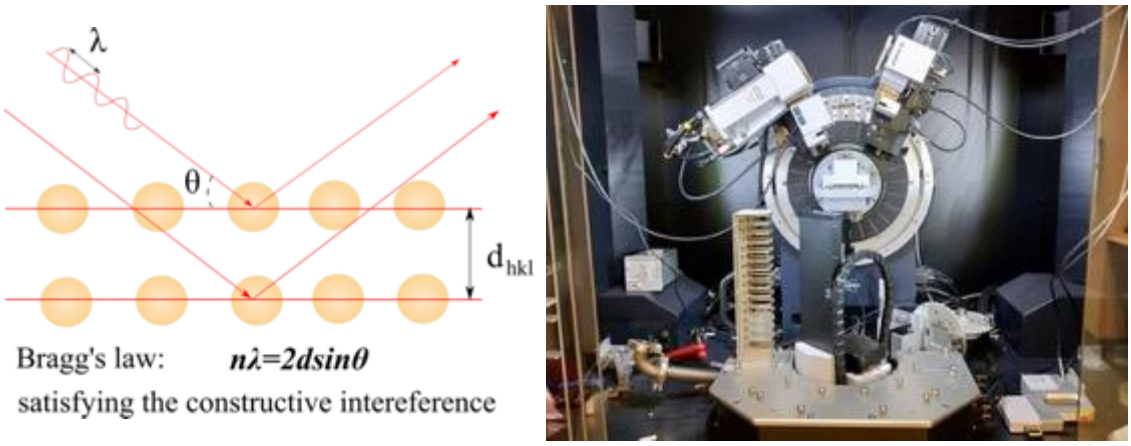

a) b)

Figure 2.4 – a) Schematic of the interaction of X-rays with the atomic planes satisfying the Bragg's equation for constructive interference b) XRD setup used to detect the crystalline structure of the samples

2.4 Spectroscopy

Spectroscopic measurements enable the determination of the optical response of a sample towards incident light of a certain wavelength range, in my case usually over the UV-vis-near-IR part of the spectrum. The measured spectrum is then displayed as an intensity of the reflected, transmitted or absorbed light versus wavelength (or equivalently versus photon energy, or photon frequency). The working principle of spectrometer is displayed in Figure 2.4a, where the main components are present. The measurement starts with the generation of polarized (s,p) or unpolarized light with a broad distribution across the spectrum (usually UV- near-IR). Then, the light is split into a nearly monochromatic beam by a prism and a slit. The slit is placed after the prism to select one particular wavelength, which later on strikes the sample. Finally, the reflected/transmitted light is collected by a detector.

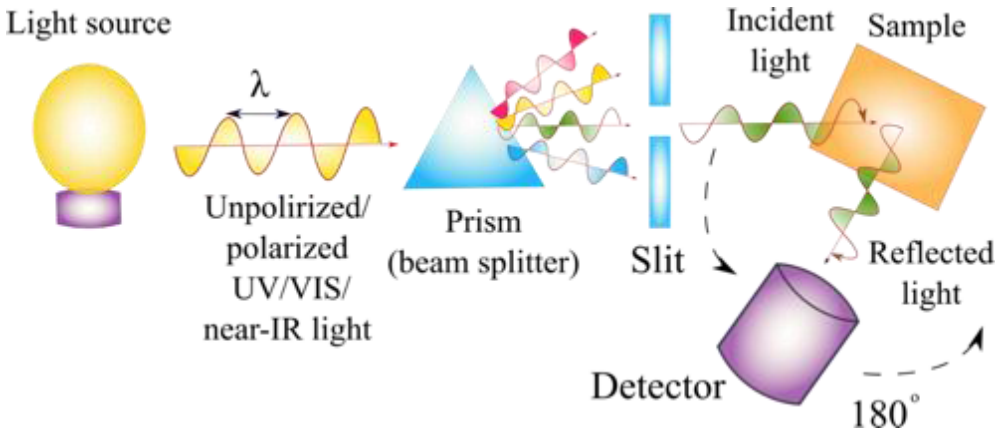

a)

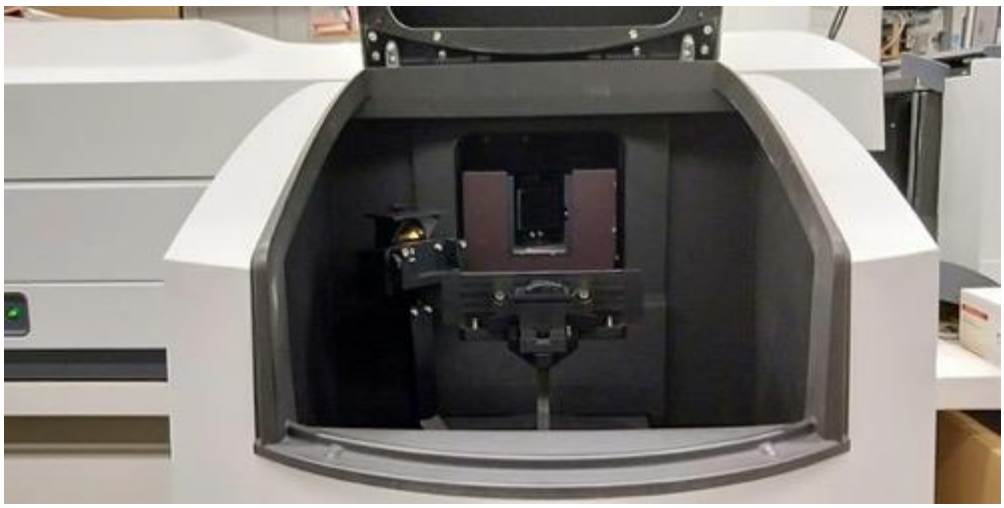

b)

Figure 2.5 – a) Schematic of the principle set up of the spectrometer b) The direct view optical design of the Agilent Cary 7000 Universal Measurement Spectrophotometer used to measure the reflectance/transmittance of the SSCs.

2.5 Ellipsometry

Ellipsometric measurements are a non-invasive optical method used to find the optical constants, thickness, or roughness of a sample. A schematic for this type of measurement is represented in Figure 2.6a and the actual set-up is shown in Figure 2.6b. First unpolarized light is generated by a light source, which is later on linearly polarized by the polarizer. This linearly polarized light strikes the studied sample, after which the polarization state changes into elliptical due to surface interaction with the material of a different optical density (this explains the name for the technique, "ellipsometry"). The phase and amplitude of the s and p component of the polarized light are changed in accordance with the Fresnel equations [71]. The angle of incidence is usually set in the 65º-75º range, as the light undergoes the biggest polarization change at these angles. After this, elliptically polarized light is analyzed by the analyzer (linear polarizer) and is collected by the detector (usually a photodiode is used).

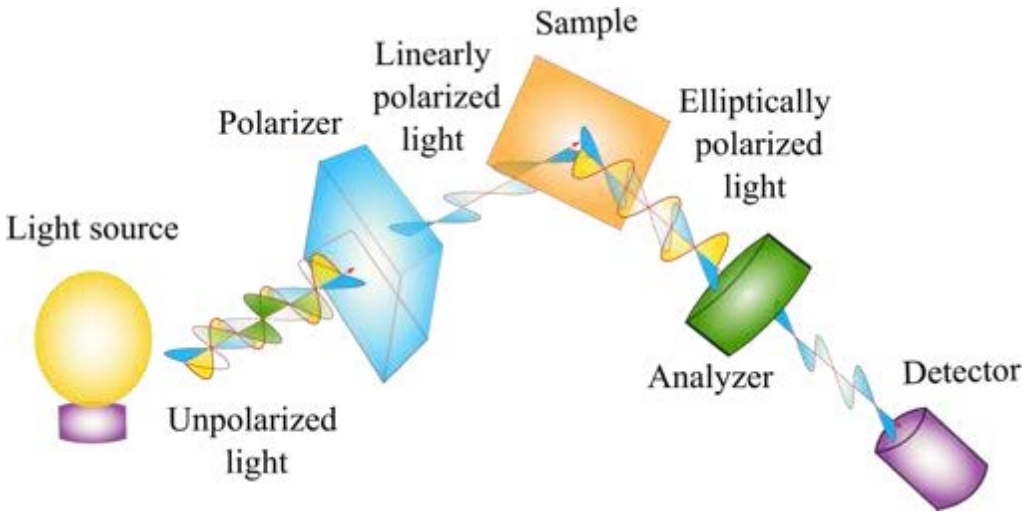

a)

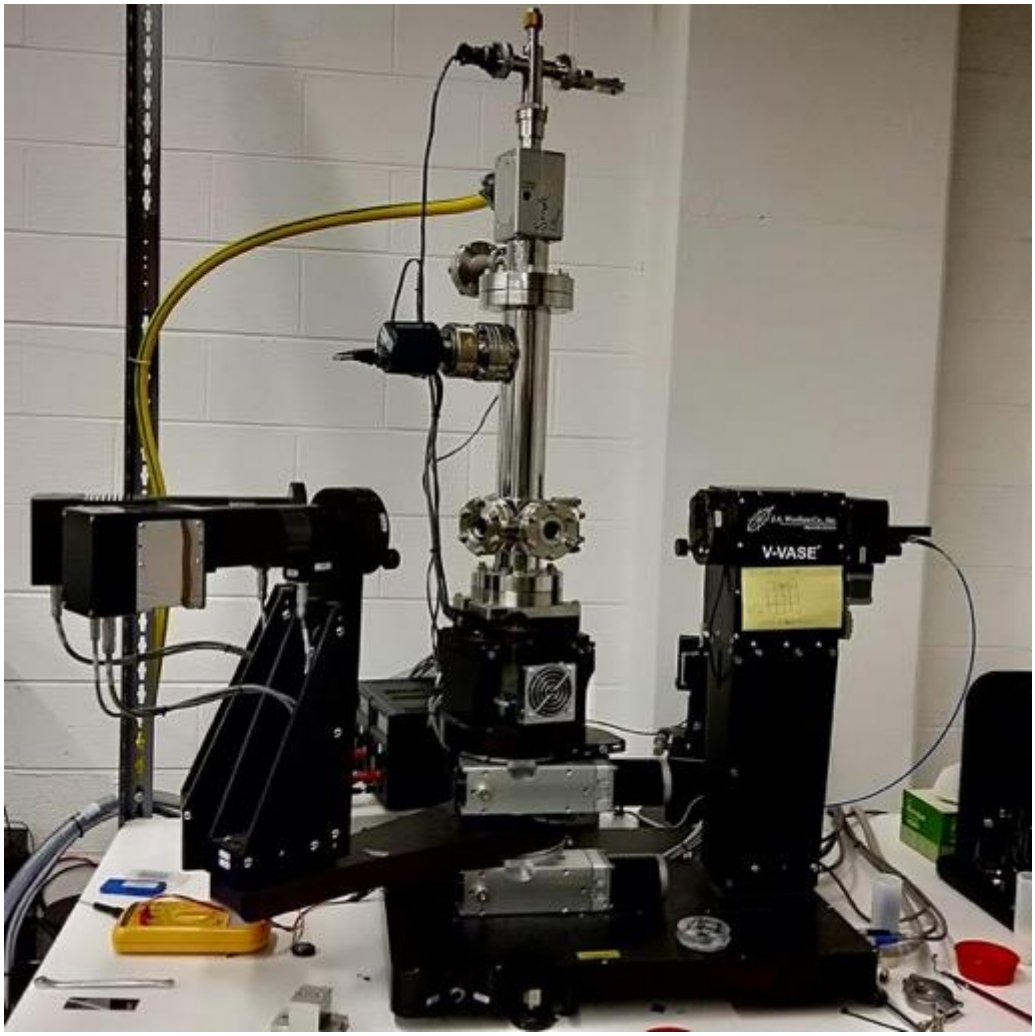

b)

Figure 2.6 – a) Schematic of the principle set up of the ellipsometer b) J.A. Woollam Co., Variable Angle Spectroscopic Ellipsometer (here with a thermal annealing set up) used to detect optical constants and thickness of the SSC

Hence, the main idea of the ellipsometric technique is to measure the polarization change of the light reflected from the sample. These polarization changes are defined by the ellipsometric parameters ($\Delta(\lambda)$ and $\Psi(\lambda)$ which are obtained by

$$\tan(\Psi)\exp(i\Delta)=R_p/R_s \qquad (2.1)$$

where Δ and Ψ are wavelength dependent and represent the shift in the phase and amplitude of polarized light after reflection from the sample; R_p and R_s are reflection

coefficients od p- and s- polarized light. Since Δ and ψ are obtained by a ratio of signal, they are insensitive to signal strength. Hence, the recorded data reflects the precise optical transitions in the sample during gradual annealing.

Determination of the optical constants is a multi-step procedure, Figure 2.7. Firstly, the ellipsometric parameters $\Delta(\lambda)$ and $\Psi(\lambda)$ are collected. After this, the WVASE software (J.A. Woollam Co.) is used to build a model of the studied material. This is possible by using library data for the optical constants for the known materials (dielectrics, semiconductors, metals etc.) in the coating and deriving the remaining unknown quantities. If a studied coating is complex and combines a few materials, then a general oscillator layer can be used for some unknown material. The oscillator model to describe the light-matter interaction would typically contain a Drude term (if it is a metal) and one or more Lorentz oscillators. There can be more than two oscillators, however, the fitting process should be conducted using the minimum number of oscillators, in order to obtain a physically meaningful description of the light matter interaction. Also, a model can contain an effective medium approximation layer (EMA) implying a complex structure of the studied sample, where two or more components are involved. This latter type of model is usually used for composites, where Maxwell-Garnett (M-G) or Bruggeman approximations can be applied. In the case of M-G, the complex medium is described as a host matrix containing dispersed inclusions with defined permittivity (M-G), while Bruggeman approximation does not separate medium into host matrix and inclusions and considers rather a smooth transition between two components of the medium, the filling factor of which does not comprise a striking difference.

After the appropriate model is selected and the best matching modelling parameters are generated, a set of complementary parameters can be found to fit to the measured experimental data. These includes thickness of each individual layer, oscillator parameters (amplitude, broadness, position etc.), filling factor for the M-G and Bruggeman approximations, possible addition of porosity or roughness layer and so on. If a perfect match of generated and experimental parameters is achieved the model should revised again to check whether the fitted parameters make physical sense. The parameters should not, for example, contradict information found by other techniques (SEM, XRD) or what is expected to be obtained from the deposition procedure. If all the mentioned parameters are in agreement, then the optical parameters and thickness can be considered

to have been correctly determined and can be used for further interpretation of the studied sample.

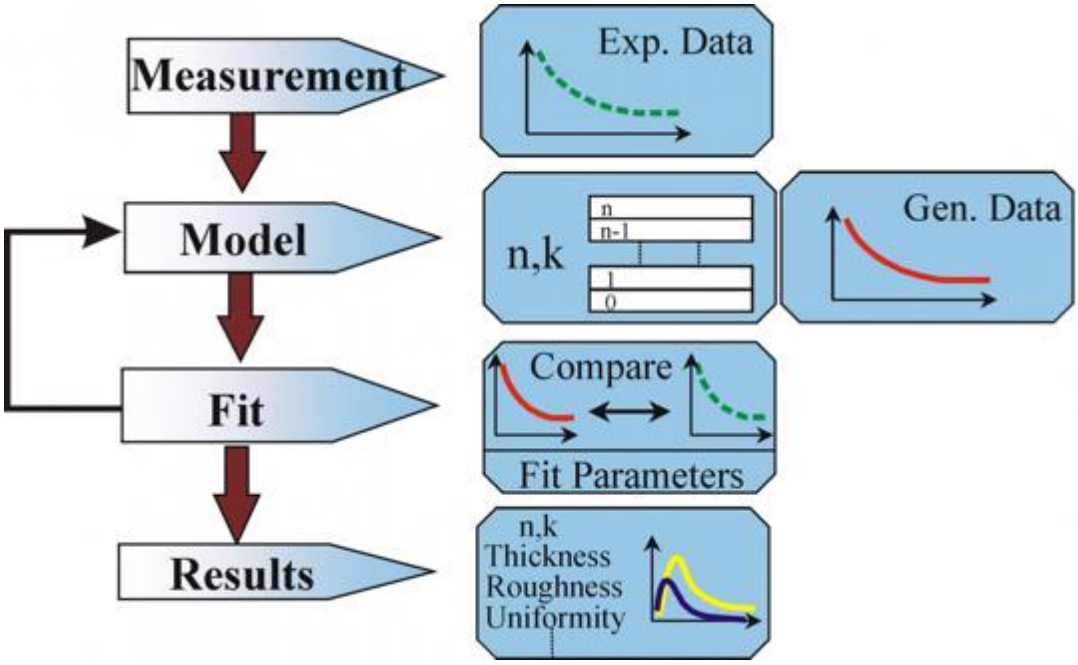

Figure 2.7 – Consequential step procedure to determine the optical constants and thickness of the measured sample using VASE Ellipsometer set up and software, retrieved from reference [12]

2.6 High temperature thermal annealing

The high temperature thermal annealing tests were performed using a custom-designed tube furnace displayed in Figure 2.8. The schematic in Figure 2.8a shows the internal view of the chamber with a heating stage made from carbon with a studied sample on top. The type-k thermocouple is attached to the stage for temperature detection. The chamber also has an exit to a turbo-pump vacuum system to achieve a high vacuum of the order of 10^{-6} Torr. In the current work, all the deposited coatings were annealed in vacuum with the value of ~10^{-5} – 10^{-6} Torr. A light source and a spectrometer were attached at the top of the chamber (the elongated tubes with a glass window at the top) providing in-situ reflectance measurement and monitoring of possible on-going optical changes during high temperature exposure of the sample, Figure 2.8b.

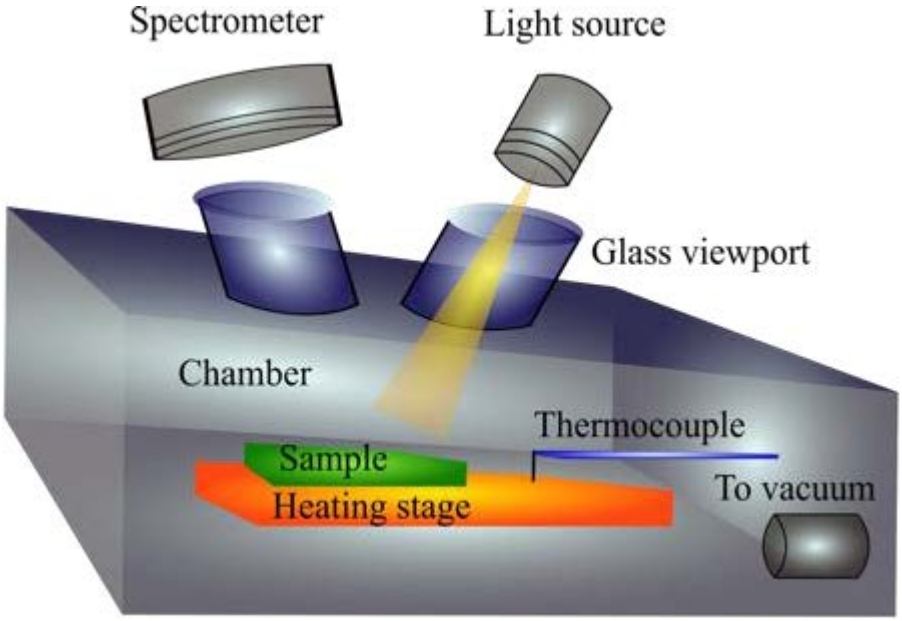

a)

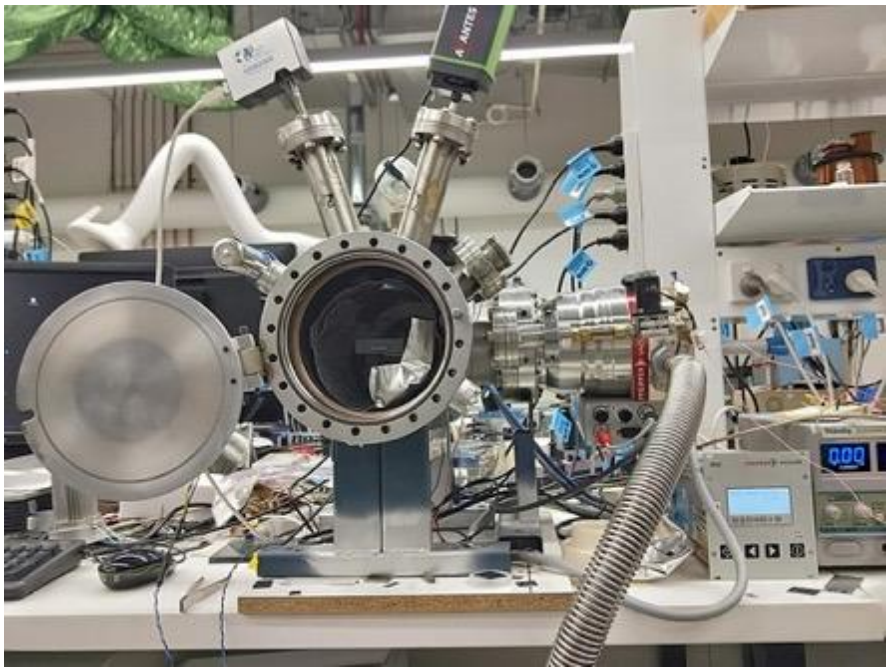

b)

Figure 2.8 – a) Schematic of the internal view of the annealing tube furnace b) Custom thermal annealing set up constructed by Dr. Angus Gentle for high temperature annealing of the samples

Chapter 3

Stacks based on $AuAl_2$:AlN for high temperature concentrated solar thermal applications

3.1 Introduction

As discussed in Chapter 1, many of the currently available solar absorbers use a cermet (a two-phase system consisting of metallic nanoparticles (NPs) dispersed within a ceramic matrix and mutually immiscible with it). This is due to the many advantages that a cermet can offer. Foremost amongst these is that the optical response can be tuned over a broad range by selecting the host matrix and metallic nanoparticles from a wide selection of candidate materials. The geometry and size of the metallic nanoparticles can also be varied, as can the density and thickness of the cermet layer. A cermet is a simple metamaterial: the composite behaves like a new material with properties unlike those of its constituent parts. The use of metal nanoparticles such as Al, W, Mo in a dielectric host has become the standard way to construct cermet coatings. The host matrix is usually provided by a temperature-stable dielectric oxide or nitride material. Al_2O_3, SiO_2, SiN, AlN, MgO, Cr_2O_3 are the most popular host materials and provide a matrix in which the atoms of enclosed nanoparticles have a low mobility. Further control of the optical response can be achieved by adjusting the volume percent of the metallic NPs, or by grading the cermet by changing the volume percent of the NPs through the layer.

Secondly a higher optical functionality can be provided by combining a cermet design with other types of spectrally selective schemes. Using a double cermet approach, with an intervening insulating layer, is effective due to interference effects enhancing solar absorptance if the correct thicknesses and metallic volume fractions of both cermet

layers are chosen. Deposition of additional AR layers also play a crucial role, hence, both thermal stability and reflectance reduction are secured.

Furthermore, the spectral selectivity can be further optimized to match the input spectrum if the metal nanoparticles undergo a localized surface plasmon resonance (LSPR) [72, 73]. In this connection, noble metals are of interest since they support a localised surface plasmon resonance (LSPR). The strength of the surface plasmon resonance depends both on the type of the matrix that was selected and the metal NPs. An additional role is played by the geometry and size of the metal NPs.

The ability to control each of these parameters opens a door for optimised performance of the SSC achieving higher structural stability and thermal tolerance, boosted absorptance in the solar part of the spectrum, and reduced emittance in the IR.

As an example, commercially available Mo:SiO_2-based cermet exhibits high α_s of ~95% in combination with thermal stability up to 600°C [74]. However, annealing at higher temperatures results in a decrease of energy conversion efficiency due to diffusion of Mo nanoparticles/atomic species in the absorbing layer. Mo nanoparticles may also be embedded in Al_2O_3, however, in that case the α_s of the stack did not exceed 90% [75]. Infrared emittance was 8% at 82°C, but will be higher at high operating temperatures due to two influences: (i) a fall in substrate IR reflectance due to nanoparticle coarsening, and (ii) a shift to shorter, more absorbing wavelengths in the Planck emission spectrum. As for Mo:SiO_2, a degradation in spectral selectivity of Mo:Al_2O_3 coatings was observed as a result of increased mobility of the Mo nanoparticles after annealing for 5 hours at 800°C [63]. Another problem that a cermet-based SSC may face is formation of the oxide layer around the metal NPs, as observed in case of the commercialized W:Al_2O_3 cermet [64].

Hence, one of the biggest challenges in designing the spectrally selective cermets for high temperature solar thermal applications is to prevent oxidation of the metallic NPs and their possible diffusion and mobility when exposed to thermal annealing. One of the solutions is to use noble metals as the encapsulated nanoparticles in the dielectric host due to their resistance to oxidation. In this case, the LSPR supported by a noble metal is preserved if the thermally activated mobility or coarsening of the NPs is prevented. So far a limited number of noble nanoparticle cermets have been proposed including Ag:Al_2O_3, AgAl:Al_2O_3, Au:MgO, Au:Al_2O_3, Au:SiO_2, and Pt:Al_2O_3 [65, 76-78].

Au-based cermet solar absorbing coatings have excellent oxidation resistance, but have shown a tendency to degrade during service at 400°C as the result of these latter phenomena [66, 79]. This is due to the extraordinary mobility of the Au atoms at

temperatures as low as 200°C which causes the Au particles to aggregate and coarsen to the point where they are no longer effective at absorbing the light [80-82].

In the study conducted here, it is shown how the mobility issue can be solved by stabilizing the Au NPs with Al by formation of an $AuAl_2$ intermetallic compound. This has the CaF_2 crystal structure with the Au and Al being located on specific sites inside the lattice of the compound. In this configuration, the diffusivity of Au is limited due to the stability of the ordered configuration of the $AuAl_2$ lattice structure.

It is worth noting that the LSPR of the newly formed $AuAl_2$ NPS will be somewhat modified and weakened compared to pure Au NPs [83], however, still contributing to absorptance in the solar range. Additionally, the weakened LSPR is compensated by the boosted thermal tolerance and structural stability due to retarded mobility.

AlN was selected for the matrix of the cermet-based SSC developed here. The AlN was selected due to its high resistance to spallation and mechanical damage, and its relatively low thermal expansion coefficient compared to other popular host matrixes like Al_2O_3 and MgO [84]. The exceedingly refractive nature of this dielectric – AlN melts at ~2600°C [84] – combined with the corrosion resistance of Au, seemed to offer an attractive pathway towards the development of improved solar thermal absorbers for use at temperatures up to 550°C. Only about 260mg of Au would be required per square meter in the coatings to be described below. Economic benefits accruing from having a higher performing coating will outweigh the cost of the Au content (about US$10/m2 of surface at a gold price of $40 per/g).

3.2 Experimental details

Three types of spectrally selective solar absorbing coatings, Figure 3.4, were deposited on Si substrates using a DC magnetron sputtering system without heating. Prior to the deposition process, the vacuum chamber was evacuated to a base pressure of 1.5×10^{-6} Torr (2×10^{-4} Pa). The Si substrates were ultrasonically cleaned in an acetone and ethanol bath for 40 minutes. High purity targets Au (99.99%) and Al (99.9%) with a diameter of 50 mm were used for sputtering. The targets were cleaned for 1 minute in Ar-plasma prior to the deposition. Ar and N_2 were introduced to the chamber at the pressure

of 1.3 mTorr and 1.2 mTorr, respectively. For cermet layers, co-sputtering of the metallic targets was performed. The Au and Al filling factor in the cermet layer was monitored by the input power applied separately to the targets at 0.01 A and 0.25 A, respectively. To achieve higher film uniformity, the substrate was rotated at 9 revolutions/min. The SiO_2 layer was separately deposited using an Edwards EO6 coater to achieve a high deposition rate. The dielectric target was 50 mm diameter and 99.99% purity, and had been Ar plasma cleaned for 1 minute. The substrate was at room temperature in all cases. A DC power supply was used at 0.25 A. Ar was introduced at 2 mTorr pressure. The thickness of the thin films was controlled using a quartz crystal monitor installed inside the deposition chamber.

In order to establish which of these stacks is the most suitable for mid- to high temperature solar thermal applications, the multilayer composites were first exposed to high temperature annealing for 30 minutes at 500°C in vacuum tube furnace pumped down to 10^{-5} Torr (1.3×10^{-3} Pa). The highest performing stack was also subsequently annealed for seven days at 500°C under the same vacuum. The evolution of phases of the heat treated samples was monitored using X-ray diffractometry employing a Bruker D8 Discover with LYNXEYE XE detector, Cu kα radiation (λ=1.54056 Å) operating at 40 kV and 40 mA and angle of incidence set at 8°.

To identify the microstructural features of the coatings, images of cross-sections were taken with a ZEISS EVO scanning electron microscope at 15 kV. Micrographs were colorized using Adobe Photoshop software to facilitate interpretation the SEM images. Four primary colors were used to distinguish each layer and processing was performed in "color blending" mode. To enhance image brightness gamma correction was made using "medium brightness (RGB)" mode.

The spectral reflectance was obtained using an Agilent Cary 7000 Universal Measurement Spectrophotometer (UMS) covering the 300-2500 nm wavelength range (angle of incidence 8°). The absorptance spectrum A(λ) was obtained according to the formula A(λ)=100%-R(λ)-T(λ) using measured reflectance R(λ) and transmittance parameters T(λ), where available. The emittance of solar absorbing coatings for solar thermal applications was measured using a custom-built emissometer heated to 82°C. The broadband thermopile sensor used detects thermal radiation over the 2.5 - 50 μm spectral range. The calibration of the instrument was conducted using an Au reference sample. Spectroscopic ellipsometry using a J.A. Woollam Co., Variable Angle

Spectroscopic Ellipsometer (VASE) was used for determination of the optical constants. The ellipsometric parameters were measured in the 300 - 2500 nm wavelength range in 5 nm steps at angles of 60°, 70° and 75°. High temperature ellipsometry was also conducted to obtain a deeper understanding of any optical changes due to temperature-induced chemical or structural changes inside each stack design. The changes in the optical response were recorded during both heating to 530°C and then the subsequent cooling cycle. The IR measurements up to 25mcm were conducted using Newport 8350 with custom build reflectance stage.

For a comprehensive analysis of these spectrally selective solar absorbers, a theoretical model of the stack was built using WVASE software (J.A. Woollam Co.). The generated results were fitted to the experimentally measured ellipsometric parameters and measured reflectance spectra, and then were displayed in terms of the final reflectance spectra for the best fit multi-layer model of the coating.

3.3 Characterization of a single layer Au/$AuAl_2$:AlN cermet

A cermet layer plays a crucial role in the cermet-based solar absorbing stack and defines the character of light-matter interaction and intensity of absorptance in the solar spectrum. The latter is strongly defined by the volume of metallic NPs present in the dielectric host matrix. The type of the dielectric is also important but plays a secondary role. As an example, it was shown in Thornton's work that the optical response of a Pt-based cermet absorber depended on the metallic fraction of Pt, where the optimal α/ε ratio was found for the cermet with 0.45 vol% - 0.55 vol% of Pt [85].

In the current work, in order to design a cermet-based stack, a single cermet was modelled first in the WVASE software (described in Chapter 2) using the Maxwell-Garnett effective medium approximation, where AlN was selected as a host matrix and Au was selected as a metallic NP inclusion. According to the model, the optimal optical response for the absorbing cermet was in the range of 18 vol% to 23 vol% Au. This model was tested by deposition of a single cermet layer with different filling factors of Au in the AlN matrix, Figure 3.1, followed by solar absorptance calculation of the cermet using formula (1.14). From Figure 3.1, it is seen that optimum does indeed lie in the range of Au volume fractions in the dielectric matrix of between 4vol% - 19 vol%. A further

increase in the Au percentage, above 25 vol%, does not contribute to enhanced solar absorptance of the cermet and leads to a vast degradation in optical performance. This can be explained by the partial or full agglomeration of the Au NPs and their local percolation, where they transit to a bulk-like behavior causing higher reflectance instead of optimized solar absorptance. Additionally, an unwanted rise in thermal emittance is expected. This type of behavior was observed in previous works, for example in a Ag:Al_2O_3 cermet-based SSC [86]. Hence, in the present work the cermet layer with nearly 20 vol% of Au was selected for a further deposition in the multilayer stack.

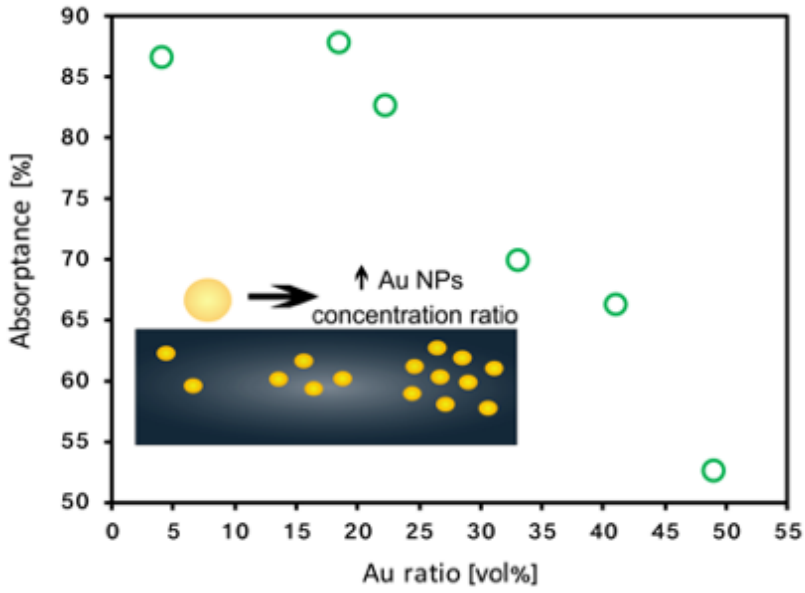

Figure 3.1 - The values of calsulated solar absorptance of a single Au/$AuAl_2$:AlN cermet layer calculated using measured reflectance/transimttance spectra with a varied Au content determined by WVASE software using MG and/or Bruggeman models .

Figure 3.2a shows the surface morphology of a single layer of Au:AlN deposited onto a Si substrate. The micrograph shows the presence of isolated Au-rich nanoparticles (white spots) in the dielectric matrix. The distribution of the metallic nanoparticles follows a random pattern, but is homogenous throughout the cermet layer with the absence of formation of any metallic channels. These dispersed Au-rich nanoparticles possess a spherical-like shape with the smallest size less than 5 nm and the maximum size of 11 nm. Such a system is well described by the Maxwell–Garnett theory, where the main criterion is to have a uniform but random dispersion of nanoparticles. The size of

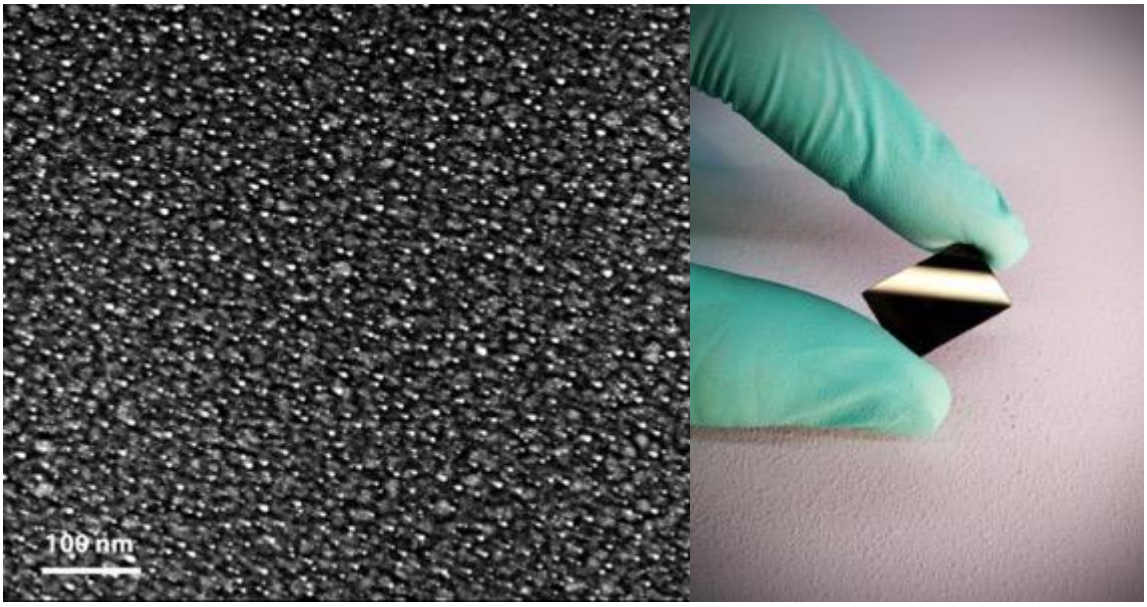

such particles should be smaller than the wavelength, while the filling factor of the Au-rich nanoparticles has to be below 25 vol% gold, as indeed is the case in Figure 3.1. Particle shape can be considered as ellipsoidal [87].

a) b)

Figure 3.2 – a) SEM micrograph of a single Au:AlN cermet layer b) appearance of a Au:AlN cermet layer deposited on a Si substrate

The annealing of the cermet was conducted at 500ºC for 1 hour in order to test the optical stability of the single absorbing layer. Figure 3.3 shows an absorptance spectrum of the Au/$AuAl_2$:AlN cermet layer with an optimal Au fraction of (19 vol%) before and after annealing. The LSPR peak centered at around 450 nm suggests the formation of $AuAl_2$ nanoparticles during a co-deposition of Au and Al targets in the N_2 atmosphere. (The position of the peak is in general agreement with a previous study on $AuAl_2$ [88].) The broadness of the peak is probably due to a wide variety of shapes and sizes of nanoparticles being present in the coating. In the current case, there may also be spherical Au particles present with an LSPR peak located at about 520 nm. This was supported by the ellipsometric model, which was constructed for a single Au/$AuAl_2$:AlN cermet layer, the details of which will be discussed later (section 5.1.4). Annealing of the sample at 500ºC leads to slight modifications in the optical response of the cermet layer. The LSPR

peak is still preserved, however, there is a minor reduction in the low-energy shoulder of the spectra, indicating possible thermally induced mobility of the metallic particles, regrowth and/or size modification. In the next section, I will show how even these small changes can be prevented so that the optical response of the cermet can be stabilized.

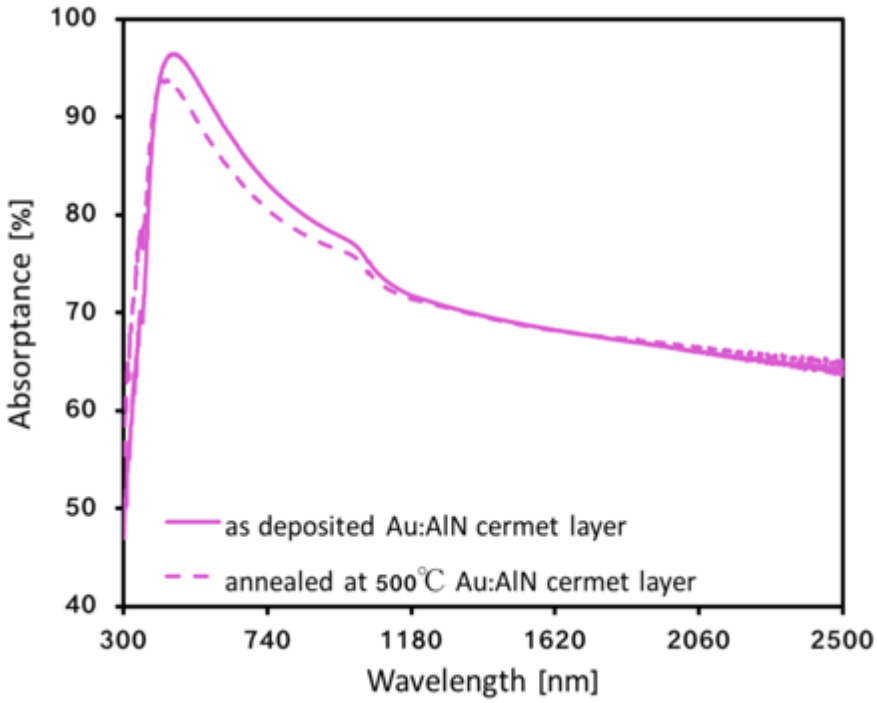

Figure 3.3 - Absorptance spectra of a single Au/$AuAl_2$:AlN cermet layer before and after annealing for 1 hour at 500ºC

3.4 Structural characterization of $AuAl_2$:AlN SSCs

Three different cermet-based spectrally selective multilayer coatings were designed and deposited using magnetron sputtering, Figure 3.4 and using an algorithm represented in Chapter 5, Figure 5.1. In all cases the intended application would be high temperature CSP. For convenience, the three different stacks will be labelled as *Stack 1*, *Stack 2* and *Stack 3*. Their detailed structure is provided in Table 3.1. All the stacks were deposited onto a Si substrate in order to conduct ellipsometric and spectroscopic measurements, however, the stacks can also be manufactured on stainless steel or other metallic substrates.

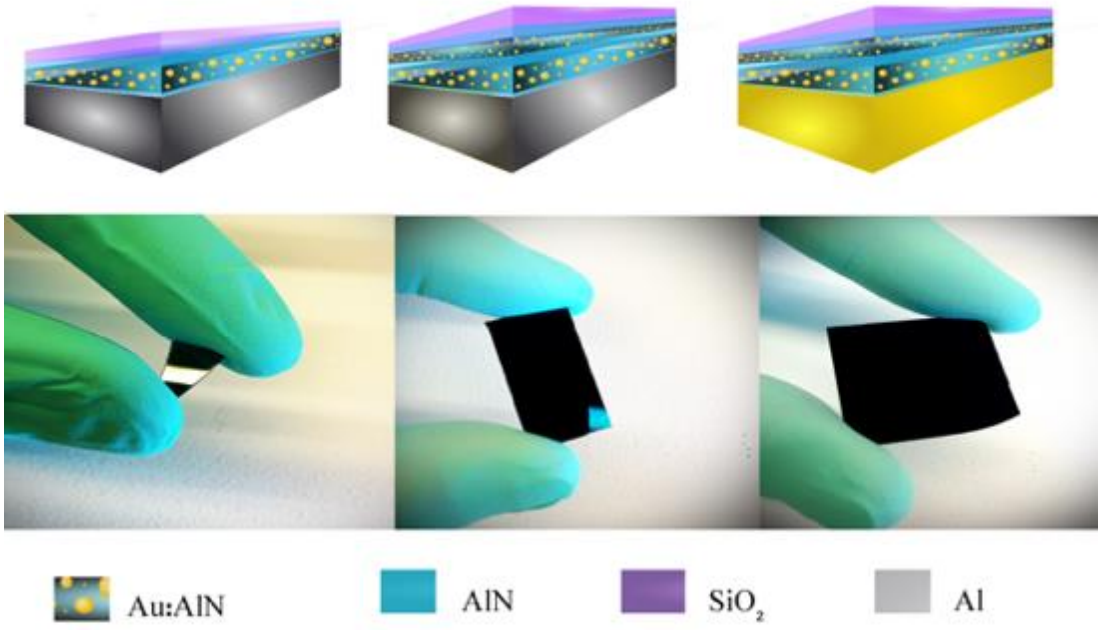

a) b) c)

Figure 3.4 – Design and top view of sputtered Au/$AuAl_2$:AlN cermet-based SSCs described in Table 2. a) Stack 1, b) Stack 2, c) Stack 3.

Table 3.1 - Description of the individual layers, function and thickness in each of the three stacks. Above the Si substrate, Stack 1 has five layers, Stack 2 seven layers and Stack 3 eight layers.

Layer number	**Compound**	**Function**	**Stack 1**	**Stack 2**	**Stack 3**
1	Si substrate	Substrate	1 mm	1 mm	1 mm
3	AlN	diffusion barrier	-	-	130 nm
2	Al	IR reflector	65 nm	100 nm	-
3	Au	IR reflector	-	-	50 nm
4	AlN	diffusion barrier	8 nm	8 nm	8 nm
5	Au-$AuAl_2$:AlN	solar absorber	80 nm	45 nm	45 nm
6	AlN	anti-reflector chemical barrier	47 nm	20 nm	20 nm
7	Au-$AuAl_2$:AlN	solar absorber	-	20 nm	20 nm
8	AlN	anti-reflector	-	20 nm	20 nm
9	SiO_2	anti-reflector chemical barrier	68 nm	68 nm	68 nm

Stack 1 was designed using a single cermet layer approach, while Stack 2 and Stack 3 had two cermet layers without any grading of the layers. Stack 1 and Stack 2 used Al as a back reflector securing low thermal emittance. Further, it will be shown that another purpose of the reflective Al layer is structural stabilization of the stack, in particular the main absorbing cermet layer, at higher temperatures. Stack 3 was deposited following same structure as Stack 2, apart from the back reflector. In this case, Au was used instead of Al in order to test the stabilization function of the Al in the designed cermets. An additional AlN layer was deposited between the Au reflector and the Si substrate for the Stack 3 to prevent the eutectic reaction between the Si substrate and the Au layer at 363°C. This also prevents the formation of SiO_2 layer on the Au side, which could have led to the degraded reflective performance of the Au layer [89].

All the three stacks used AlN and SiO_2 as then two top antireflective coatings with the SiO_2 top layer serving as a protection against oxidation and deterioration of the stack during high temperature exposure. Other transparent oxides can be also used, however, SiO_2 or Al_2O_3 have gained the most popularity among researchers.

X-ray diffraction patterns were collected for the three coatings (Stack1, Stack 2, Stack 3) in order to identify any phases present in the deposited stacks. These are shown in Figure 3.5.

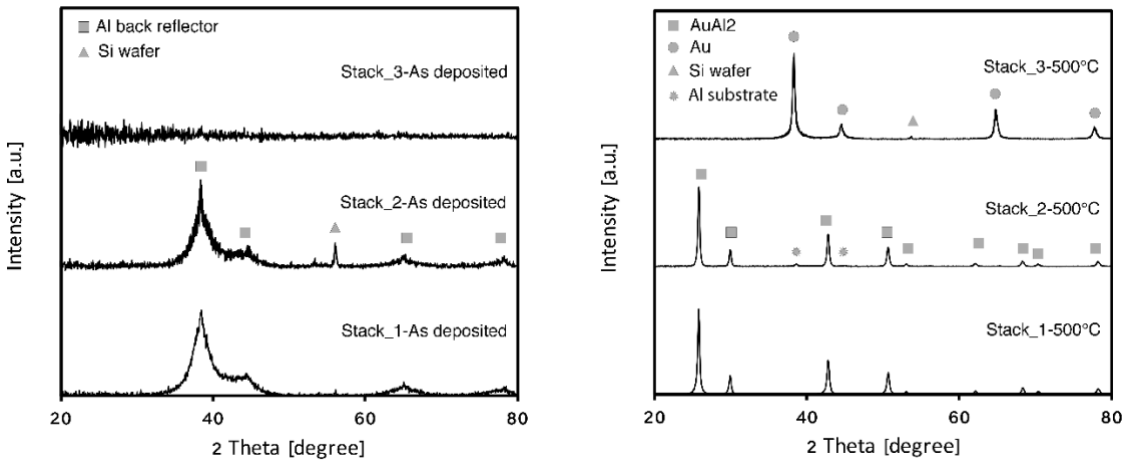

a) b)

Figure 3.5 – XRD patterns of the Au-$AuAl_2$:AlN solar absorbing coatings deposited on Si substrate, a) before and b) after annealing at 500°C. Note that the vertical scale of (a) is much less than that of (b).

The *as-deposited* multilayer samples do not show any peaks attributed to the phases that could be present in the absorbing cermet layer or dielectric layers, implying an amorphous nature, Figure 3.5a. By comparison of the patterns for Stack 1 and 2, on the one hand, and Stack 3 on the other, it can be deduced that the broad peaks of the former are from the Al reflecting layer. The broadness of the Al peaks is a characteristic of poorly crystallized phases. In contrast, Au back reflector layer of Stack 3 has remained nearly amorphous due probably to the much higher melting point of Au than Al (Figure 3.5). No peaks were identified for the encapsulated metallic nanoparticles. This could possibly be due to their very small size (<10 nm according to Figure 3.2).

Figure 3.5b shows the XRD the newly formed diffraction peaks of the *annealed* versions of the three coatings. No crystallization of the host dielectric matrix and other dielectric layers has occurred, and they remain amorphous in nature. However, there is an obvious formation of the $AuAl_2$ phase observed for Stack 1 and Stack 2 which have Al as the back reflector, while no $AuAl_2$ formation is indicated for Stack 3, which has the Au back reflector.

From this point, three competing theories could be proposed: 1) formation of the $AuAl_2$ phase due to Al from the AlN host matrix reacting with the Au, or 2) formation of the $AuAl_2$ phase due to Al from the reflective layer diffusing up to react with the Au, or 3) Al from an Al-rich AlN matrix reacting with the Au to form $AuAl_2$. The first theory can be discarded as AlN has a more negative Gibbs free energy formation than $AuAl_2$: the negative heat of formation (ΔH) is -31 kJ/mole for $AuAl_2$ *vs* -218 kJ/mole for AlN, indicating that AlN is in lower energy state or has a lower potential energy than $AuAl_2$, and is therefore much more stable. It is not possible that Au would remove Al from AlN [90]. Hence, there are two assumptions left, that $AuAl_2$ formation is due to a flux of Al from an Al-rich AlN matrix or that it is from the Al back reflector. Analyzing diffraction peaks for the Stack 3 after annealing sheds a light on this situation. As shown in Figure 3.5, no $AuAl_2$ was formed in Stack 3 (which had the Au reflector) in contrast with Stack 1 or Stack 2 (which had the Al reflector). Instead, Stack 3 just has Au peaks arising from either the crystallization of the Au reflector or from Au NPs within AlN matrix. This is proof that the main source of the Al used to form $AuAl_2$ came up from the Al IR reflecting layer.

The upward diffusion of the Al into the cermet absorbing layer is secured by thermal treatment of the stack at 500°C. Furthermore, the difference in thermal expansion

coefficients between the Al and the Si substrate will generate a stress distribution. This has been reported to facilitate outwards diffusion of Al in bilayered Ag/Al coatings [91]. A secondary contribution may still come from the Al-rich AlN matrix due to short distance interaction of the Au NPs and the excesses of the Al from the host.

During the thermally activated diffusion of the Al from the back reflector, a thin diffusion barrier film represented by AlN, Table 2, becomes "transparent" to the Al flow due to its small thickness, 8 nm. A similar phenomenon was observed in Gao's work, where thermal migration of the Al from the back reflector was observed to react with Ag NPs in the overlying Al_2O_3 matrix [78]. In our case, this is a desirable effect because the formation of $AuAl_2$ stabilizes the metallic NPs. The result also points out the inadequacy of a diffusion barrier of only 8 nm. It should probably be at least 25 nm if no flow of Al is required.

Figure 3.6 shows the colorized SEM cross-sectional micrographs for as-deposited and annealed cermet-based stacks. In all three pristine multilayer coatings, the Au NPs are readily observed inside the amorphous AlN host. The cross-section views are in agreement with morphological view for a single Au/ $AuAl_2$:AlN cermet layer, Figure 3.2a, and reflect that all the Au NPs are spherical in shape with the size distribution between 3 nm and 12 nm. The distribution of the particles is relatively uniform, and unlike the gradient normally seen in many other cermets. The interfaces between the layers are explicit and clear, indicating no interdiffusion during the deposition process.

After annealing the structural integrity of the top AR thin films (AlN and SiO_2) was unchanged, and they still exhibited clear interface boundaries. Analysing the bottom layers of these two stacks, one can conclude that there is no strongly defined diffusion area for the exchange interaction between Au and the Al from the IR reflective layer after the heat treatment. However, an incorporation of the Al atoms from the Al reflective layer into the Au-$AuAl_2$:AlN cermet and a consequential formation of the bimetallic $AuAl_2$ is supported by an increase in the thickness (from 80 to 90 nm as measured in SEM cross-sections) and the presence of the cavities in the main absorbing layer after annealing at 500°C. The cavities may be due to the Kirkendall effect, a phenomenon governed by the difference in the diffusion rates of two adjacent metals [92]. The result of a faster diffusion of one of the metals is represented by the formation of the characteristic vacancies which move into the opposite direction and are known as Kirkendall's voids, Figure 3.6d. A further agglomeration of voids in specific locations occurs here as, according to Figures 3d and 3f, the distribution of holes is inhomogeneous. Randomly

distributed stresses throughout the layer may also result and help to drive void formation. According to Egami, the defects in amorphous media include low-symmetry regions with high stresses [89]. It is believed that these regions can also be the nucleating points for the Kirkendall hole growth (Figure 3.6d).

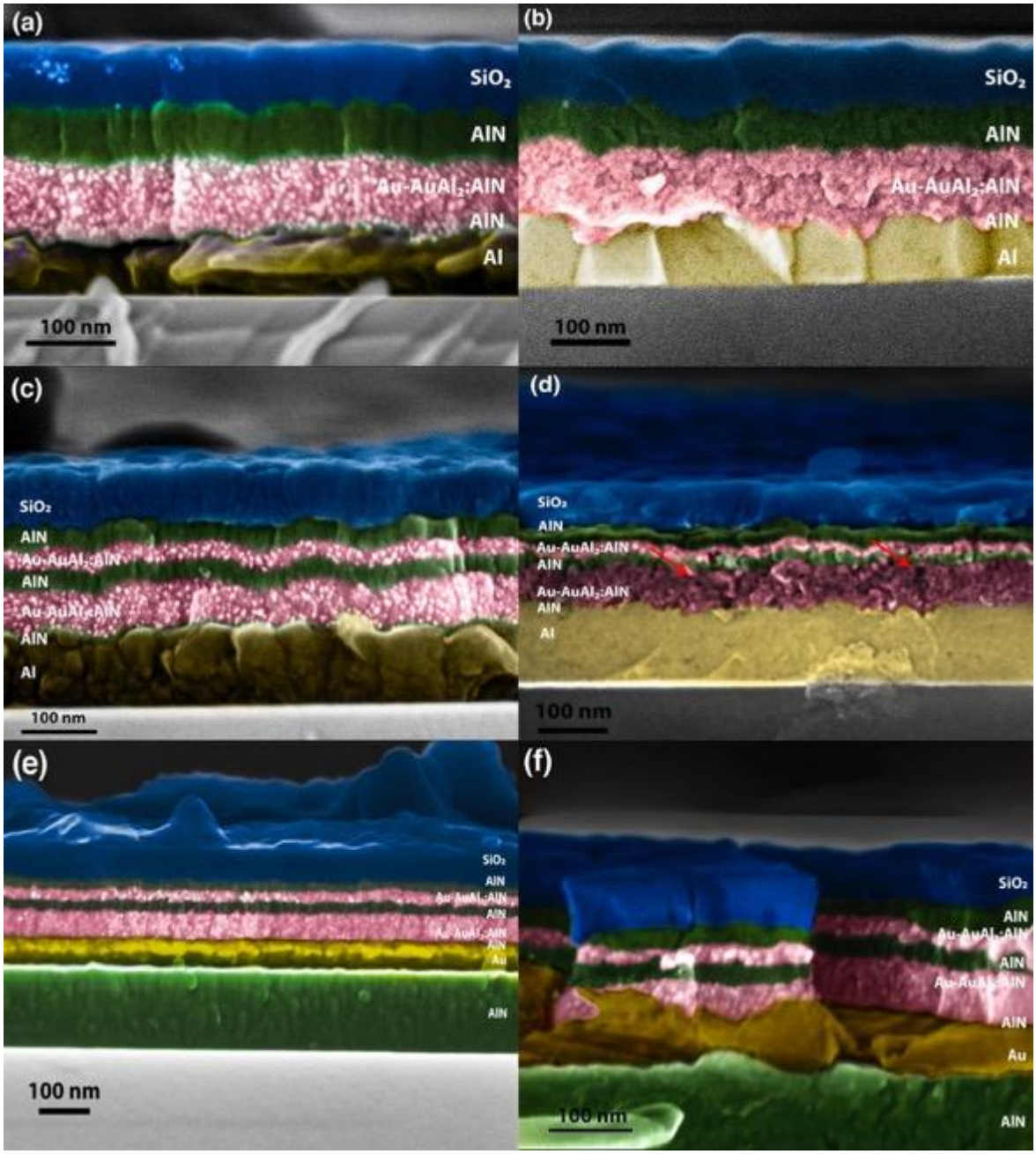

Figure 3.6 - Cross-sectional colored micrographs of single and double Au-$AuAl_2$:AlN cermet layer stacks. The left hand images are in the as-deposited state, the right-hand images are for samples after annealing at 500°C, (a,b) single layer on Al, (c,d) double layer on Al, red arrows indicate the Kirkendall voids, (e,f) double layer on Au.

In case of the cermets using gold particles above a gold substrate, the Kirkendall voids are not formed, as expected. Furthermore, a substantial supply of Al atoms is desired to react with the Au NPs in the AlN matrix. This is further supported by the lack of alloy formation in the top cermet layer in any two cermet layer stack, as evidenced by the lack of Kirkendall voiding in the upper cermet layer and its retention of high contrast nanoparticles. The contrast in the internal nano-structure within the two cermet layers after annealing is seen in Figure 3.6d but not in Figure 3.6f. The poor adhesion strength of the Au reflector in Stack 3 is obvious after the heat treatment and results in the delamination of the Au layer, intrinsic stresses in the deposited multilayers, crack formation and finally partial peeling of the upper layers. To prevent this problem, an adhesion layer made from Ti can be deposited below gold in any future work.

The top two antireflective layers AlN and SiO_2 remained unchanged after being heat-treated. Here, the SiO_2 layer performs its function and protects the lower layers from oxidation, Figure 3.6b,d.

3.5 Optical characterization of Au/$AuAl_2$:AlN SSCs

The potential efficiency of a coating for use in solar concentrated power systems operating at elevated temperatures can be estimated from optical measurements made at room temperature. Ideally, however, optical measurements are also needed at the operating temperatures, but these are rarely available. Here we begin by assessing the room temperature properties of the Au/$AuAl_2$:AlN samples before moving on to their properties at temperature.

Once the optical measurements have been made then a refractive index/extinction coefficient model is fitted to each layer of the coatings as described earlier in Chapter 2. Examination of these models can provide insight as to how to achieve efficient optical performance in a solar concentrator design. The optical constants, n and k, should be correctly selected for each specific layer performing a certain function, such as reducing front reflectance or intensively absorbing light in the solar spectrum. One of the strategies for achieving effective solar absorptance is to create a grading of the refractive index throughout the SSC. The idea is to increase impedance matching by gradual decrease of the refractive index, starting with a high value in the layer closest to the IR reflector and

then reducing it going towards the top of the coating. This is especially the case for the cermet-based coatings, where the refractive index of the cermet layer can be smoothly varied by an addition of the metallic particles. Figure 3.7a shows the implementation of this approach in the single cermet Stack 1, where the optical constants were determined by the ellipsometric measurements (the model of the stack will be discussed further later). The second approach employs destructive interference between two layers as discussed in the *metal – dielectric tandems* section above, with the main absorptance occurring in two cermet layers separated by a non-absorbing dielectric AlN layer (k=0) as shown in Figure 3.7b. Each layer fitted to determine the n,k was simultaneously deposited on a separate substrate to achieve the highest possible precision in determination of the optical properties of each layer in the stack.

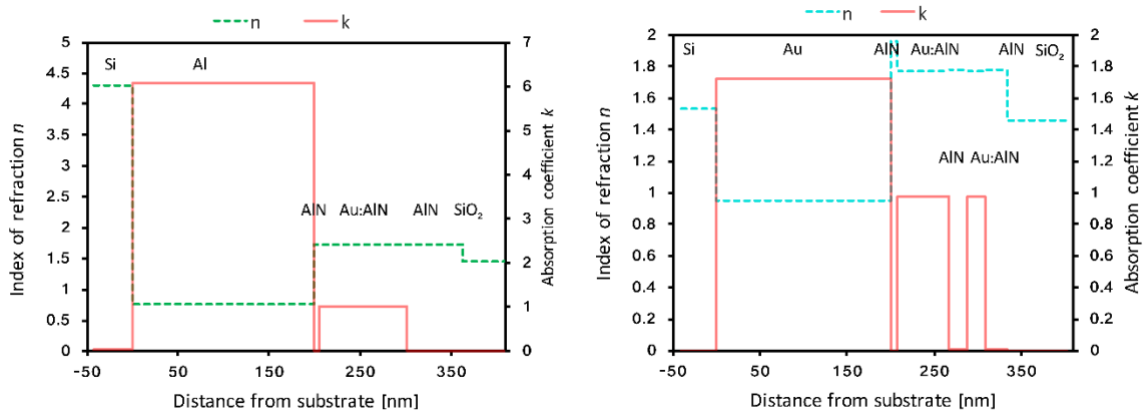

a) b)

Figure 3.7 – Refractive index and extinction coefficient values at 300 nm for a) Stack 1 and b) Stack 3 as a function of a distance from the Si substrate to the top of the coating

The model for cermet absorber layer included four components whose composition was fitted using a two-step Maxwell-Garnett effective-medium approximation (EMA), with an explanation provided further. Firstly, the EMA model was determined for the matrix only and then defined n,k were used to create an EMA model for the whole cermet including metallic nano-particles. The refractive indices for the purely dielectric layers (i.e. no Au added) could be modelled in two ways: a multi-oscillator model (some of which represented the effect of point defects), or as an effective medium composed of just 4% (by volume) of elongated Al metal in an AlN host. The latter can be indicative of

a metal-rich stoichiometry in the AlN and should not necessarily be interpreted literally as discrete Al nanoparticles in a pure AlN matrix.

Once a model for the AlN had been found, the next step was to develop a model for the cermet. The inclusion of gold particles alone into the above AlN matrix did not provide a fit to the cermet layers indicating that there was some missing factor. Empirically, it was found that also adding in some $AuAl_2$ nanoparticles along with 5.5 vol.% of voids yielded a high accuracy fit to the experimental ellipsometric parameters. The Au and $AuAl_2$ nanoparticles had volume fractions of 20% and 18% respectively in the as-deposited AlN:Al host. It appears that a reaction of the Au atoms with an excess of mobile Al atoms already occurs during the deposition. This is probably linked to the mobility of both Al and Au on the substrate and is in agreement with previous studies that poorly crystallized or defective $AuAl_2$ can be deposited by magnetron sputtering at room temperature [88, 93]. Formation of the well crystallized $AuAl_2$ that is detectable by XRD will occur once the deposit is annealed at higher temperatures [83].

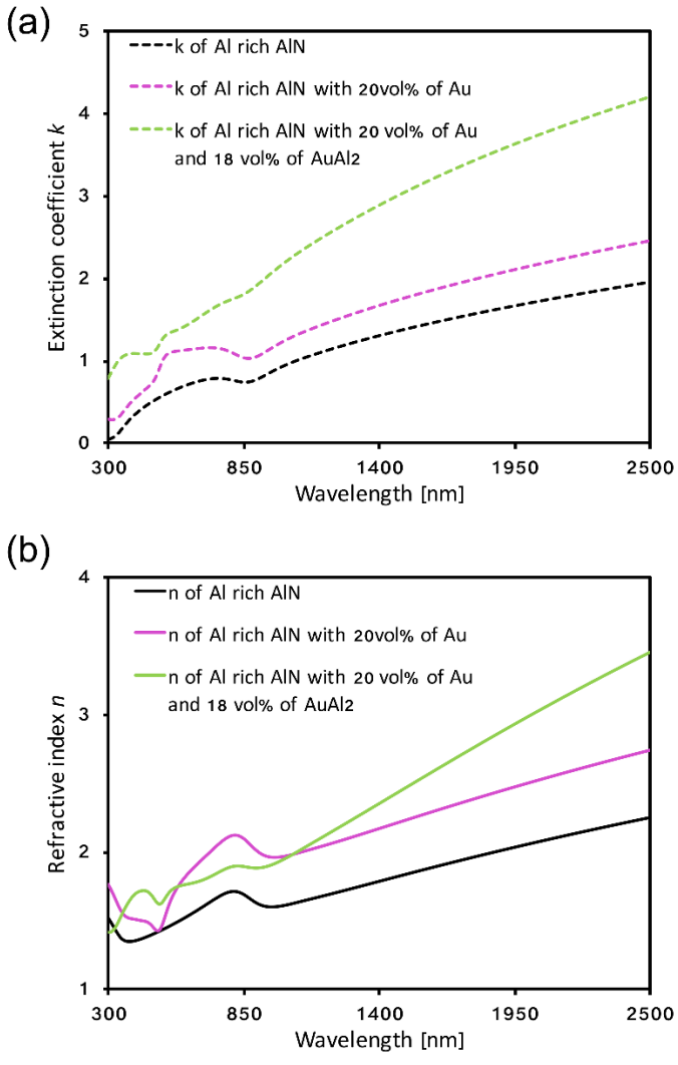

Figure 3.8 - Variations of experimentally determined a) extinction coefficient values and b) refractive index values for the as-deposited Au-$AuAl_2$:AlN cermet with addition of the Au (20 vol.%) and $AuAl_2$ (18 vol.%) nanoparticles into the AlN_{1-x} matrix. The matrix used is Al-rich.

The distribution of pores is supported by the spectral evidence and was well fitted using Maxwell-Garnett theory, where the "pores" or "voids" were added to MG theory for the stack 1 and stack 2 as a third component with the n,k data taken from the WVASE library. Figure 3.8 shows the evolution of the extinction coefficient *k* with sequential additions of the Au and the $AuAl_2$ NPs into the Al-doped AlN layer.

From these spectra it can be concluded that solar absorption is boosted further when $AuAl_2$ nanoparticles are present in the dielectric matrix in addition to Au NPs. Spectral details show this clearly, with a narrow extinction peak centered at around 480 nm plus a broad absorption peak at longer wavelengths, Figure 3.9. This broadening suggests that the presence of nanoparticles of both Au and $AuAl_2$ are needed to achieve the required high solar absorptance.

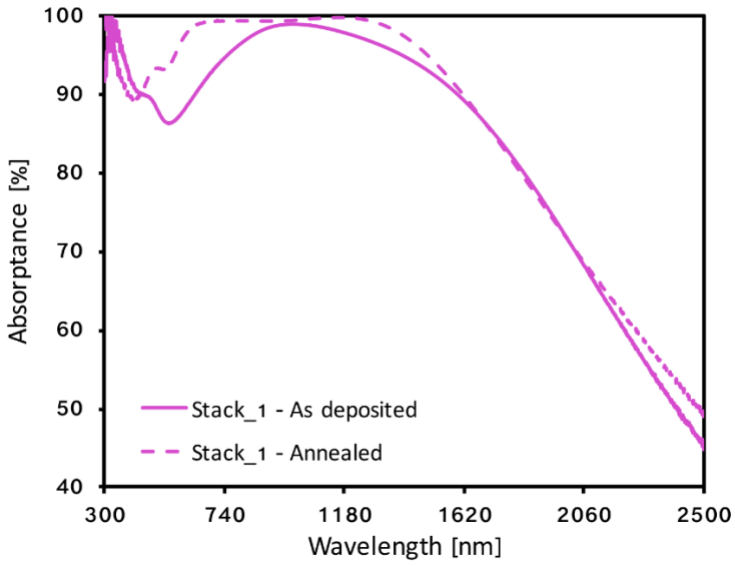

Figure 3.9 - Absorptance spectra of a single cermet Au-$AuAl_2$:AlN multilayer solar absorbing stack

Simulated reflectance spectra as a function of angle are displayed in Figure 3.10. It is worth noting that obtaining a higher overall efficiency of the absorber for certain focusing optics and for a stationary heat collector requires that the maximum absorption should persist out to high incidence angles. For high temperature work two-axis tracking of the

sun is possible, but single axis tracking is preferable due to reduced costs of the system [94]. In this connection, the heat output performance is affected by the incidence angle of solar radiation due to dependence on the location and site latitude [95].

The modelled reflectance spectrum was obtained in the WVASE software using the optical constants of the single layers determined by fitting experimentally measured reflectance spectra generated in the 8º - 80º incident angle range. A parallel fit of the ellipsometric parameters and experimental reflectance spectrum at normal incidence was also conducted for higher accuracy, Figure 3.11. Both modelled and experimental reflectance spectra at different incident angles display a similar trend. This would not be the case if the optical constants that had been determined were inaccurate.

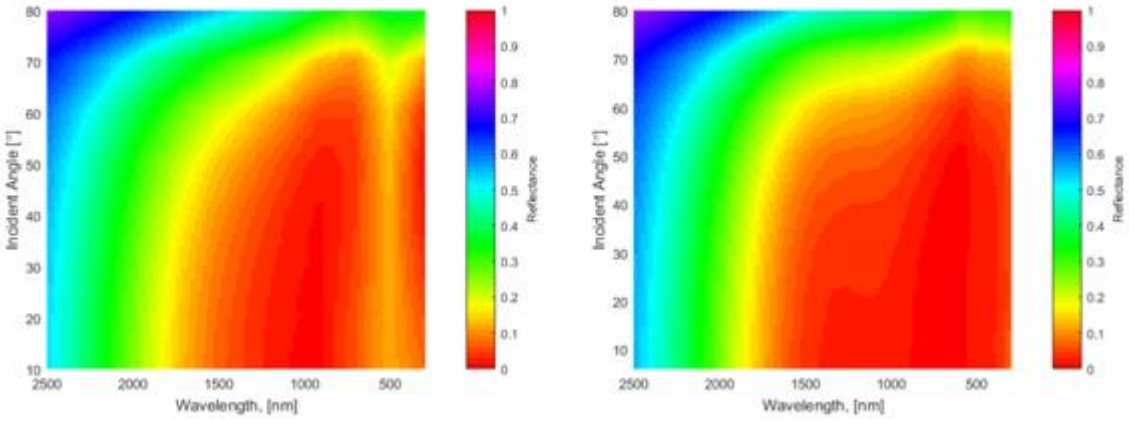

a) b)

Figure 3.10 - Modelled angular reflectance spectra of a Au/AuAl$_2$:AlN nano-cermet solar absorbing coating using WVASE software for a) Stack 1 b) Stack 2

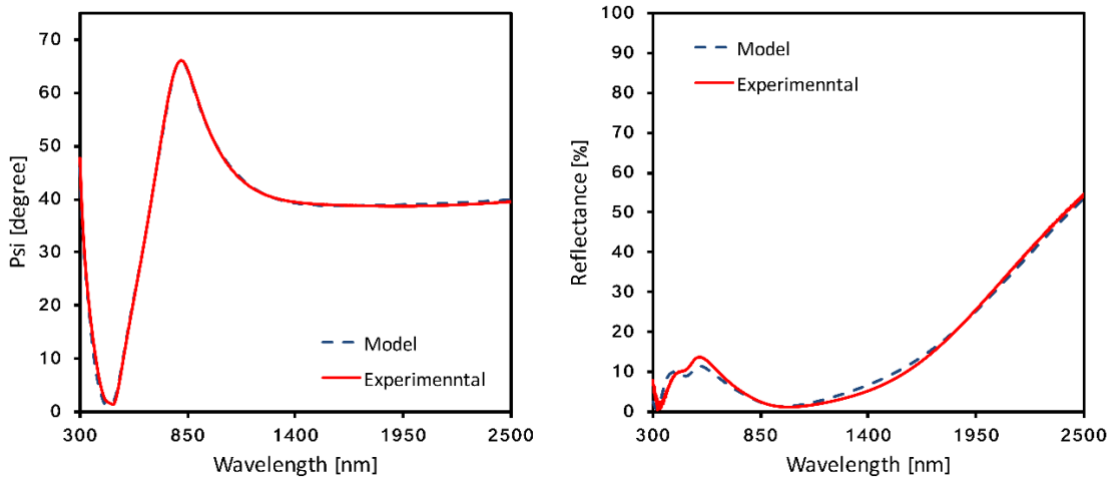

Figure 3.11 - The results of parallel fitting of (a) ellipsometric and (b) spectroscopic data for the as-deposited Au-$AuAl_2$:AlN single cermet stack

A minimum value of spectral reflectance was achieved across the 300 to 1700 nm wavelength range at all incidence angles from normal incidence to 70º. As a result, solar absorptance is also maximized. Beyond 1700 nm reflectance increases, reaching around 60% at 2500 nm. This is beneficial as it will enable a low emittance in the IR range. This combination ensures excellent spectral selectivity for the $AuAl_2$:AlN solar absorbing coating. This result is comparable with that of Zheng for a Mo:SiO_2 double cermet solar absorber and Tesfamichael's study for a Ni:NiO_x solar absorbing coating [96, 97]. In both of those studies an increase in spectral reflectance of at least by 20% is observed after surpassing the 50º incidence angle. This can be explained in part by the variation in interference effects between the two separated cermet layers, which vary with the angle of incidence [98]. The strongest interference effect is observed for angles close to normal incidence. In addition, the solar power flux is a function of incident angle and approximately follows Lambert's cosine law (equation (3.1)) due to the variation in the area illuminated obliquely. Additional solar attenuation comes from the thicker atmosphere at incident higher angles. The projection impact is given by

$$I(\lambda, \theta) = I_0(\lambda)cos(\theta) \tag{3.1}$$

θ is an incident angle of the solar radiation, I_0 is the intensity in the incident beam radiation and I is the intensity of solar radiation falling obliquely onto the surface.

The overall analysis of the reflectance – incident angle data shows that the Au-$AuAl_2$:AlN cermet coatings are broad-angle solar absorbers, enabling them to harvest a high fraction of solar radiation over a broad angular range from normal incidence to about 70º incidence. If used in a tracking solar heating system, this coating will be highly efficient all day, and even if used in a stationary absorber acting at lower temperatures (for example for industrial heat collection) it will be efficient over much of the day. The high intrinsic solar absorptance of the Au-$AuAl_2$:AlN cermet along with interference effects enabled by the multilayer structure leads to this excellent performance.

3.6 Thermal stability and optical response at high temperatures of $Au/AuAl_2$:AlN SSCs

Next, we annealed the coatings at 500°C and then made room temperature measurements of the integrated solar absorptance and thermal emittance (Table 3). Annealing was conducted in a vacuum ambient to test the potential for use in evacuated tube parabolic trough solar collectors. Key absorption coefficients were collected as a function of a wavelength and are displayed in Table 2.2. Stack 1 was clearly superior under the conditions of interest. Its efficiency of heat generation was evaluated using Equation (1.13).

Table 2.2 - Effect of a 30 minute heat-treatment at 500°C in vacuum. The parameters assessed are solar absorptance and IR hemispherical emittance.

Sample	As Deposited			After annealing for 30 minutes at 500°C			
	Absorptance α_s	Emittance $\varepsilon_{82°C}$	Efficiency η	Absorptance α_s	Emittance $\varepsilon_{82°C}$	Emittance $\varepsilon_{500°C}$	Efficiency η initial, (500°C)
Stack_1	92%	4.7%	90.8%	95%	13%	20.65%	90.8%(89.9%)
Stack_2	97%	3.5%	-	94%	21.2%	-	-
Stack_3	95%	2.3%	-	91.9%	26%	-	-

*Emittance at 500°C was calculated using formula (1.15)

Finally, *in-situ* high temperature ellipsometric measurements were made to dynamically track optical transformations as the heat-treatment progressed. Figure 3.12 illustrates dynamic *in situ* ellipsometric studies of the optical response changes inside Stack 1 and Stack 2 as they are the main interest here. Since the collected results are time-dependent, ellipsometric parameter (Ψ) at several representative wavelengths 300, 500, 1000, 1500, 2000, and 2500 nm (primary *y* axis) and annealing temperature ramp (secondary *y* axis) are plotted versus time.

The dynamic ellipsometric results can be separated into four main regions according to observed properties. These regions are defined by the following annealing temperature ranges and associated ellipsometric changes properties:

27°C - 200°C. The Ψ parameter is constant at the six wavelengths used. Thus, no optical changes occur up to 200°C.

200°C – 400°C. A transition takes place at the upper end of this temperature range indicated by a sharp drop in Ψ. This is due to nano-structural changes in the Au/$AuAl_2$:AlN cermet. As mentioned, XRD analysis suggested that annealing of the solar absorber above 220°C causes diffusion of Al atoms from the substrate into the Au/$AuAl_2$:AlN cermet where the Al reacts with the remaining Au nanoparticles to form $AuAl_2$. This is in approximate agreement with previous studies which have found the formation of well crystallized $AuAl_2$ to occur after annealing at 250°C or greater [99, 100].

400°C – 510°C. This is another "stabilization region". A moderate change in the ellipsometric parameters occurs, indicating a completion of the reaction of Al with Au. At this point the Au of the cermet has been fully reacted to $AuAl_2$.

510°C – 530°C. Flattening of the Ψ - time curves is this zone's characteristic. At this stage the $AuAl_2$:AlN cermet has fully formed.

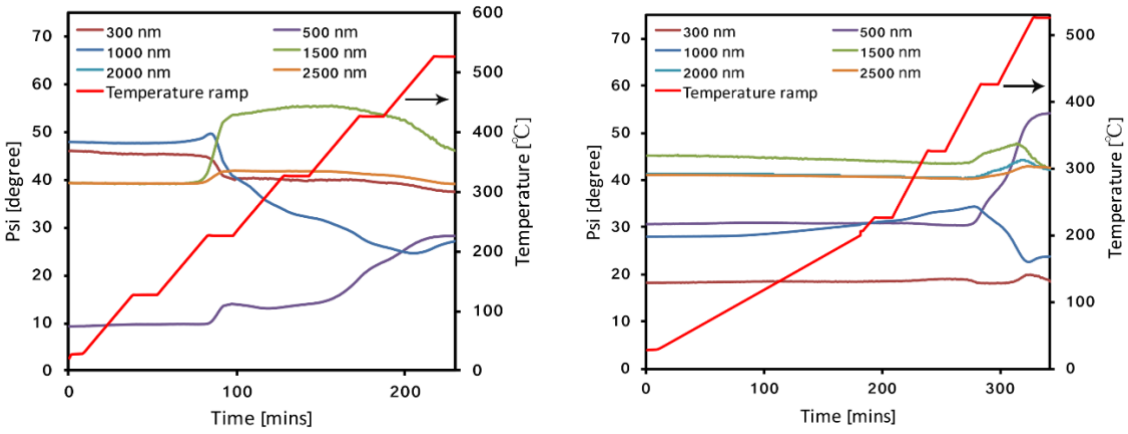

Figure 3.12 - Amplitude (Ψ) difference at six representative wavelengths as a function of time and temperature (red line) recorded by *in-situ* high temperature spectroscopic ellipsometry during ramp to 530°C, (a) Stack 1 and (b) Stack 2.

All the Au-$AuAl_2$:AlN spectrally selective stacks produced excellent solar absorptance, of 92% or higher. The high solar absorptance values of the as-deposited coatings were further boosted by intrinsic NIR absorptance in the AlN host due to its off-stoichiometric (Al-rich) composition. In addition, the presence of the AlN and SiO_2

antireflection coatings also added to absorptance by allowing more solar energy to enter the stack. Despite this commonality, the three stack designs differed quite significantly in their detailed behavior. This will now be described below.

Stack 1

Absorptance rose in the single Au-$AuAl_2$:AlN layer stack by 3% after annealing for 30 minutes at 500°C but was not further changed even after 7 days of annealing, Figure 3.13. The relatively low value of thermal emittance of 13% in the single layer cermet absorber after annealing is comparable with other studies [101]. This is still higher than that of traditional double cermet W-AlN stack after annealing at 500°C for 1 hour (ε = 3.7%) as shown in Zhang's work, where almost no change after heat treatment was observed [61]. However, it should be noted that the Au-$AuAl_2$:AlN coating having a single solar absorbing cermet layer shows improvement in solar absorptance after annealing and increased to 95%, which is higher by around 1%, compared to W-AlN stack. Also, according to high-temperature ellipsometry results, the optical properties of the stack_1 remain unchanged during and after annealing (Figure 3.14).

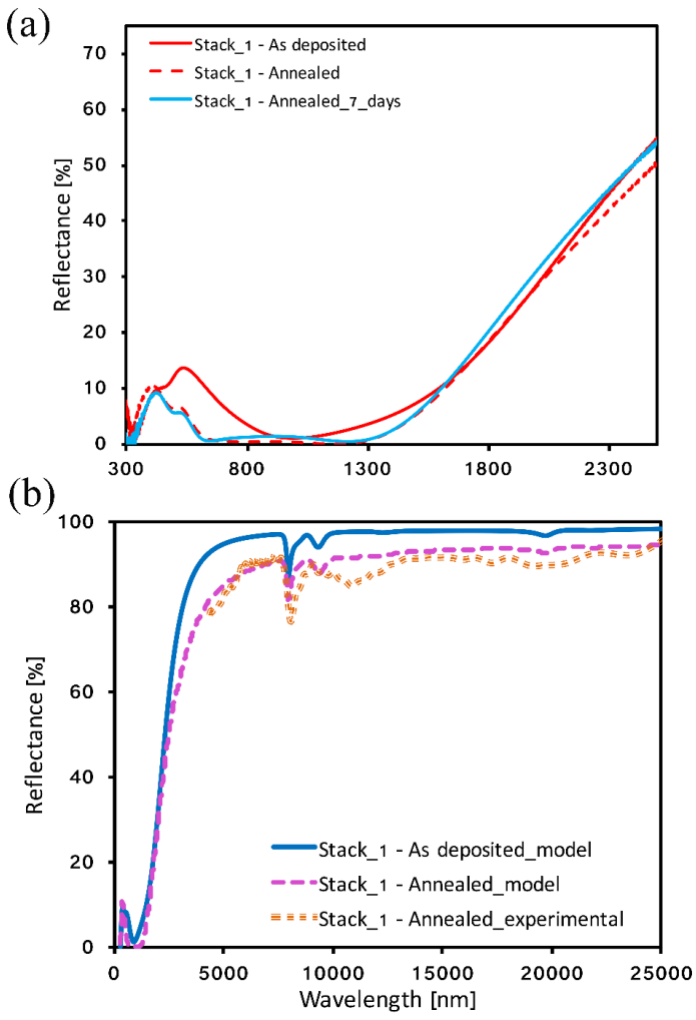

Figure 3.13 - Optical properties of Stack 1. a) Effect of short (30 minutes) and long (7 days) annealing at 500°C on the reflectance of Stack 1. b) Modelled spectral reflectance of Stack 1 before (solid line) and after (dashed line) annealing at 500°C for 30 minutes and experimental spectral reflectance of Stack 1 after (dotted line) annealing at 500°C for 30 minutes. In this analysis the fitted optical properties have been used to extrapolate the performance out to 25 μm infrared radiation.

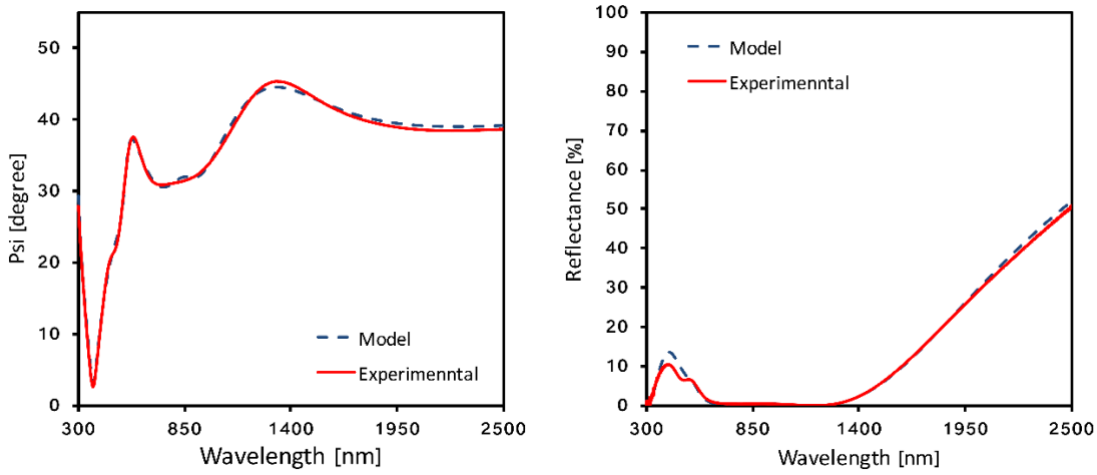

a) b)

Figure 3.14 - The results of parallel fitting of ellipsometric (a) and spectroscopic (b) data for the annealed Au-$AuAl_2$:AlN single cermet stack (compare to the as-deposited state in Figure 3.13).

The single Au-$AuAl_2$:AlN cermet structure plotted had the smallest changes in IR reflectance, which we attributed to less stress and less surface texturing at the Al/Au-$AuAl_2$:AlN interface after annealing than the other two designs due to simpler structure. The onset of the spectral transition from low R to high R barely changes and it is virtually complete by ~2 to 3.5 μm (Figure 3.13a).

To evaluate the hemispherical emittance at 500°C, room temperature (RT) ellipsometric results were compared to high temperature (HT) ellipsometric data at 500°C. A comparison of RT and HT ellipsometric parameters shows insignificant changes (Figure 3.15) enabling the approximation to be made that reflectance spectra

during and after annealing are equal. Thus, $\varepsilon_{500°C}$ was calculated using modelled reflectance results employing formula (1.15) to calculate emittance at 500°C.

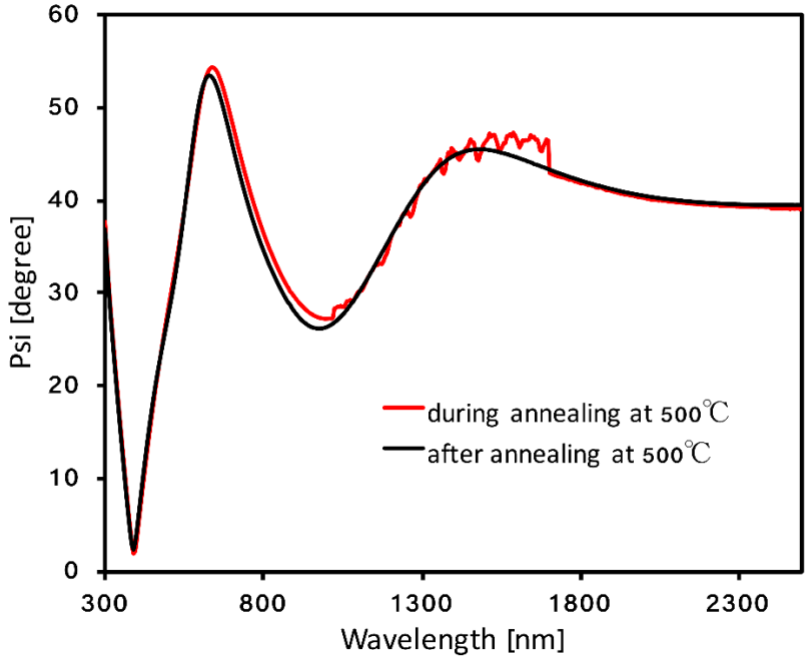

Figure 3.15 - Ellipsometric parameters of a Au-$AuAl_2$:AlN single cermet solar absorbing coating during and after annealing

Stack 2

A superior normal solar absorptance of 97% occurred in Stack 2 (as-deposited) due to its double solar absorbing layer structure. According to Du, photothermal conversion in double cermet multilayers is governed by two principle mechanisms: the first is by intrinsic absorption in the cermet layer lying above the reflective substrate, the second is enhancement of absorption by the optical interference occurring between the two layers [102]. Unfortunately, there was some degradation in performance of Stack 2 after annealing, Figure 3.16, with a decrease in reflectance due to the development of a high degree of texturing at the Al interface, and a decrease in absorptance due possibly to a disruption of the interference between the two cermet layers. This was presumably caused by Kirkendall voiding, Figure 3.6.

Stack 3

Stack 3, which had the gold reflective substrate, followed the same double cermet design as Stack 2, and exhibited solar absorptance of 95% at normal incidence in the as-deposited form, and up to 92% after annealing at 500°C. The Au film reflector enables

the lowest emittance initially of 2.3% relative to that from Al of 3.5%. However, after annealing at 500°C for 30 minutes, its IR emittance rose to 26%, Figure 3.16. This is too large for use in solar absorptive coatings. SEM examination revealed that the problem was caused by delamination of the Au reflective layer. Due to partial delamination of the coating on the Au back reflector after heat treatment (Stack 3), additional ellipsometric measurements on a selected and un-delaminated area were conducted to get more accurate results.

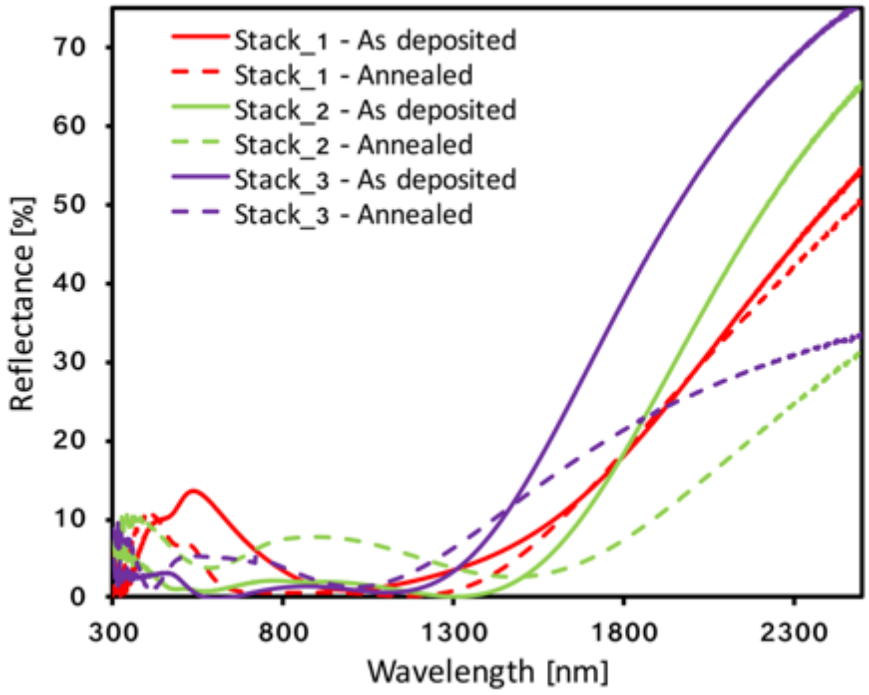

Figure 3.16 - Reflectance of multilayer Au-$AuAl_2$:AlN solar absorber Stacks 2 and 3 before (solid line) and after (dashed line) annealing at 500°C for 30 minutes. Stack 3 partially delaminated during annealing; the 'selected area' curve is for an intact region of the coating.

It is obvious from Equation (1.13) that as S_{total} - hence the number of Suns - rises for a pre-set $T_{absorber}$ then η also rises and approaches its maximum possible value of α_s. For parabolic trough collectors with operating conditions as in Gharbi's work with an incident flux of 80 Suns and approximate absorber temperature of 500°C, the weighting factor is 0.25 which reduces η by about $0.25\varepsilon = 0.03$ for the Stack 1, where ε=13% is measured spectral emittance of the annealed at 500°C Stack 1 (Table 3) [103]. It follows that, at

these conditions, an increase in solar absorptance contributes more to an enhancement of the solar collector operation than an equal decrease in a thermal emittance [104]. As a general rule for high operating temperatures, the highest possible absorptance and its thermal stability is the priority material issue. While it is ideal to also maintain the low as-prepared emittances shown in Table 3, at high T a small rise in emittance is tolerable as long as α_s is maintained. The high impact of $T^4_{absorber}$ does not change. Our values of α_s and ε for the annealed stack in equation (1.13) yield a solar absorber collection efficiency of ~91%. If it was assumed that the α_s and ε of the single cermet stack were unchanged after annealing, then the heat collection efficiency of the absorber is still 91%. This demonstrates that a small rise in α_s after annealing is of major benefit even if ε rises by 1%. However, the rise in ε from 3.5% to 21.2% in the double cermet layer on Al along with a 3% fall in α_s, leads to a larger drop in efficiency which goes from an initial 94% to ~88%. This is still good though. A minor tuning of the double layer design to give a ε rise limited to 1% and a stable α_s could make this stack superior at 500°C or above.

3.7 Conclusions

In this work, a novel approach was taken to demonstrate the possibility of the Au-based SSCs to be exploited in high temperature CSP applications. In the past, successful commercialization of gold-containing coatings was not possible due to thermally activated nanoparticle aggregation. This process is already quite rapid at temperatures as low as 250°C. Hence, preservation of both plasmon resonance response and raising thermal tolerance is a challenging task. This issue was solved here by a heat-treatment of the Au cermet-based spectrally selective stack to force the gold nanoparticles within the cermet to react with metallic Al from the underlying reflective layer (or, in principle, with excess Al co-deposited into the AlN matrix) to form nanoparticles of the less labile $AuAl_2$ intermetallic compound.

Two types of stacks having different designs were examined for this purpose: 1) a multilayer coating employing two layers of Au/$AuAl_2$:AlN cermet separated by a thin layer of AlN and 2) a single Au/$AuAl_2$:AlN cermet solar absorbing coating with both stacks having two antireflective coating (AlN, SiO_2) on top to decrease impedance mismatch. Double cermet stack yielded a spectrally selective solar absorbing coating with

a superior value of near normal incidence solar absorptance of 97% due to optimized stack design versus 92% for a single cermet stack. The influence of the stack designs and the formation of $AuAl_2$ nanoparticles inside the AlN dielectric matrix on final thermal efficiencies was examined. It turns out that, in case of a single cermet stack, a boosted solar absorptance can be achieved after a heat treatment resulting in an increase of light absorptance in the solar range by 3% (95% is the final value). This was possible due to substantial supply of the Al atoms from the reflective layer reacting with the encapsulated Au particles in the AlN host and forming $AuAl_2$ nanoparticles. As a result of this reaction during the heat treatment process, voiding of the dielectric host occurred due probably to the Kirkendall effect. Despite a rise in emittance from 4.7% to 13% after heat treatment, the thermal efficiency of an evacuated solar collector using a single cermet coating of the $Au/AuAl_2$:AlN type was predicted to remain at around 90%. This coating was stable for at least 7 days at temperature, with no significant change in optical response. A double cermet design showed reasonable thermal stability with minor reduction in solar absorptance by 3%. This happened due to the lack of the Al supply in the top cermet layer compared to the bottom cermet layer being closer to the Al reflector. I predict that the optical response of this type of stack could be also preserved after the heat treatment in future if a very thin layer of Al is deposited below the top cermet layer, thus, providing, the Al supply to form $AuAl_2$ nanoparticles in the top cermet layer.

In summary, the study described in this chapter show that Au in nanoparticle form has excellent potential for use in high temperature solar energy applications if three conditions are met: first the Au must be alloyed with another metal such that a less labile intermetallic compound is formed, second this compound must still possess a suitable low loss dielectric function and finally, the particles must be embedded in a stable and refractory dielectric matrix such as AlN. In addition, some NIR absorption in the host matrix is beneficial as found in the AlN layers used in this study. Crystalline and exactly stoichiometric AlN does not have this latter broad band absorption feature but it can be engineered by deposition of Al-rich AlN.

Chapter 4

$Ti_xAl_{1-x}N$-based stack for high temperature concentrated solar thermal applications

4.1 Introduction

In today's material science, nitrides take a special place due to their ability to achieve a wide spectrum of properties. Nitrides in combination with different elements of the periodic table may create structures with metallic, semiconductor or insulator-like behaviour. Metal nitride compounds represent a special interest as many of them have high chemical resistance, high thermal stability, wear resistance and are very hard [37, 47]. Such a broad variety of nitride phases with a wide range of structures and corresponding chemical and physical properties enables them to be successfully applied as optical and protective coatings, ultraviolet radiation detectors, diffusion barriers, solar cells, heat mirrors and plasmonic materials.

Different metal-nitride tandems composed of Si_3N_4, AlN, TiAlON, TiCN, CrAlON, TiN and TiAlN thin layers have been designed to achieve high thermal stability and desired spectral selectivity of film stacks for enhanced solar thermal conversion [40, 105-109]. Among these, TiN is very widely used due to structure simplicity (cubic NaCl), broad regions of homogeneity, efficient diffusion barrier properties, optical properties resembling gold, and a relatively easy deposition process (e.g. arc vapour deposition or magnetron sputtering). However, to overcome rapid oxidation of the TiN at 500°C and to push the boundaries of thermal tolerance, foreign elements such as Sc, Al, Cr, Nb have been introduced into the binary compound, with Al being the most popular addition and forming the single cubic $Ti_xAl_{1-x}N$ phase with randomly distributed Ti and Al atoms within the metal sub-lattice [110-112]. This was successfully demonstrated in Munz's work [113], where $Ti_{0.5}Al_{0.5}N$ showed thermal tolerance up to 700°C in hot air, which was attributed to the formation of a protective aluminium oxide layer. Further heat treatment lead to a rapid oxidation of the $Ti_{0.5}Al_{0.5}N$ film. However, while extension of oxidation limits of the TiN was successfully achieved by introduction of Al, another problem, spinoidal decomposition at ~800°C, set a new maximum operating temperature.

All $Ti_xAl_{1-x}N$ films produced to date show a tendency to decompose when heated. In Höglund's work, a thermally annealed at 1000°C $Ti_{0.51}Al_{0.49}N$ thin film in a vacuum ambient (5×10^{-4} Pa) showed oxidation and loss of Al into a vacuum chamber followed by spinodal decomposition into c-AlN and TiN-rich domains starting at 800°C with a clear phase separation at 1000°C [110]. A series of other studies support a phase separation of the $Ti_xAl_{1-x}N$ into coherent c-AlN and c- TiN phases in the 800°C -1000°C temperature range, where the main mechanism of phase separation is agreed to be the amount of energy supplied during annealing which causes the atomic diffusion that drives the spinodal decomposition [114-116]. On one hand, spinodal decomposition is known to have a positive effect in $Ti_xAl_{1-x}N$ systems for industrial applications, as a result of self-hardening of the face-centered cubic $Ti_xAl_{1-x}N$. However, any structural modification usually involves alteration in optical response of the material, which should be prevented if used in high temperature solar thermal applications. Hence, there is a need to develop a material with suitable and stable optical behaviour and simultaneous extremely high thermal tolerance. From this perspective, TiAlN is a very suitable candidate as it has already been proven to withstand high temperatures when used in efficient solar absorber coatings. Therefore, the goal of the current research was to explore the thermal stability of Al,Ti,N-based stacks up to 900°C and to see how a possible decomposition of the TiAlN layers may affect the optical response of the multilayer SSC.

Introduction of a corrosive environment worsens the problem. For example, Cunha showed decomposition of the $Ti_xAl_{1-x}N$ into AlN, Al_2O_3, TiO_2 and possible TiAlON in a very corrosive environment (H_2O-HCl) during annealing at 350°C due to loss of nitrogen and consequential oxidation of metallic elements [117].

4.2 Experimental details

A $Ti_xAl_{1-x}N$ -based spectrally-selective solar absorbing coating was deposited on a polished stainless steel (SS) substrate using a DC magnetron sputtering system. Prior to the deposition process, the vacuum chamber was evacuated to a base pressure of 2.8×10^{-6} Torr. The SS substrate was mechanically polished and then ultrasonically cleaned in an acetone and ethanol bath for 80 minutes in total. High purity targets Ti (99.99%), Al (99.9%), Pt (99.99%) and SiO_2 (99.99%) with a diameter of 50 mm were used for sputtering. The targets were cleaned for 1 minute in Ar-plasma prior to the deposition. For the TiAlN and AlN layers co-sputtering of the Ti and Al target was performed with

simultaneous introduction of N_2. Ar and N_2 were introduced to the chamber at the pressure of 7×10^{-4} Torr and 1.1×10^{-3} Torr, respectively, for deposition of TiAlN layer on a heated substrate using a heating module set to 180 W for 30 mins. The AlN layer was deposited on a heated substrate with Ar and N_2 pressure being at 1.5×10^{-3} Torr and 2.4×10^{-3} Torr. An RF power supply was used at 50 W for deposition of the AR SiO_2 layer. The thickness of the thin films was controlled using a quartz crystal monitor installed inside the deposition chamber. The Pt IR reflector was selected due to high melting point and temperature stability and was deposited underneath the AlN diffusion barrier layer. The Pt metal film was deposited at Ar pressure of 1.3 mTorr, correspondingly, with the applied target current of 0.15 A. Individual single layers for the test control were deposited on a Si substrate as per Figure 4.1 in the following order: Pt, AlN, TiAlN, AlN, SiO_2.

To test the potential of the cermet-based SSCs for high temperature CSP applications, the multilayer stack was first exposed to high temperature annealing for 24 hours at 600°C in a vacuum tube furnace pumped down to 10^{-5} Torr and then to 24 hour annealing at 700°C, 750°C, 800°C, 2 hour annealing at 850°C and 3 hour annealing at 900°C, using the Denton thermal evaporation chamber pumped down to 10^{-5} Torr. The evolution of phases of the heat treated samples was observed using X-ray diffractometry employing a Bruker D8 Discover with LYNXEYE XE detector, Cu kα radiation (λ=1.54056 Å) operating at 40 kV and 40 mA and angle of incidence set at 8°.

The spectral reflectance was obtained using an Agilent Cary 7000 Universal Measurement Spectrophotometer (UMS) covering the 300-2500 nm wavelength range (angle of incidence 8°). The emittance of solar absorbing coatings for solar thermal applications was measured using a custom built emissometer heated to 82°C. The broadband thermopile sensor used detects thermal radiation over the 2.5 - 50 μm spectral range. The calibration of the instrument was conducted using an Al reference sample. Spectroscopic ellipsometry using a J.A. Woollam Co., Variable Angle Spectroscopic Ellipsometer (VASE) was used for determination of the optical constants. The ellipsometric parameters were measured in the 300 - 3000 nm wavelength range in 5 nm steps at angles of 60°, 70° and 75°.

For a comprehensive analysis of these spectrally selective solar absorbers, a theoretical model of the stack was built using WVASE software (J.A. Woollam Co.). The generated results were fitted to the experimentally measured ellipsometric parameters and measured

reflectance spectra, and then were displayed in terms of the final reflectance spectra for the best fit multi-layer model of the coating.

4.3 Design and structure

The theoretical design of the $Ti_xAl_{1-x}N$-based solar absorber deposited on a polished stainless steel (SS) substrate is shown in Figure 4.1a. The Pt was chosen as the IR reflector due to high reflectance obtained for the deposited Pt thin film, compared to other refractory metals tested such as Ta, W, V or Ni. Al or Ag also showed high values of the IR reflectance, but were not considered for this study due to their lower melting points.

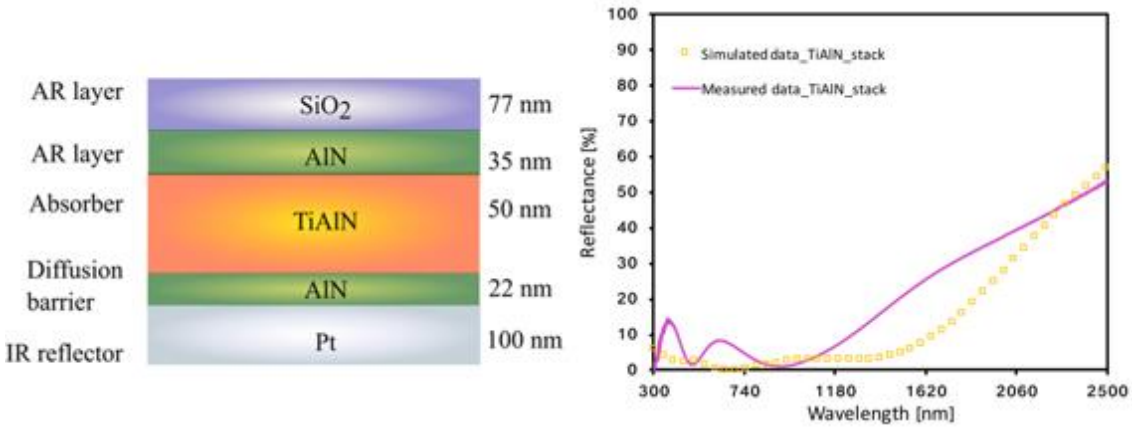

a) b)

Figure 4.1 - a) Design and b) comparison of the theoretical and measured optical response of the TiAlN-based stack using Pt as a back reflector

22 nm AlN was deposited on top of the Pt reflector in order to prevent any possible thermal diffusion from the Pt back reflector or the SS substrate. The main absorbing layer was comprised of the $Ti_xAl_{1-x}N$ thin film, the Al/Ti ratio of which was carefully selected in order to achieve a maximum of the solar absorptance for the whole multilayer stack. Table 4.1 shows how the selected current applied to the Ti and Al targets affected the overall absorptance of the stack. Each $Ti_xAl_{1-x}N$ thin film was ellipsometrically measured and the determined optical constants were used to model the SSC and determine the theoretical solar absorptance. The layer with optimal deposition parameters resulted from

an Al/Ti ratio that led to 95.6% solar absorptance of the SSC and was thus selected for the deposition within the stack. Two AR coatings, AlN and SiO_2, were deposited on top of the stack to reduce front reflection, along with the top AlN layer comprising an interference sandwich with the bottom AlN layer. The theoretical solar absorptance was calculated based on the ellipsometric measurement and retrieved optical constants for each individual layer. The resultant reflectance prediction is displayed in Figure 4.1b with a designed cut-off at 2000 nm. The theoretical model shows a broad highly absorptive region between 300 nm and 2000 nm. The experimentally obtained $Ti_xAl_{1-x}N$ based SSC shows a more reflective response between 1200 nm and 2000 nm indicating a higher percentage of the metallic fraction in the main absorbing layer. Several factors may have contributed to this: 1) randomized distribution of the metallic Ti and Al species driven by the kinetics of the sputtering conditions 2) higher level of vacuum (2.6×10^{-6} Torr) achieved for the deposition of the stack compared to 6.2×10^{-6} Torr obtained for the individual deposition of the $Ti_xAl_{1-x}N$ thin film, which leads to higher level of directionality of the sputtering metallic species and, as was shown in Table 4.1, may result in a reduction of solar absorptance by nearly 3% and higher reflectivity. A similar result will be demonstrated for the sputtering of back reflectors, which will be discussed in more detail in Chapter 6.

Table 4.1 – The effect of Ti and Al target currents on the absorptance of the $Ti_xAl_{1-x}N$ based stack

Solar absorptance, %	**87.8**	**91.2**	**91.6**	**92.9**	**93.3**	**95.6**
Ti current, A	0.4	0.3	0.4	0.38	0.4	0.38
Al current, A	0.25	0.12	0.12	0.27	0.3	0.26

Figure 4.2 shows the structural modifications of the $Ti_xAl_{1-x}N$-based SSC recorded by the XRD measurements after each heat treatment up to 900ºC. The XRD data indicates the presence of the several crystalline phases in the multilayer stack mainly related to the $Ti_xAl_{1-x}N$ solar absorbing layer, as no phases attributed to the crystalline AlN, SiO_2 or Pt were detected, reflecting the amorphous or poorly crystalline nature of these layers. The as-deposited stack shows that co-sputtering of the Ti and the Al in presence of nitrogen atmosphere results in the formation of the cubic $Ti_{0.55}Al_{0.45}N$ phase. The XRD also

detected some Ti oxides, which might be due to the presence of the residual oxygen in the vacuum chamber. The annealing of the stack at 600ºC results in the upward thermal diffusion of the Fe present in the SS substrate into the Pt IR reflecting layer, resulting in the formation of the Fe_3Pt phase. Furthermore, it leads to the decomposition of the phases assigned to the TiO_x and $Ti_{0.55}Al_{0.45}N$. The heat treatment of the $Ti_xAl_{1-x}N$-based SSC at 800ºC and up to 900ºC shows a further thermally-induced upward migration of the Fe species from the SS and formation of the Fe_3Pt phase. The $Ti_{1-x}Al_xN$ is still present however, although its peaks are much smaller than those of Fe_3Pt. The effect this has on a spectral selectivity and the optical response of the stack will be discussed later. Further heat treatment at 800ºC and above causes the Pt in the Fe_3Pt to diffuse down into the substrate so that only the peaks for the austenite phase (F m -3 m, a=3.628 Å) of the substrate are visible. From this it can be concluded that the 22nm AlN diffusion barrier was not effective above 600°C. In addition, a thicker AlN diffusion barrier should be deposited in future between the SS substrate and the Pt back reflector to avoid the formation of Fe_3Pt at the earlier stages of annealing,

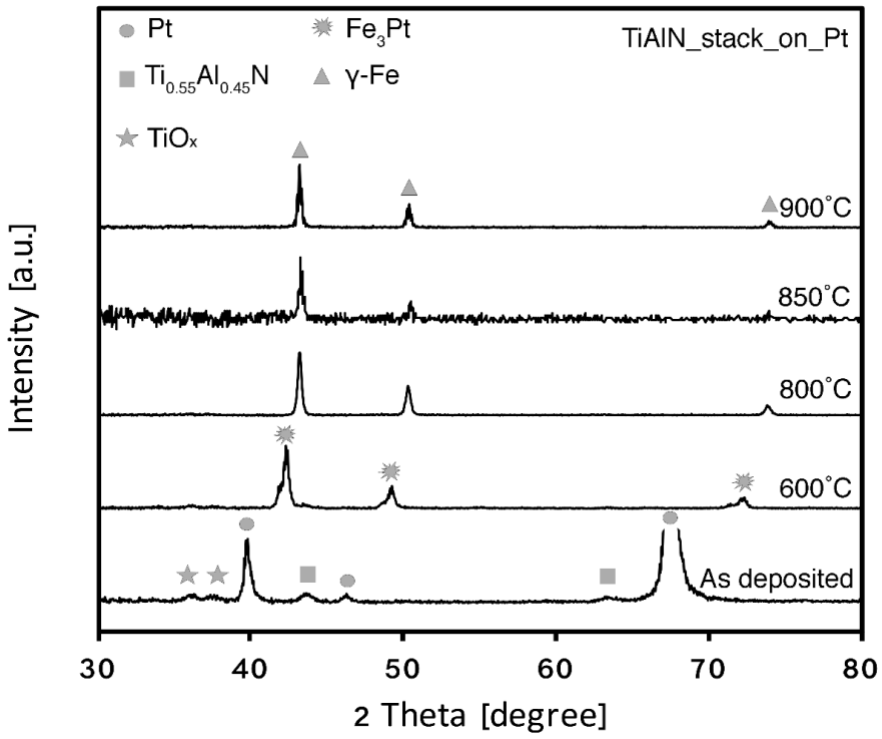

Figure 4.2 – The XRD patterns of the as-deposited and annealed $Ti_xAl_{1-x}N$ SSC on Pt

4.4 Optical characterization of the as-deposited $Ti_xAl_{1-x}N$ -based solar absorber

The designed $Ti_xAl_{1-x}N$ based solar absorber demonstrates a high level of spectral selectivity with minimized reflectance up to 2000 nm, Figure 4.3, enabling achievement of 92% of solar absorptance. The 2000 nm cut-off was deliberately selected for the application of the absorber at 630ºC. This is due to the position of the BB spectra, shifting towards shorter wavelengths when the sample is heated at higher temperatures, as shown in Figure 4.3 and discussed in the Introduction chapter. There is also appearance of the interference peaks at

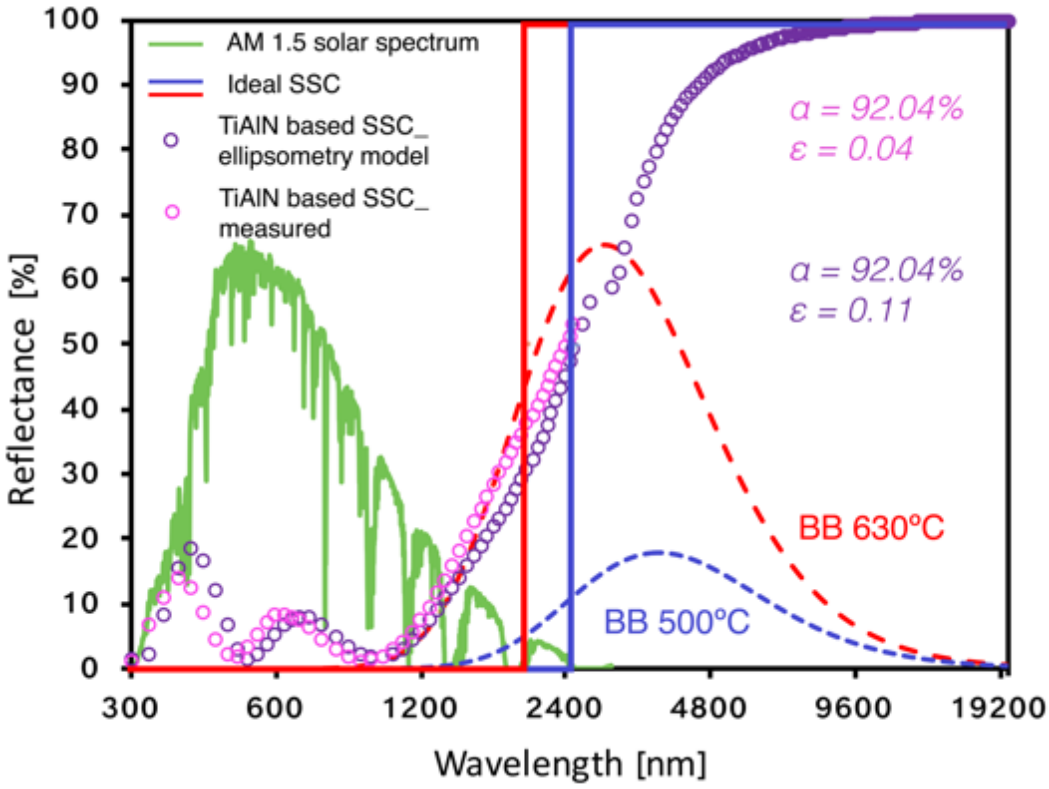

Figure 4.3 – Measured and modelled (ellipsomeric fit to psi and delta of the stack) spectral selectivity of the $Ti_xAl_{1-x}N$ based SSC reflectance wise. The solar and blackbody spectrum are for illustration purposes

around 350 nm and 600 nm due to a multilayer structure and a reflection/refraction of the electromagnetic wave at the interfaces. The modelled reflectance curve was extracted from WVASE software from the experimental fit of the measured ellipsometric parameters of the whole stack with extrapolation starting from 3000nm and up to

20000nm. The SSC shows steep reflectance ramp-up between 2000 nm and 4000 nm and nearly 100% of reflectance in the far IR region, confirmed by the measured low thermal emittance, $\varepsilon_{82°C}$=0.04. The calculated thermal emittance using model prediction shows a slightly higher value of ε=0.11, which is attributed to the measurement of the individual Pt IR reflector up to 3000 nm giving known optical constants of the layer up to 3000 nm point. This is demonstrated and predicted in the modelled reflectance curve at 3000 nm showing a minor reduction in the reflectance ramp.

Figure 4.4 shows an initial measured spectral response of the individual $Ti_xAl_{1-x}N$ layer on the Si substrate, followed up by the addition of the other layers. The solar absorptance of the semiconducting $Ti_xAl_{1-x}N$ layer is quite high, at 75.1%. Further enhancement in solar absorptance was achieved by the deposition of two AR layers AlN and SiO_2, where the final SiO_2 layer contributed to a reduction in reflectance in the vis-near-IR range by 3%.

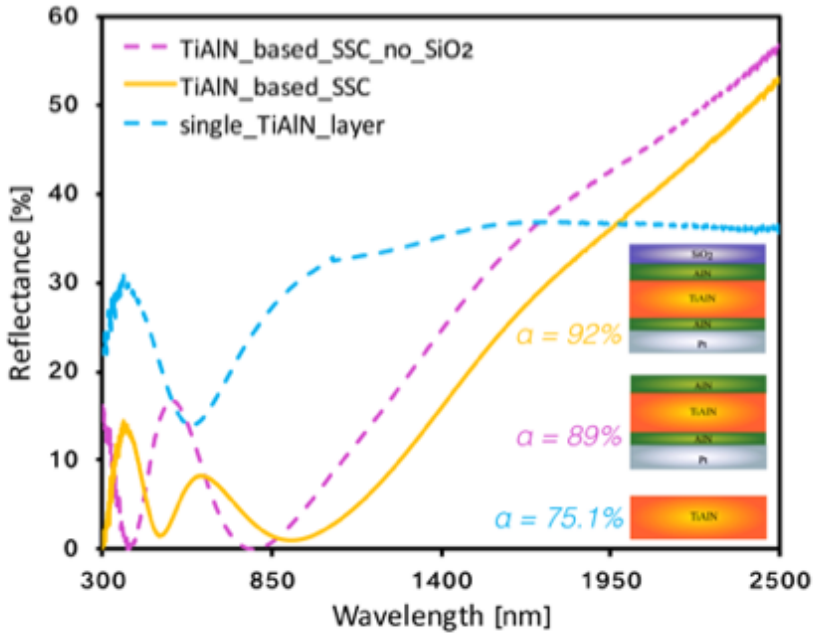

Figure 4.4 – Measured reflectance of the individual $Ti_xAl_{1-x}N$ layer on Si substrate, $Ti_xAl_{1-x}N$ based SSC without SiO_2 AR layer and final $Ti_xAl_{1-x}N$ stack on SS substrate.

As demonstrated in Gunther's work, for single tracking parabolic trough power plants, the solar absorptance of the spectrally selective solar absorber is important up to 32º due to the geometry of the parabolic trough mirrors and their relative position to the absorbing pipe [118]. Figure 4.5 demonstrates nearly unchanged solar absorptance up to 30º, with solar absorptance above 90% up to 50º, after which a steady reduction is

observed with the final drop to 60% at the incident angle of 80º which is attributed to both Lambert's cosine law in equation (2), and reduced intensity at higher incidence angles of the solar radiation as followed from the Fresnel equations.

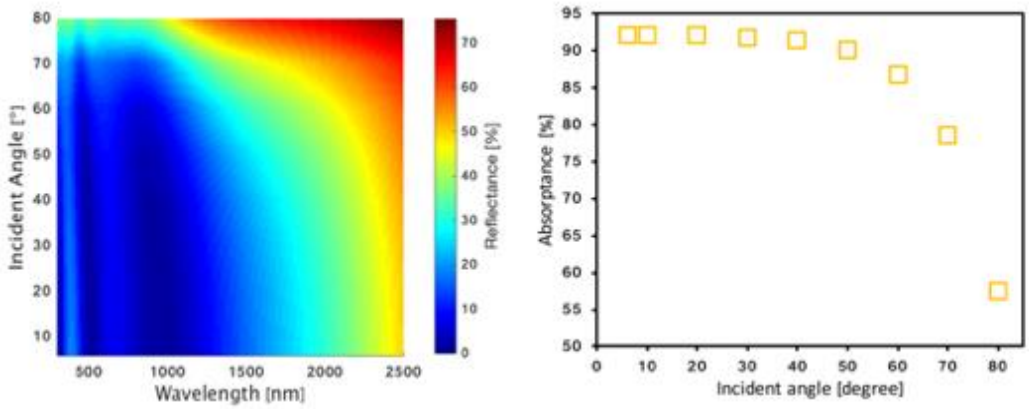

a) b)

Figure 4.5 – a) Modelled angular dependence of the reflectance and b) calculated angular solar absorptance of the $Ti_xAl_{1-x}N$ based SSC

4.5 The temperature-dependent optical characterization of the $Ti_xAl_{1-x}N$ -based solar absorber

Figure 4.6 demonstrates the ellipsometric fit to the measured psi parameters at different annealing temperatures up to 900ºC. These measurements were *ex situ* and were performed at room temperature. The high accuracy of fitting parameters was achieved mainly due to an adjustment of the oscillator parameters for the main $Ti_xAl_{1-x}N$ absorbing layer and Pt IR reflector, as shown before and after reaction with diffused species from the SS Fe at the higher annealing temperatures.

Overall, it is seen that the multilayer solar-absorbing stack undergoes the most noticeable change in optical behaviour after annealing at 800ºC. Up until that temperature the optical response of the multilayer stack remains almost the same, as observed in the fixed position of the psi peaks, their widths and intensity. The first annealing at 600ºC and further at 700ºC shows that the amplitude of the second hump of the measured psi parameter has slightly increased compared to the as-deposited conditions, and taking into account the XRD results, identifies some structural modifications of the stack but with almost unchanged optical response, which is in a good agreement with the measured temperature dynamic reflectance spectra (to be shown later). The other more noticeable change occurs after annealing for 24 hrs at 800ºC, where a shift of the psi spectra occurs

towards shorter wavelengths. This type of optical behaviour is nevertheless preserved upon the final annealing at 900ºC. At this stage, it can be concluded that the main pattern of the spectral behaviour of the stack is preserved up to 900ºC thermal treatment, with some minor changes.

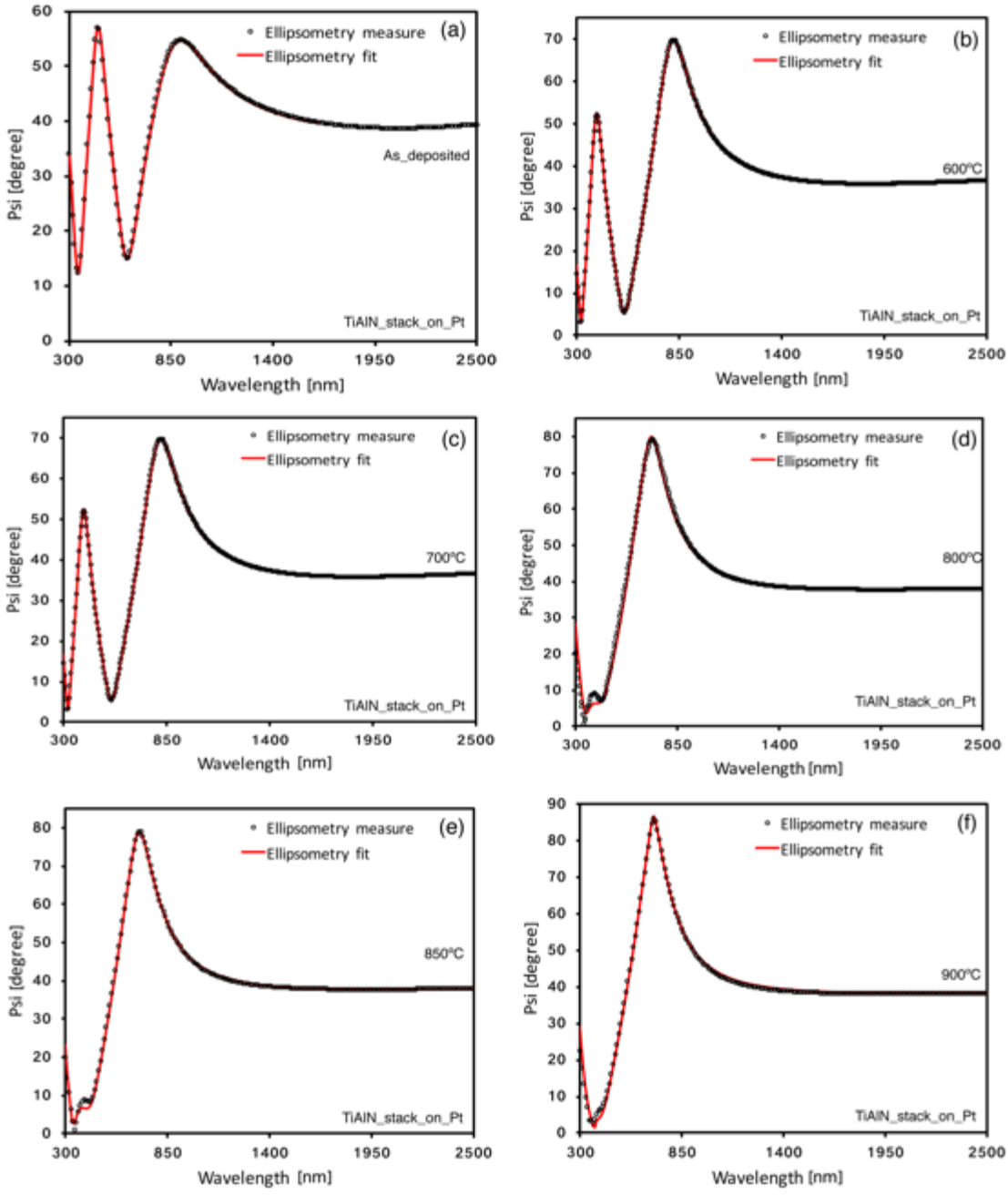

Figure 4.6 – Measured ellipsometric parameter psi and the fit after each stage of annealing in vacuum for 24 hrs (600 ºC -850ºC), 2hrs (850 ºC) and 3 hrs (900ºC) of $Ti_xAl_{1-x}N$ based stack

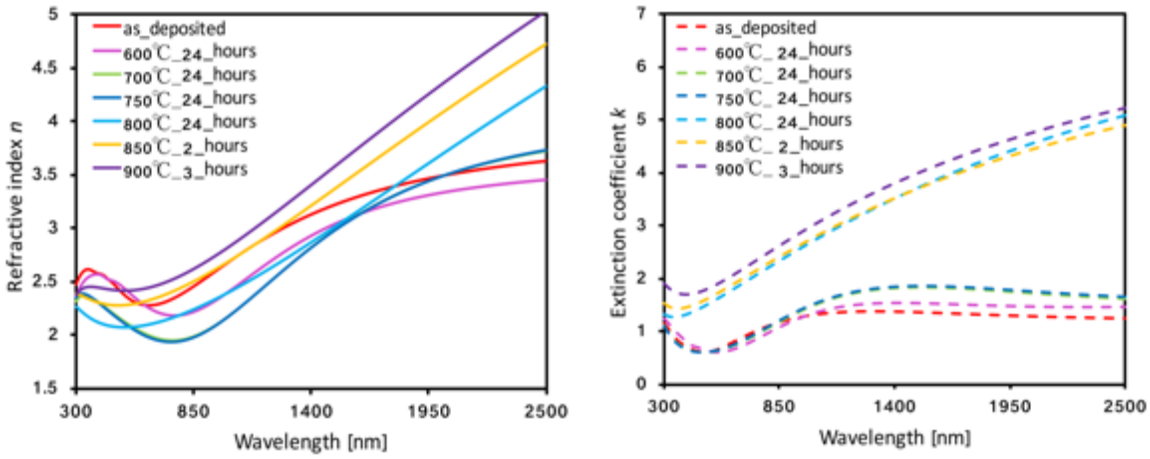

a) b)

Figure 4.6 – The evolution of the optical constants a) *n* and b) *k* of the individual $Ti_xAl_{1-x}N$ layer after each stage of heat treatment of the whole stack These plots were derived by fitting the measured ellipsometric parameters as shown in Figure 4.5

The extracted *n, k* optical constants of the $Ti_xAl_{1-x}N$ absorbing layer in Figure 4.6 up to 750° C shows semiconducting or semi-metal behaviour as the extinction coefficient *k* lies between 0.5 and 1.5 throughout the whole wavelength range, with its initial increase starting at around 500 nm and a downward trend after 1500 nm. The refractive index *n* also shows a transitional behaviour between dielectric and metallic response, with a dip in the visible range and a further rise up to 3.8 at the end of the wavelength spectrum range. This type of trend is observed for both optical constants after annealing at 750ºC in vacuum for 24 hrs for each cycle. The heat treatment at 800ºC for 24 hrs shows that $Ti_xAl_{1-x}N$ absorbing layer becomes optically denser and reveals a higher degree of metallic behaviour (because *k* shows an upward trend up to 2500 nm after a dip at 400 nm).

Figure 4.7 shows the reflectance spectrum of the $Ti_xAl_{1-x}N$ solar absorber designed to operate at 630ºC as would be the case for a photo-thermal conversion in an advanced parabolic trough solar power plant. The additional annealing up to 900ºC was conducted in order to test the potential of the stack for other high temperature solar thermal applications such as the recently emerged interest in STPV. As demonstrated in Jurczak's work, the starting temperature for the exploitation of STPV using a SSC (if the $Ga_xIn_{1-x}As$ semiconductor PV cell is used with the bandgap of 0.4 eV) would be 730ºC resulting

in an efficiency of 15% [119]. With further increase in the bandgap and the source temperature, higher efficiencies can be achieved.

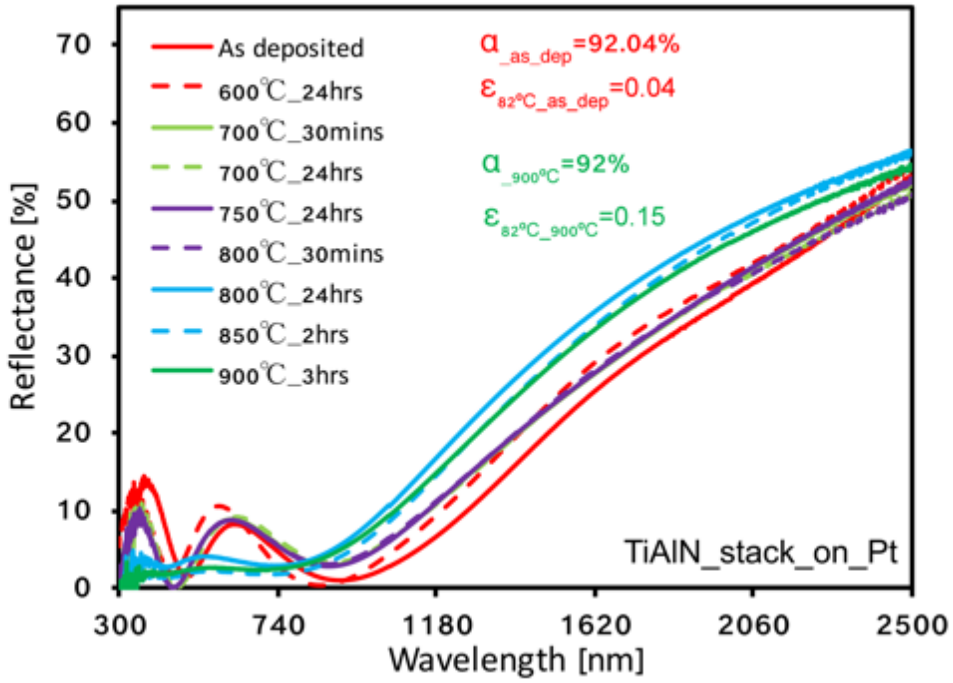

Figure 4.7 – The reflectance spectra of as-deposited and annealed $Ti_xAl_{1-x}N$ SSC up to 900ºC in vacuum

The annealing of the $Ti_xAl_{1-x}N$-based stack up to 750ºC for 24 hours does not significantly affect the spectrally-selective response of the multilayer solar absorber: the solar absorptance varies only between the initial 92% to 91.2%, Figure 4.8. This is also consistent with the ellipsometric measurements in Figure 4.6, shown by the absence of significant changes in the ellipsometric parameters up to 700ºC annealing. Interestingly, further short-term annealing of the stack at 800ºC for 30 minutes does not affect the reflectivity of the sample compared to the preceding annealing stage at 750ºC, however, annealing of the sample at 800ºC for 24 hours leads to more noticeable changes in the spectral response of the absorber. Firstly, there is disappearance of the two characteristic interference humps and flattening of the reflectance curve which is beneficial in this case and results in a more enhanced absorptance in the region, 300 nm – 750 nm, where the highest intensity of solar radiation is located. On the other hand, there is a slight rise in the reflectance curve starting at 1000 nm. This type of behaviour could be attributed to two possible phenomena: either recrystallization of the metallic back reflector or

structural modifications in the main absorbing layer. In this case, the first factor cannot take place due to an increase in measured emittance from its initial 0.04 to 0.15 after annealing at 900ºC. Hence, taking into account the extracted optical constants for the semiconducting $Ti_xAl_{1-x}N$ absorbing layer after final annealing, the increase in the reflectance spectra in the near-IR range is attributed to the more metallic-like response of this layer. Nevertheless, the calculated solar absorptance of the stack shows same strength of the solar energy harnessing, remaining at 92% with simultaneous preservation of its spectrally-selective response.

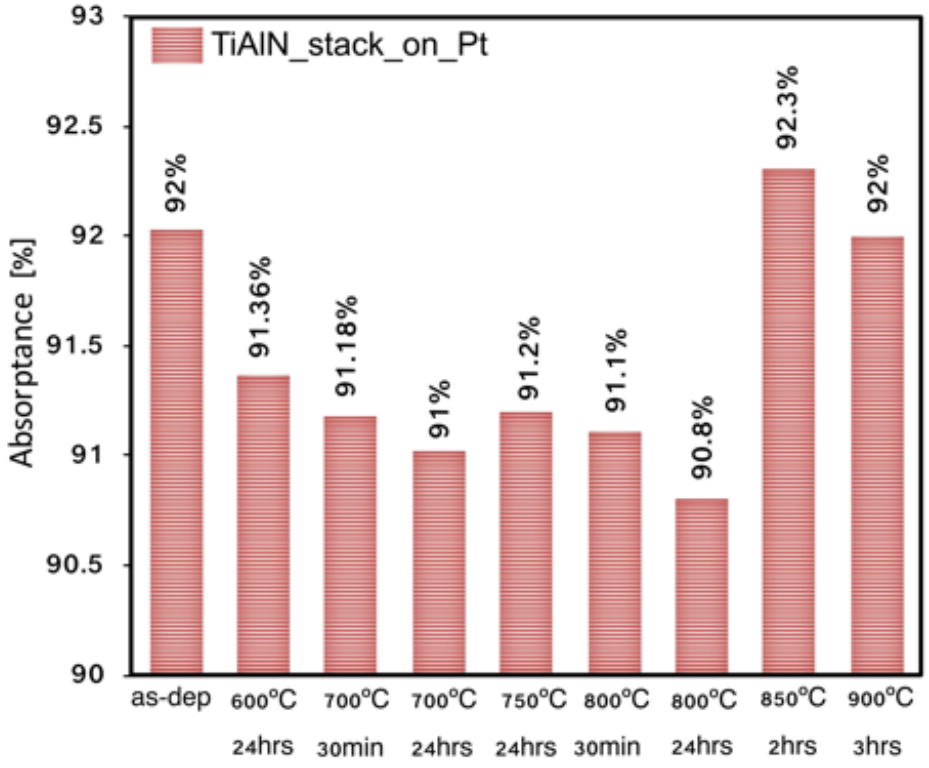

Figure 4.8 – Calculated integrated solar absorptance for as-deposited and annealed for 24 hours in the vacuum $Ti_xAl_{1-x}N$ SSC using Pt IR reflector on SS substrate

Considering the preceding results, the efficiency of the photo-thermal conversion at 630ºC was calculated with some analysis of the importance of the weighting and concentration factors as discussed in the Introduction chapter.

Figure 4.9 demonstrates the influence of the concentration factor on the conversion efficiency for the different solar absorbing surfaces operating at 630ºC. The parameters of the ideal SSC were assumed to be $\alpha_s = 100\%$ and $\varepsilon_s = 0.01$. At these parameters, the ideal surface would convert 96% of solar radiation already if C = 1 sun and would

reach 99.97% when C = 100. The photo-thermal conversion for the real selective absorbing surface, obtained in the current work, would not possible if C=3.5 suns.

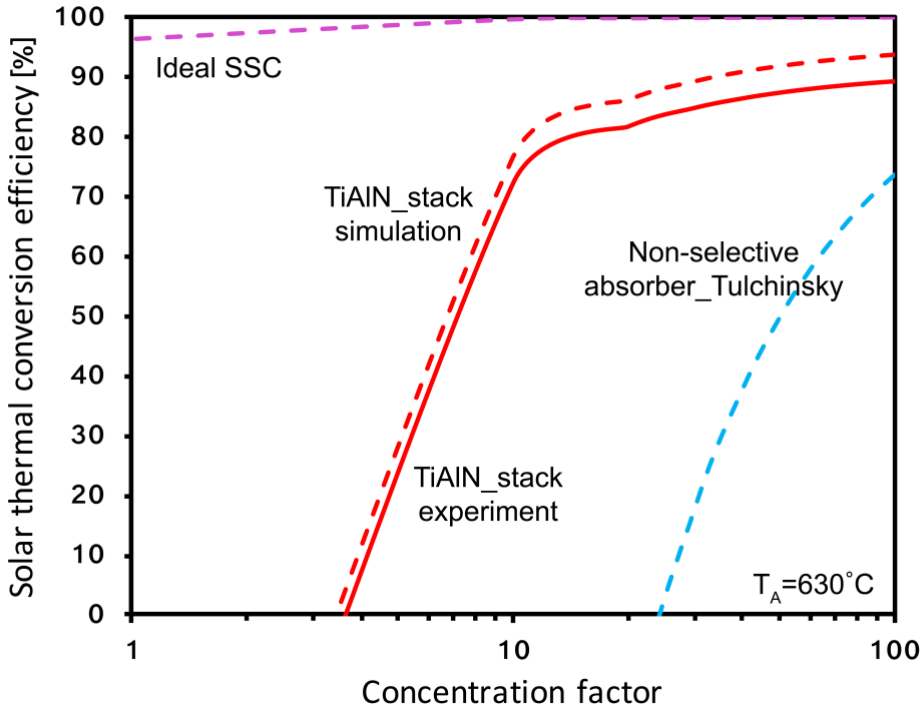

Figure 4.9 – The comparison of different absorbing surfaces contributing to the photo-thermal conversion efficiency as a function of concentration factor at operating temperature of 630ºC. The non-selective absorber described by Tulchinsky is included for comparison [13].

If both of them would be concentrated by a factor of 40, the modelled $Ti_xAl_{1-x}N$ SSC with expected solar absorptance of nearly 96% would convert solar radiation into useful heat with 92% efficiency and for the real deposited $Ti_xAl_{1-x}N$ SSC it would be 82.2% . For C = 100 suns the useful heat conversion is 93.7% and 89.5% for the modelled and real absorbing surface, respectively . Such a difference is attributed to the variance in the predicted and obtained solar absorptances for the $Ti_xAl_{1-x}N$ SSC, accounting for 96% compared to 91.36% when annealed at 600ºC. The thermal emittance was taken as 0.051 for the both modelled and deposited $Ti_xAl_{1-x}N$ SSCs to show the influence of rise in solar absorptance on efficiency of a photo-thermal conversion (in order to conduct a fair comparison, the single higher value of 0.051 was taken). This also indicates that, for higher concentration factors, an improvement in solar absorptance would be highly desirable as it enables a boost in harvesting of total solar energy by nearly 4%. Although,

the main accent has been on solar absorptance at higher concentration ratios with the emittance playing a secondary role, achieving low emittance is still important. The comparison shown here, for, the non-selective absorber obtained by Tulschinsky with α_s =97.4% and ε_{RT}=0.64, demonstrates the improvement from a lower emittance. The non-selective surface with a very high solar absorptance but also high thermal emission loss shows an ability to convert solar to heat energy at 30 suns with 5% efficiency compared to 75%, while for *C*=100 suns, the efficiency non-selective system would be 73.6%, which is nearly 17% lower than that obtained with our deposited $Ti_xAl_{1-x}N$ selective surface.

4.6 Conclusions

The research described in this chapter has demonstrated that a magnetron sputtered $Ti_xAl_{1-x}N$-based solar absorbing coating on an IR reflecting surface approach can show both high thermal stability and a useful spectral selective response. A coating with nearly 96% solar absorptance was obtained by fine tuning of the Ti/Al ratio. This material was then incorporated into a stack consisting of a Pt back reflector with an AlN layer as a diffusion barrier layer and, finally, two antireflective coatings on top, AlN and SiO_2. The experimentally obtained solar absorber showed high spectral selectivity ratio with its initial $\frac{\alpha_s}{\varepsilon_{82^oC}}$ =0.92/0.04. The lower value of the solar absorptance of 92% in the stack, compared to an expected 96%, was attributed to the higher level of vacuum achieved during the time taken to sputter the whole stack compared to the individual layer sputtering, the optical constants of which were used to model the whole stack. The reduced pressure resulted in a higher directionality of the ejected atoms from the metallic targets. The $Ti_xAl_{1-x}N$-based solar absorber proved to be stable after each cycle of annealing in vacuum for 24 hours, at 600ºC, 700ºC, 750ºC, 800ºC, and for 2 hours at 850ºC and 3 hours at 900ºC, preserving its high spectral selectivity $\frac{\alpha_s}{\varepsilon_{82^oC}} = 0.92/0.15$ with no change in solar absorptance. The $Ti_xAl_{1-x}N$ based solar absorber stack thus has potential for use in concentrated solar thermal applications at operating temperatures up to 900ºC.

Chapter 5

Ta:SiO_2 stack for high temperature concentrated solar thermal applications

5.1 Introduction

As has been discussed in Chapter 1, utilization of sunlight to extract other forms of energy can be achieved by well-established concentrated solar thermal technologies. An example is a parabolic trough power plant, where one of the key components is a spectrally selective solar absorbing coating that is able to withstand the current operating temperatures of around 490ºC-565ºC [120]. According to Figure 8, extending this temperature to 630ºC will result in the maximum power output of the CSP plant. Furthermore, shifting this temperature limit to even higher temperatures opens up possibilities for the emerging technology of solar thermophotovoltaics, where the concentrated light incident thermally onto a solar absorber creates photons used by the PV cell to induce electrical current. The latter application is a big challenge for materials scientists searching for a suitable spectrally selective solar absorber as even for a commonly used Ge PV cell with one of the lowest bandgaps, 0.67 eV, the generation of bandgap matching photons requires absorber/emitter operating temperatures above 1300ºC due to the position of the center of the peak in the blackbody irradiation spectrum. For this reason, many scientists construct and test STPV systems employing a InGaAsSb PV cell with a bandgap of 0.55 eV and, hence, requiring lower energy photons, that can be generated at 1007ºC to match the 0.55 eV bandgap [52, 121]. Furthermore, as shown in Bermel's work, raising operation temperature of the absorber/emitter structures in the STPV system from 730ºC to 930ºC results in an efficiency enhancement for their platinum-based structure by more than 8% [122].

While the primary goal of the current investigation was to design a SSC for advanced operation of parabolic trough solar power plants, the temperature limit of the fabricated coating was tested above 600°C in order to investigate its potential exploitation in STPV

devices.

As was shown in Chapter 1, the current designs enabling spectrally selective response are commonly represented by multilayers, cermets, semiconductor-metal tandems and their joint hybrid structures. Achieving both spectral selectivity and structural thermal stability in the 630ºC - 1000ºC range is a big challenge for these type of structures due to exploitation of different types of materials in one solar absorbing stack (metallic IR reflector, cermet layer including a metal and a dielectric, AR dielectric layer, etc) each having different thermal expansion coefficients, which cause generation of thermal stresses and possible degradation in long-term service. Hence, for the STPV applications, a new approach has been proposed for an SSC, namely a photonic crystal structure consisting usually of a single metallic material, where the difference in thermal expansion problem can be avoided, Figure 18f. However, in the present research, it will be demonstrated that a multilayer cermet SSC consisting of IR reflector, two graded cermet layers and a dielectric AR layer may not only survive very high temperatures but also preserve an enhanced spectrally selective response, with a high $\boldsymbol{\alpha/\varepsilon}$ (solar absorptance/thermal emittance) ratio.

Some of the recently developed SSC's for high temperature CSP applications consist of cermet stacks, a design also employed in the current research. For example, the Mo:SiO_2 based composite absorber introduced by Wang showed a high thermal tolerance up to 800ºC along with a 95% solar absorptance [60]. The WTi:Al_2O_3 cermet based solar absorber designed by Wang et al. was stable up to 600ºC with no significant change in the solar absorptance, which stayed at round 92.5%, along with the thermal emittance being below 11%. An $AlSiO_x$:W cermet based absorber introduced by Dias exhibited thermal stability up to 580ºC with unchanged solar absorptance, $\boldsymbol{\alpha \sim 95\%}$ and thermal emittance staying at around $\boldsymbol{12\%}$ ($\boldsymbol{\varepsilon_{400^\circ C}}$) after cyclic annealing [123].

In this work, a further improvement in spectrally selective response is demonstrated. A superior solar absorptance of nearly 98% was achieved for a double cermet Ta:SiO_2 stack along with a low thermal emittance. Furthermore, the stack shows excellent thermal stability up to 1000ºC, which, to our knowledge, has not been achieved yet for cermet based solar absorbers. This is an exceptional result, as both a nearly ideal spectral selectivity was gained with an extremely high thermal tolerance in vacuum.

5.2 Experimental details

Two types of spectrally selective solar absorbing coatings were deposited on Si substrates using a DC magnetron sputtering system without heating. The main difference between them was that they had different IR reflectors. Prior to the deposition process, the vacuum chamber was evacuated to a base pressure of 2.8×10^{-6} Torr. The Si substrates were ultrasonically cleaned in an acetone and ethanol bath for 80 minutes in total. High purity targets Ta (99.99%), Pt (99.99%) and SiO_2 (99.99%) with a diameter of 50 mm were used for sputtering. The targets were cleaned for 1 minute in Ar-plasma prior to the deposition. For the cermet layers co-sputtering of the Ta target and the SiO_2 target was performed. Ar was introduced to the chamber at the pressure of 1.4 mTorr for deposition of two cermet layers Ta:SiO_2 with high metal volume fraction (HMVF) and Ta:SiO_2 with low metal volume fraction (LMVF) and at 1.3 mTorr for deposition of antireflective (AR) SiO_2. The Ta filling factor in a cermet layer was controlled by varying the current applied separately to the targets at 0.04 A and 0.09 A, for the LMVF and HMVF, respectively. An RF power supply was used at 132 W for deposition of both cermet layers and an AR SiO_2 layer. The thickness of the thin films was controlled using a quartz crystal monitor installed inside the deposition chamber. An IR reflector of either Ta or Pt was deposited underneath the cermet. The Ta and Pt metal films were deposited at Ar pressure of 1.6 mTorr and 1.3 mTorr, correspondingly, with an applied target current of 0.15 A for both metals.

To test the potential of the cermet-based SSCs for high temperature CSP applications, the multilayer composites were first exposed to 600°C in a vacuum tube furnace pumped down to 10^{-5} Torr for 30 minutes and then to 1 hour at 700°C, 800°C, 900°C, 1000°C and 1100°C using a Denton thermal evaporation chamber pumped down to 10^{-5} Torr, where each anneal followed the previous one. The evolution of phases of the heat-treated samples was observed using X-ray diffractometry employing a Bruker D8 Discover with LYNXEYE XE detector, Cu kα radiation (λ=1.54056 Å) operating at 40 kV and 40 mA and angle of incidence set at 8°.

To identify the microstructural features of the coatings, images of cross-sections were taken with a ZEISS EVO scanning electron microscope at 20 kV.

The spectral reflectance was obtained using an Agilent Cary 7000 Universal Measurement Spectrophotometer (UMS) covering the 300-2500 nm wavelength range

(angle of incidence 8°). The absorptance spectrum A(λ) was obtained according to the formula A(λ)=100%-R(λ) using measured reflectance R(λ). T(λ) is assumed to be zero for the two types of absorbers using thick IR metal reflectors. The emittance of solar absorbing coatings for solar thermal applications was measured using a custom built emissometer heated to 82°C. The broadband thermopile sensor used detects thermal radiation over the 2.5 - 50 μm spectral range. The calibration of the instrument was conducted using an Al reference sample. Spectroscopic ellipsometry using a J.A. Woollam Co., Variable Angle Spectroscopic Ellipsometer (VASE) was used for determination of the optical constants. The ellipsometric parameters were measured in the 300 - 3000 nm wavelength range in 5 nm steps at angles of 60°, 70° and 75°.

For a comprehensive analysis of these spectrally selective solar absorbers, a theoretical model of the stack was built using the WVASE software (J.A. Woollam Co.). The generated results were fitted to the experimentally measured ellipsometric parameters and measured reflectance spectra, and then were displayed in terms of the final reflectance spectra for the best fit multi-layer model of the coating.

5.3 Algorithm to design a nearly ideal cermet-based spectrally-selective solar absorbing stack

A nearly ideal solar absorptance by a cermet-based Ta:SiO_2 stack was achieved using a newly designed algorithm for fitting and designing ellipsometry data. In this approach the WVASE software was used to build a theoretical model and predict the optical response of the absorber for incident sunlight in an iterative fashion. This resulted in the efficient spectrally selective response of the Ta:SiO_2 solar absorber using algorithm shown in Figure 5.1. The algorithm has seven key cycles and after each cycle an ideal spectrally selective absorber can be designed. The first cycle is comprised of the correct selection of the IR back reflector as the main element in the spectrally selective absorber preventing heat loss by radiation. The second part of the first cycle is made up of a more complex procedure, where both compatibility of the metal particles and dielectric matrix is tested to build a cermet layer with an optimal thickness and optimal volume ratio of metal particles to the host matrix. If a nearly ideal cermet based solar absorber can be

achieved at this stage, then an optical model can be transferred to the experimental stage and further tested.

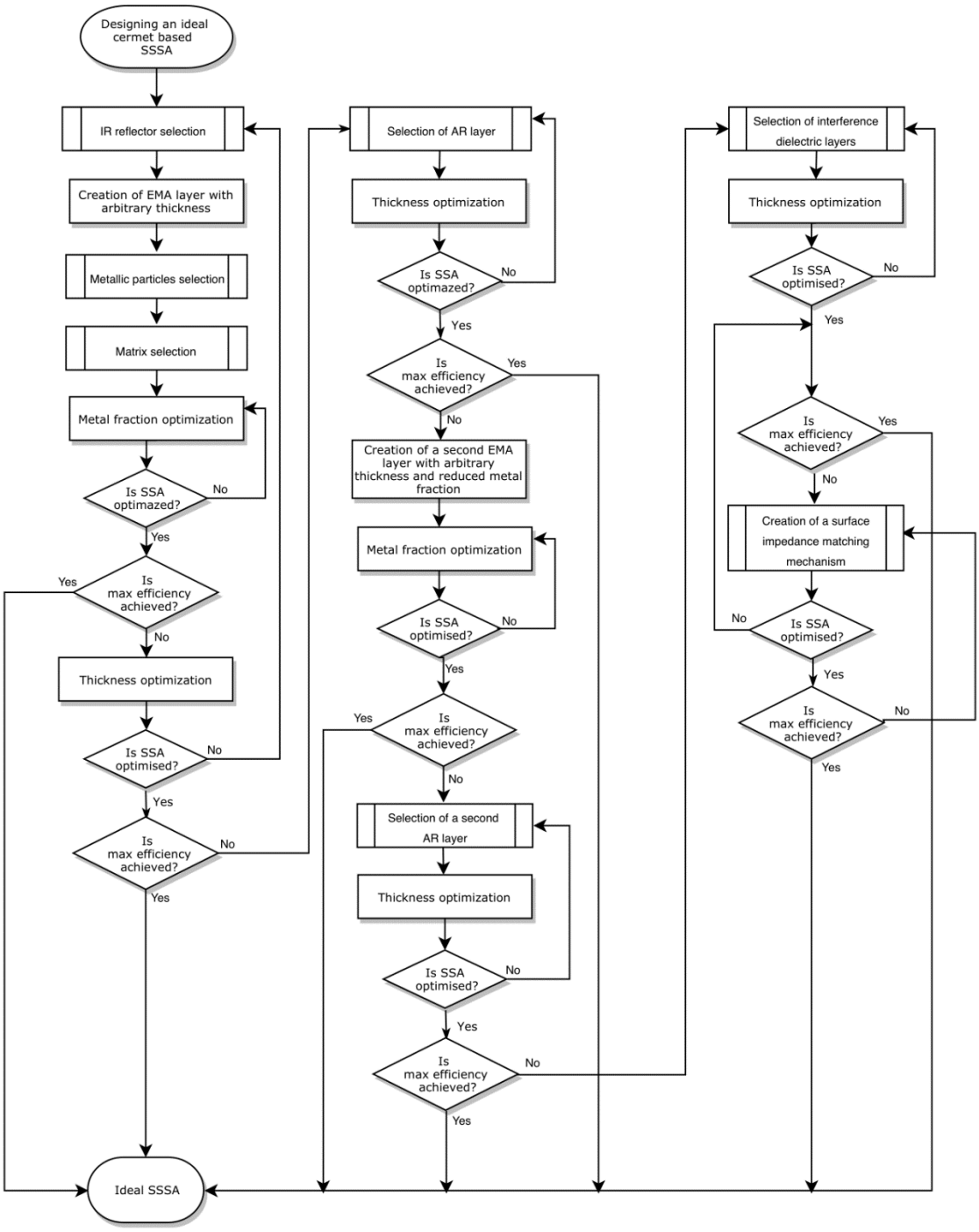

Figure 5.1 – Algorithm to design an ideal spectrally selective solar absorber (SSA) using a cermet approach, employed in the current research work

In an ideal case scenario, the theoretical prediction of the absorber's optical behavior should coincide with the experimentally obtained one, but this is not always possible due

to non-ideal conditions during a manufacturing process or if precise control is not always achievable. This may include residual foreign particle adsorption on the surface of the forming film or deviations associated with a control of the thickness of each layer down to 1 nm accuracy range. The latter results in a modified position or amplitude of the interference peaks in the measured reflectance/absorptance spectrum, and for a reduced absorption of the incident photons at the energy spectrum range where their intensity reaches the highest values or vice versa. The level of crystallinity of the deposited thin film also contributes, leading to modified *n* & *k* optical constants of each layer.

If finishing the first cycle of the algorithm in Figure 5.1 does not result in the most efficient spectrally selective solar absorber (SSSA), then an improvement in the efficiency is achieved through the subsequent cycles, where an additional cermet layer can be added with a modified metallic particle volume fraction in both cermet layers. Additional antireflective layers can be used, which also serve as a protection against rapid oxidation or deterioration of the lower stack layers. Finally, a further and last improvement that can be made to SSSA after selection of the main absorbing layers and AR layers is finding an impedance matching mechanism between the air/vacuum media and the SSSA, which sometimes can be a double-edged sword. This is due to the fact that often such a mechanism is achieved through roughening of the surface or creation of the porosity in the top layer, attributes which are known to be less resistive to elevated temperature exposure.

Ideally, fewer layers in the SSSA are preferable for a higher degree of stability when the sample is annealed, particularly due to generation of less thermal stress as a result of thermal expansion coefficient mismatch between each material. It should be highlighted that constructing a cermet-based SSSA for high temperature CSP applications is a sophisticated process with three key parameters: 1) high solar absorptance 2) low thermal emittance 3) high thermal stability, where the first two are to remain unchanged or if changed, then with an acceptable degree not significantly influencing the performance of the SSSA after annealing.

In the current research four cycles were used to design a desired spectrally selective response of the double cermet Ta:SiO_2 solar absorber, where the algorithm cycle was concluded at the construction of the second cermet layer, enabling achievement of a 97.5% solar absorptance. A further boost to nearly 100% is possible by going directly to the final impedance matching cycle.

5.4 Structural characterization of Ta:SiO_2 stacks

Two types of SSCs were developed in this work and are represented in Figure 5.2. The two stacks included four principal layers, IR reflector (Pt or Ta), high metal volume fraction (HMVF) cermet layer (Ta:SiO_2), low metal volume fraction (LMVF) cermet layer (Ta:SiO_2), AR layer (SiO_2). The cermet-based design was employed using Ta metal as a metallic inclusion in a SiO_2 host dielectric matrix. Tantalum is very refractory both on its own and when it forms compounds with boron, nitrogen or carbon. It is also known to be used as a replacement for platinum in laboratory equipment that must be highly corrosion resistant. The potential of Ta for high temperature CSP applications has been investigated by other workers as a photonic crystal structure [124, 125], as tantalum thin films [126], and as a diffusion barrier in spectrally selective multilayer structures [127]. However, to my knowledge, Ta was never investigated previously for use as the metallic particle in a cermet-based SSC. In the present work a SiO_2 matrix was chosen due to the proven thermal stability when used as a host matrix in SSC composites [60].

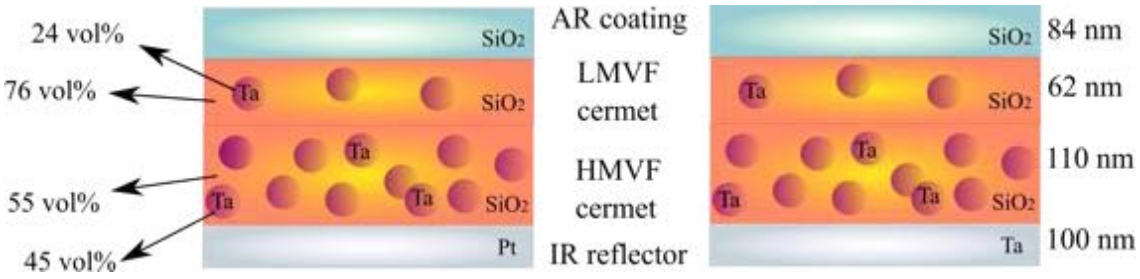

a) b)

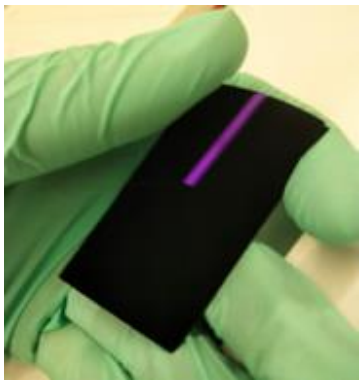

c)

Figure 5.2 – Design and top view of sputtered Ta:SiO_2 cermet based SSCs a) Ta:SiO_2 stack using Pt reflector b) Ta:SiO_2 stack using Ta reflector c) top view

A selection of Pt or Ta as back reflectors was mad, due to their lower reactivity with the Si substrate, compared to other refractory metals as described in Chapter 6. The volume of the Ta inclusions in two cermets was chosen in such a way to achieve the highest possible solar absorptance using the theoretical model developed in the WVASE software using the EMA approximation, for Figure 5.3a. The model was comprised of the stack with the layers as per Figure 5.2, where LMVF was modelled using Maxwell-Garnett approximation with varied volume content of Ta particles, Figure 5.3a and HMVF was represented by the Brueggemann model with the varied volume content of Ta inclusions as seen in Figure 5.3a.

a) b)

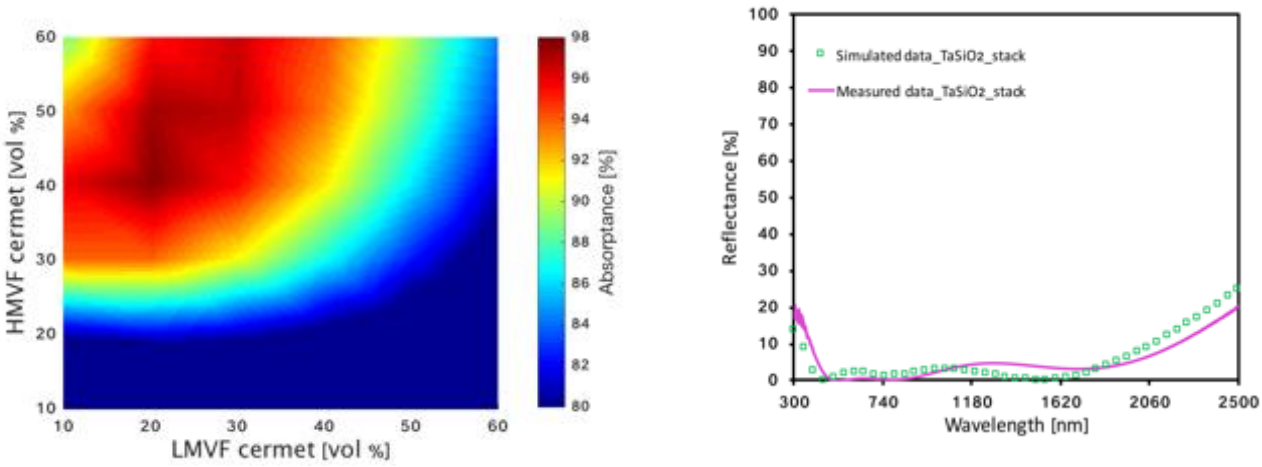

Figure 5.3 – a) Effect of a metal fraction in the cermet layers on optical response of the Ta:SiO_2 stack, b) comparison of the theoretical and measured optical response of the Ta:SiO_2 stack using Pt as a back reflector

As seen from the simulated results, Figure 5.3a, the optimal amount of the Ta for the HMVF layer is within 38 vol% - 50 vol% range and for the LMVF it comprised 16 vol% - 26 vol%. Hence, the depicted best theoretical values were 42 vol% and 20 vol% for the HMVF and the LMVF layers, respectively, as then a maximum solar absorptance surpassing 97% was achieved. To test the validity of the theoretical simulation, the measured reflectance spectrum of the produced stack is compared to the model in Figure 5.3b. The experimental reflectance spectrum of the stack is in a good agreement with prediction, confirming the validity of the chosen Ta:SiO_2 cermet-based design.

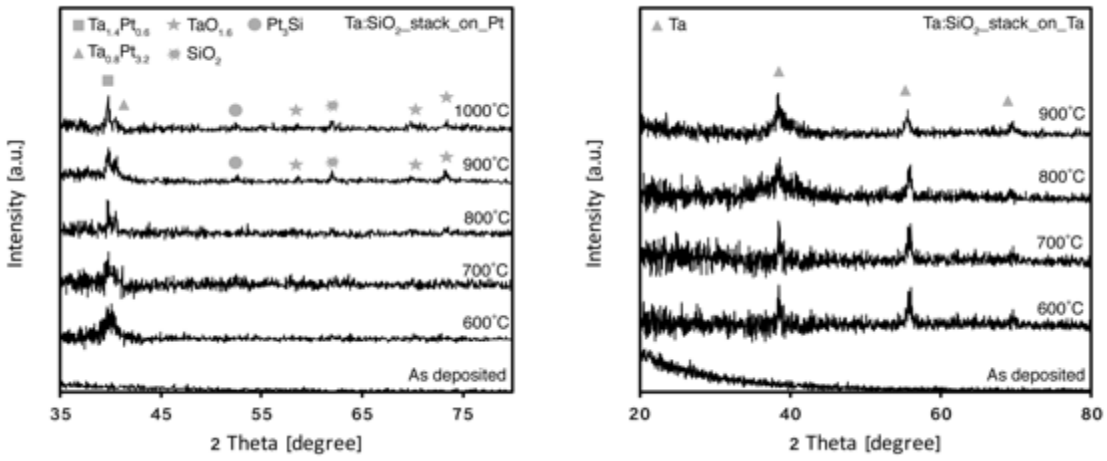

a) b)

Figure 5.4 – XRD results for as deposited and annealed for 1 hour Ta:SiO_2 cermet based stacks using a) Pt and b) Ta IR reflectors

Figure 5.4 shows the X-ray diffraction patterns of the Ta:SiO_2 stacks using the two types of back reflectors. From the Figure, it is seen that both pristine SSCs do not exhibit defined crystal structure, indicating an amorphous state of the deposited layers. There are no peaks identified for the Ta particles present in the cermet layers or for the back reflector for the Pt or Ta, pointing out a possible poor crystallization of the metals. The heat treatment of the solar absorbing coatings results in alloying of those Ta inclusions present in the HMVF cermet with the metal coming from the IR reflector when heated. In case of the Ta:SiO_2 stack on Pt, it leads to a formation of bimetallic nanoparticles of $Ta_{1.4}Pt_{0.6}$ at 600ºC and 700ºC. The further annealing up to 1000ºC induces a higher flux of Pt. In addition to the observed $Ta_{1.4}Pt_{0.6}$ inclusions, bimetallic particles with a higher fraction of Pt are formed, corresponding to $Ta_{0.8}Pt_{3.2}$. As will be shown further, in the ellipsometric characterization section, no alloying occurs in the top cermet layer, showing a high stability of the Ta particles in the LMVF cermet, where the access to the high volume source of the metal IR reflector out-diffusion is absent. As was shown in Chapter 5.1 for the Au/$AuAl_2$:AlN stack, the out-diffusion of the metal from the IR reflector is facilitated by the stress generation between the IR reflector and the Si substrate. Hence, it is worth testing with a different substrate in future in order to investigate if the thermally-induced diffusion from a back reflector can be suspended. Annealing of the stack at 900ºC leads to the partial-oxidation of the partially alloyed or unalloyed Ta particles leading to formation of a thin $TaO_{1.6}$ layer around the Ta inclusions, which might

be beneficial in limiting the Ta agglomeration and mobility and, as will be shown further, this does not lead to significant changes in the spectrally selective response of the stack. The formation of the tantalum oxides is also known to be beneficial due to a corrosion resistance enhancement of the tantalum. Finally, the XRD results indicate that 900ºC and 1000ºC annealing induces chemical reaction between the Pt reflector and the Si substrate. This can be avoided by placing a diffusion barrier between the Pt and Si. Finally, the observed SiO_2 peaks indicate the crystallization of the SiO_2 either in the host matrix and/or AR layer.

Taking into account the XRD results for the heat treated Ta:SiO_2 stack on Pt, it can be assumed that for the Ta:SiO_2 cermet multilayer on Ta, the formation of XRD peaks for Ta is due to alloying of the encapsulated Ta in the HMVF layer with the diffused Ta from the IR reflector (this is also confirmed by the Ellipsometry model and will be shown further). It can be noted that no oxidation of the Ta was indicated by the XRD experiments for the Ta:SiO_2 stack using the Ta reflector. Annealing of the sample at 1000ºC leads to the rapid chemical reaction between the Ta and the Si substrate and demolition of the coating (not shown here). The reaction between Ta and Si is known to start at 700ºC [128], but with no obvious XRD peaks. As was shown in [128], annealing of the Ta/Si at >700ºC leads to much pronounced XRD peaks and their intensity growth, assuming faster chemical reaction between Si and Ta. By contrast, in the Ta:SiO_2 stack using the Pt reflector, this reaction happens more slowly, starting at 900ºC and increasing to 1100ºC. At 1100ºC a partial delamination/flaking of the coating occurred. The preserved areas still exhibited specular reflectance and dark violet color, showing the possible stability of the upper layers of the SSC. Hence, it can be concluded, that the Ta:SiO_2 cermet-based absorber using a Pt reflector might resist 1100ºC annealing if a diffusion barrier between the Pt reflector and the Si substrate is provided, or if the Si substrate is replaced. This theory should be tested in future.

The SEM cross-sectional measurements show a successful deposition of the cermet based Ta:SiO_2 multilayer stack with four distinct layers and boundaries between them. The contrast between the layers indicates the degree of metallization of the deposited layers.

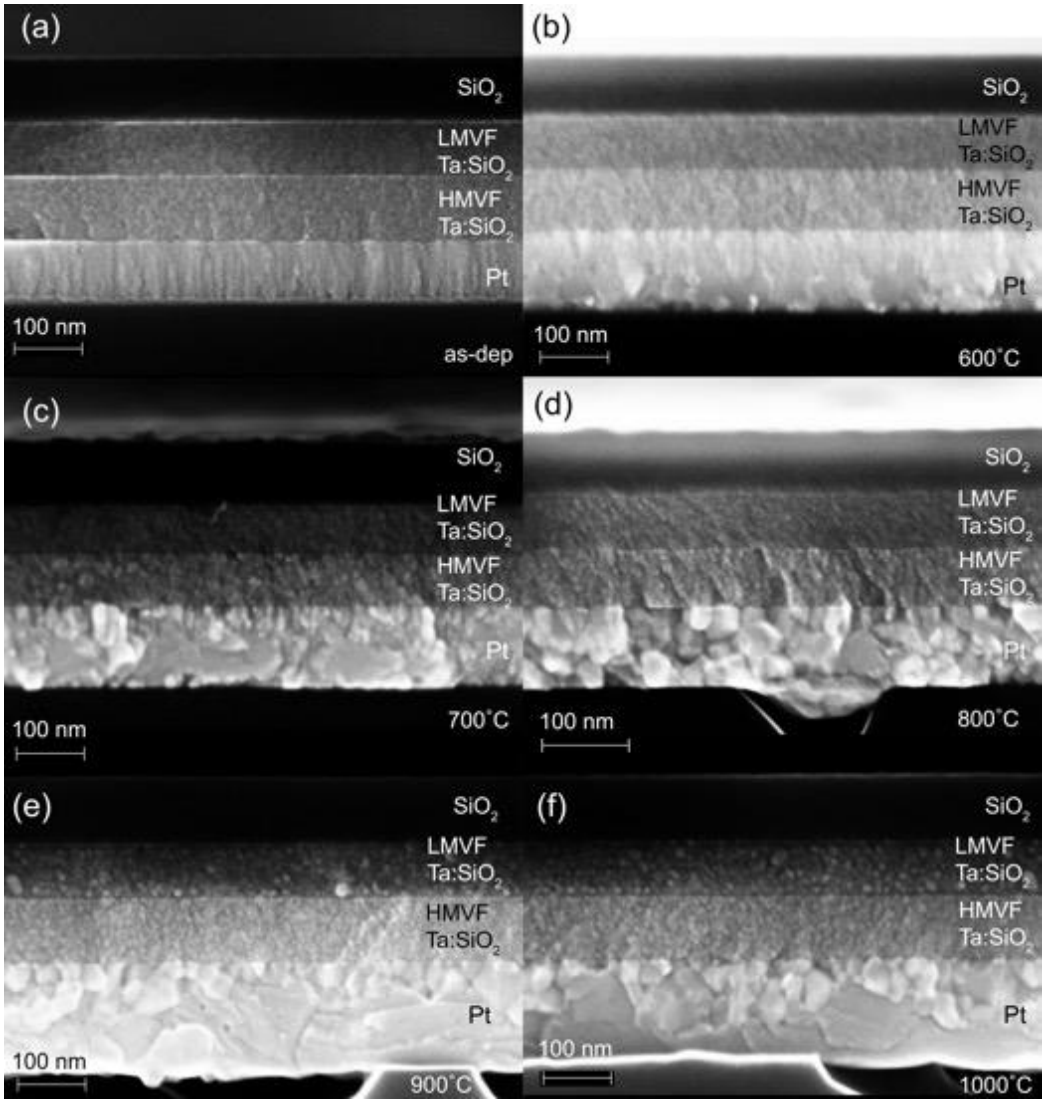

Figure 5.5 – Cross-Sectional SEM images of Ta:SiO_2 stack using Pt reflector, a) as-deposited, b) annealed at 600ºC, c) 700ºC, d) , 800ºC, e) 1000ºC.

It is clear that, for the Ta:SiO_2 layer with 24 vol% of Ta, a darker contrast is observed compared to the Ta:SiO_2 layer with 45 vol% of Ta, confirming the presence of Ta in the two cermets using SiO_2 as a host matrix. Annealing of the Ta:SiO_2 solar absorber at 600ºC does not lead to any obvious structural modifications and the clear boundaries between the layers are still preserved, indicating a good thermal stability of the sample. This is also observed for the further annealing steps at 700ºC, 800ºC and 1000ºC. Annealing at 700ºC leads to an obvious recrystallization of the Pt back reflector from an initial columnar structure, Figure 5.5a,c, which will be shown to result in emittance reduction (Section 5.3.6). Finally, the cross-sectional SEM image of the Ta:SiO_2 stack on Pt after annealing at 1000ºC enables to detect the Ta spherical-like nanoparticles in the LMVF

cermet layer, 5.3.5f, which was not well observed for the as-deposited sample and early stages of annealing. This indicates the a thermally induced crystallization of the Ta inclusions acquiring a more spherical shape, which is in agreement with the built ellipsometrical model and will be discussed further.

5.5 Ellipsometric characterization of single Ta:SiO_2 cermet layers

The fitting of the optical constants of the measured samples was conducted by building a general oscillator model, as was shown in Chapter 2. Depending on the material type (metal, semiconductor or insulator) a different set of oscillators can be used. For the deposited Ta:SiO_2 cermet layers Lorentz, Tauc-Lorentz and Drude oscillators were used showing the contribution of polarized bound electrons in the UV and visible range (Lorentz, Tauc-Lorentz oscillators) and the contribution of free electrons (Drude oscillator) accelerated by the applied electric field. The complex dielectric constant ($\tilde{\varepsilon}$) using a Drude model is defined as [129]:

$$\tilde{\varepsilon} = \varepsilon_1 + i\varepsilon_2 = \varepsilon_\infty - \frac{\omega_p^2}{\omega^2 + i\omega\Gamma} \tag{5.1}$$

where $\varepsilon_1$and ε_2 are real and imaginary parts of the complex dielectric constant, respectively; ω_p is a resonance (plasma) frequency at which $\varepsilon_1 \to 0$ and $\varepsilon_2 < 1$; Γ is a damping factor containing a drift velocity of the electrons and describes the number of collisions of free electrons per second when accelerated by the optical electric field and ω is an angular frequency of the incident electromagnetic wave.

Formula (5.1) takes the following form within the WVASE software in order to build a Drude oscillator fit:

$$\tilde{\varepsilon}_{n\_Drd} = -\frac{A_n Br_n}{E^2 + iBr_n \mathrm{E}} \tag{5.2}$$

where A_n is a Drude oscillator strength related to plasma frequency and $A_n * Br_n = \varepsilon_\infty E_p^2$, where ε_∞ is a dielectric constant responsible for residual absorption above the frequency where ε_1 becomes negative E_p; Br_n is an oscillator broadness [130].

The friction force in the oscillator model (or drift velocity) is described by the damping of the oscillator and consequently causes line broadening (represented as the Br_n parameter in the Drude model, of WVASE software). For the two Ta:SiO_2 layers used for the LMVF and HMVF, the Br_n parameter was 18.9 eV and 5.85 eV respectively, which shows a higher degree of damping in the LMVF layer Ta and more metallic response in the HMVF layer. For the Ta:SiO_2 composite layer with the lower metallic content the free carrier density is reduced compared to the HMVF Ta:SiO_2 cermet, hence, the value of A_n, which is connected with ω_p is pushed towards IR region and equals 0.3 eV compared to 6.25 eV for the HMVF, which is well observed in the current case, Figure 5.6.

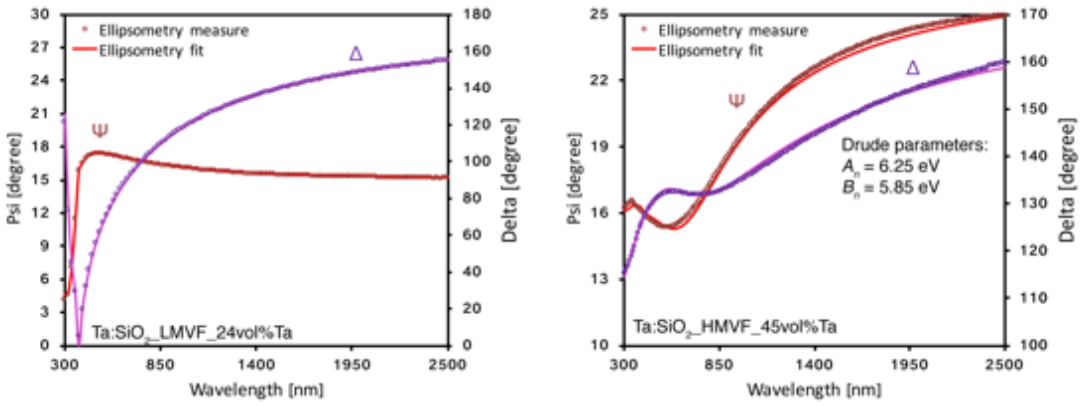

Figure 5.6 – Measured psi and delta parameters for the LMVF and HMVF Ta:SiO_2 single layers and the ellipsometric fit using oscillator model with the Drude parameters employed to make a fit. The overall fit was made using single Drude oscillator and three Lorentz oscillators

The optical constants *n,k* of single Ta:SiO_2 cermet layers with 24 vol% and 45 vol% of Ta were derived from the ellipsometry measurements using the EMA approach, Figure 5.7. The fit to measured ellipsometric parameters for the HMVF Ta:SiO_2 cermet layer was conducted using a Bruggeman EMA approximation, which is ideal for two phase media with a high volume fraction of metal inclusions (30 to 40 vol%). For the current cermet with 45 vol% of Ta, the *n,k* increases steadily with the wavelength, identifying a percolating metallic-like character of this layer. For the LMVF Ta:SiO_2 layer, a Maxwell – Garnett EMA was employed to make a perfect ellipsometric fit. For the composite with 24 vol% of Ta in SiO_2 media, the M-G is the preferred approach due to the low filling factor of the Ta inclusions, assumed to be separated by the dielectric host. The derived

optical constants characterize the LMVF layer as a semi-metallic layer, where the extinction coefficient monotonically extinguishes with the wavelength approaching zero value at the end of the spectrum range. The exploitation of these two layers on top of each other with a low refractive index top layer such as SiO_2 or other dielectric material creates beneficial conditions to decrease the impedance mismatch for the entering light wave travelling from the vacuum/air into the solar absorber, thus, enhancing a light absorption of the graded stack.

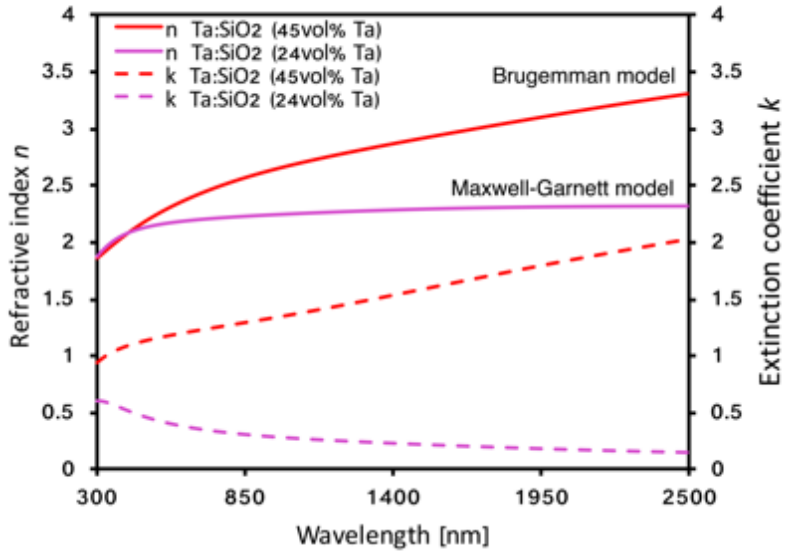

Figure 5.7 – The optical constants of the two Ta:SiO_2 cermet layers with varied metallic content

5.6 Ellipsometric characterization of Ta:SiO_2 solar absorber before and after annealing

A Ta:SiO_2 cermet-based multilayer solar absorber employing structural design, shown in Figure 5.2, was characterized by ellipsometry before and after each annealing step. The measured psi and delta ellipsometric parameters are displayed in Figure 5.8. In order to achieve an ideal fit, a four-layer model was built using WVASE software, consisting of the Si substrate, Pt or Ta IR reflecting layers depending on the stack, two cermet layers with varied Ta fractions in the SiO_2 media using an EMA approximation as described in the previous section and the SiO_2 layer. The fit to the Pt, Ta and SiO_2 layers was conducted in advance for separately deposited films and the fitted optical constants

were used in the stack's model. To fit the measured data, four main parameters were adjusted upon 1 hour thermal treatment in vacuum at 600ºC, 700ºC, 800ºC, 900ºC, 1000ºC for both stacks. The first parameter is a volume fraction of the Ta in the LMVF layer, the second is the volume fraction of the Ta in the HMVF layer, the third is the depolarization factor (DF) of the metal inclusions, characterizing a possible change in the shape after heat treatment and the fourth parameter is the thickness of each layer. Since the thickness for each film in the stack remained at the relatively constant value, the values are not depicted in the graph.

The Ta:SiO_2 stack using Pt as the IR reflector will be discussed first, followed by the Ta:SiO_2 stack using the Ta reflector. The ellipsometric studies of the as-deposited Ta:SiO_2 solar absorber on Pt show that a perfect fit was conducted using 24 vol% of Ta for the LMVF layer and 45 vol% of Ta for the HMVF cermet along with DF = 0.183 and DF = 0.333, respectively, as initial parameters, Figure 5.8a. The defined DF value suggests an ellipsoidal-like shape of the encapsulated metal particles as was shown in [131] and [132]. The first annealing of the stack at 600ºC in vacuum does not lead to noticeable changes in the top cermet layer and the shape of the Ta particles, showing a high level of thermal stability of the top cermet. However, there were some changes in the bottom cermet layer, which was adjacent to the Pt reflector. In this layer the thermal treatment induces diffusion of the Pt atomic species into the cermet to about 0.45 vol%, which is in agreement with the XRD results and results in the formation of bimetallic $Ta_{1.4}Pt_{0.6}$ particles. As will be shown further, in the spectroscopic characterization section, this is beneficial and has a positive effect on the integrated solar absorptance of the stack. The further annealing at 700ºC and 800ºC did show reshaping of the Ta particles in the top cermet which acquired a more spherical shape by reducing the axis aspect ratio of the initially ellipsoidal Ta particles. This is reflected in the values of the depolarization factors, which are 0.20 and 0.23 respectively, Figure 5.8c,d. The amount of the Ta inclusions remained unchanged, at around 24 vol%, demonstrating the absence of diffusion of any metallic species from the bottom cermet layer.

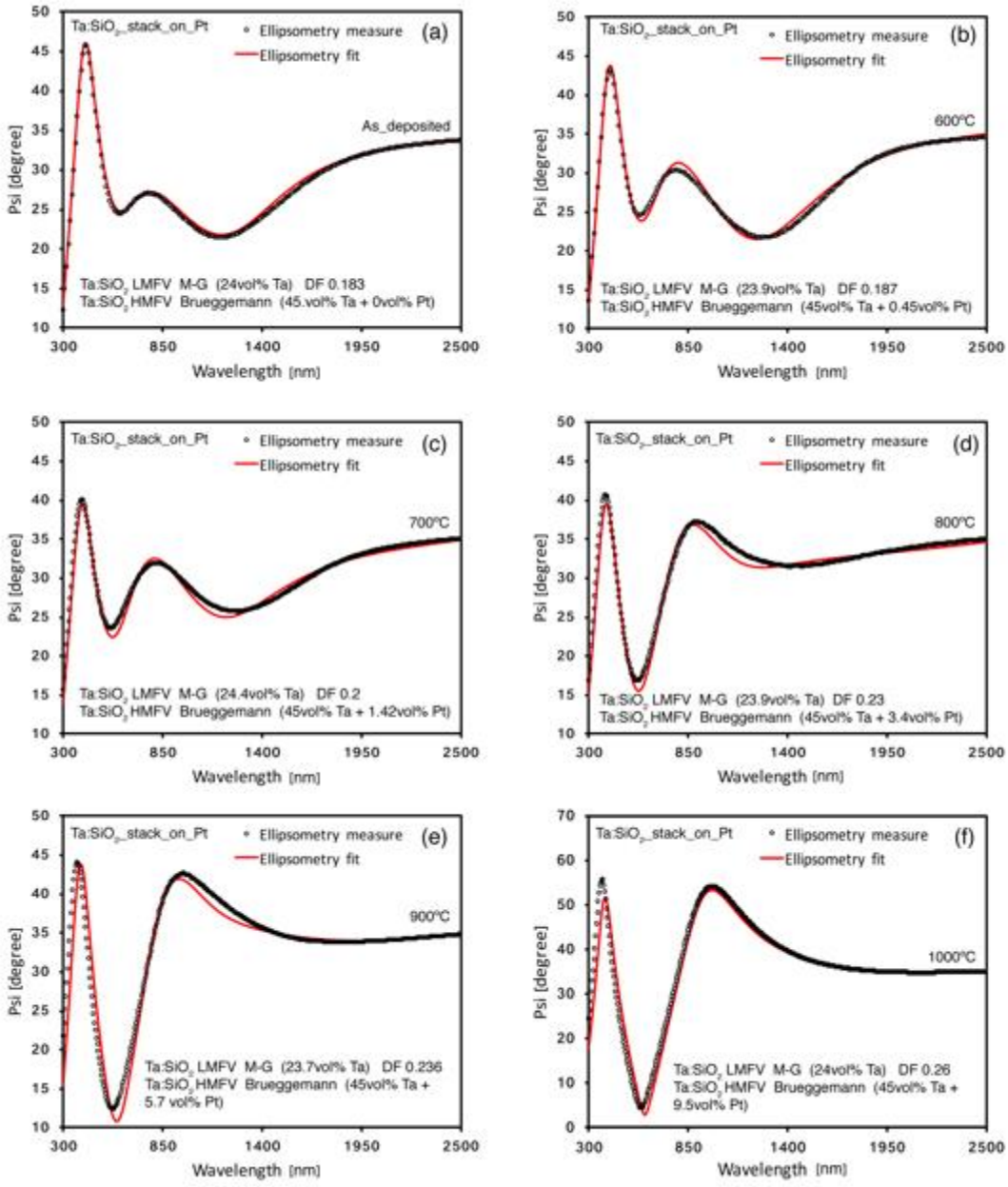

Figure 5.8 – Ellipsometric measurement and fit to the as–deposited and annealed at different temperatures Ta:SiO_2 cermet based stack on Pt reflector (DF is depolarization factor)

The 700ºC and 800ºC thermal treatments further facilitate the upwards diffusion of the Pt, resulting in the overall increase of the Pt vol% in the bottom cermet layer by 1 vol% and 2 vol%, respectively, which, with respect to the XRD analysis, leads to a formation of the bimetallic $Ta_{0.8}Pt_{3.2}$ particles, dominated by the Pt fraction. In its turn, this has a most beneficial effect on the solar absorptance (as will be shown later). Annealing at 900ºC still does not influence the amount of the Ta inclusions in the LMVF

layer and, considering the absence of any Ta peaks in the XRD, it seems that no agglomeration of the Ta particles has occurred. At the same time, the amount of migrated Pt species has increased by 2.4 vol% in the HMVF layer, Figure 5.8e. Finally, the 1000ºC heat treatment is associated with further minor reshaping of the Ta particles with unchanged 24 vol% in the top cermet resulting in DF = 0.26 compared to initial 0.183, Figure 5.8f. This still characterizes Ta particles as ellipsoidal as the depolarization factor lies within the ellipsoidal shape range [131]. The 1000ºC heat treatment produced a HMVF cermet with the highest amount of Pt, resulting in additional 9.5 vol% of metallic fraction compared to the as-deposited one. Taking into account the simulation results for the volume fraction of metal in the two cermets in Figure 5.3a, even this additional amount of the metal should not affect the absorption capabilities of the multilayer stack significantly, and the solar absorption of the Ta:SiO_2 cermet-based coating should remain within 94 - 96% range.

The ellipsometric characterization of the Ta:SiO_2 multilayer solar absorber with the Ta back reflector is shown in Figure 5.9. A nearly ideal fit to the experimental ellipsometric data was achieved for the sample after each step of annealing. Like in the previous section, the initial parameters were 24.8 vol% of the Ta inclusions for the LMVF layer with ellipsoid shape as defined by the depolarization factor (0.174) and 46 vol% of Ta for the HMVF layer. As was observed for the Ta:SiO_2 stack using the Pt reflector, annealing induces thermally-activated diffusion of the metallic species from the IR reflector. For the current solar absorber using Ta as a back reflector, the overall amount of diffused Ta is less at each annealing step. The additional amount of migrated Ta at the very beginning of the series of annealing treatments accounted for 0.28 vol%, compared to 0.45 vol% in case of Pt reflector. For each annealing step this amount of Ta continued to increase steadily, but still being lower than if a Pt reflector was used. The evolution of the depolarization factor demonstrates a similar trend to the previous stack in reshaping of the encapsulated particles in the LMVF layer, starting from the value of 0.174 and ending up with 0.21 at 900ºC. For the Ta:SiO_2 stack on the Pt reflector, DF equals 0.236 after 900ºC annealing, showing a slightly higher degree of reshaping of the elongated Ta particles and approaching a more spherical shape. This can be caused by the generation of a higher degree of thermal stresses coming from the bottom cermet layer having an additional metallic element, Pt, due to two reasons: 1) Pt has a different value of thermal coefficient of expansion compared to Ta and 2) higher volume of additional metallic fraction in the Ta:SiO_2 cermet using Pt reflector was achieved, compared to the Ta:SiO_2

cermet having Ta reflector underneath. The amount of the Ta particles in the LMVF layer remained at the relatively constant value, around 24 vol%. Since there is no obvious decreasing or increasing pattern for the Ta in the LMVF layer, a slight difference in the percentage of the Ta throughout the annealing process can be due to the initial randomized distribution of the Ta inclusions.

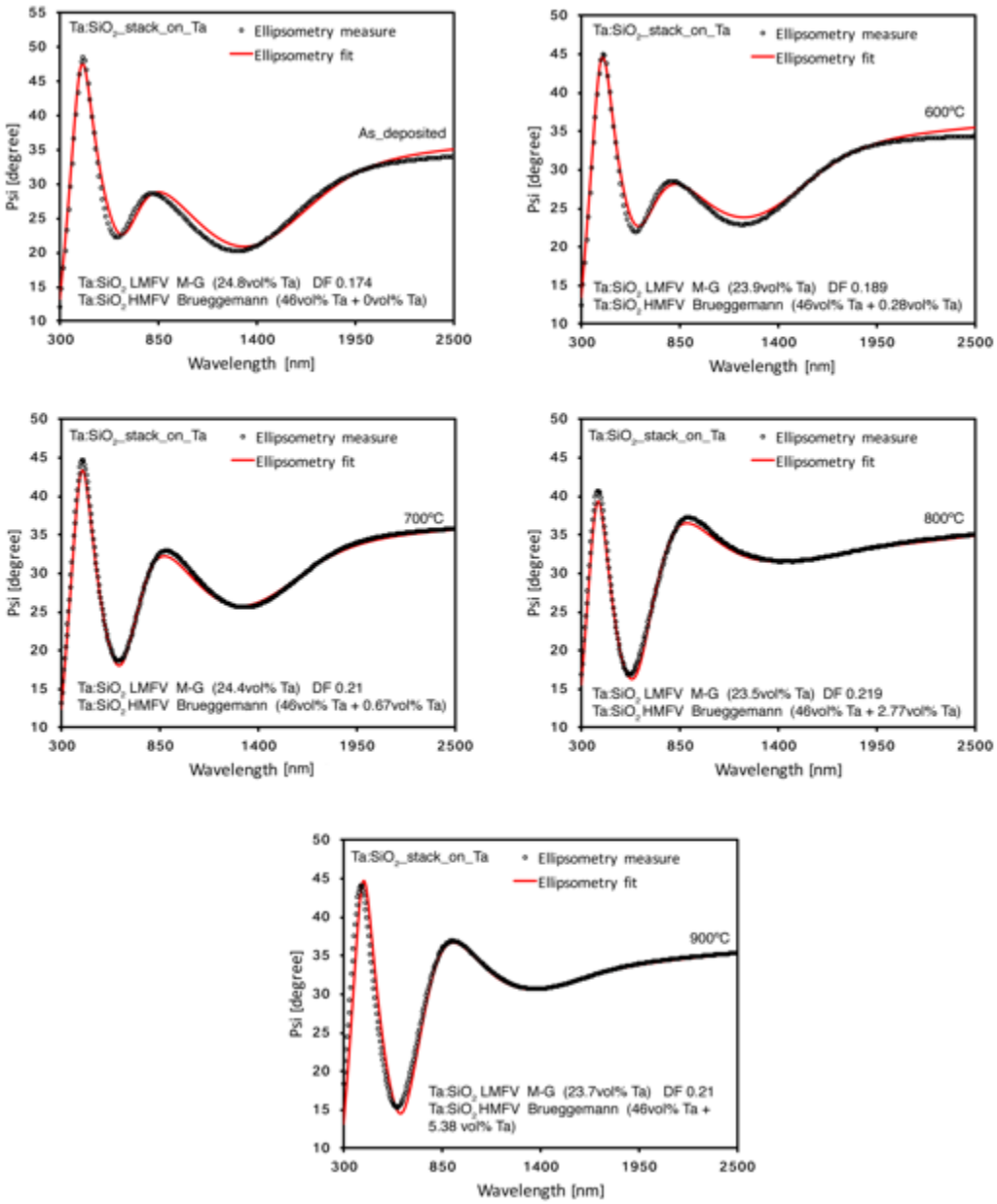

Figure 5.9 – Ellipsometric measurement and fit to as–deposited and annealed at different temperatures Ta:SiO_2 cermet based stack using Ta reflector (DF is depolarization factor)

5.7 Spectroscopic characterization before and after annealing

The spectrally selective response of the Ta:SiO_2 cermet-based multilayer stack (Pt reflector) was analyzed by combining the measured spectroscopic data in the UV-vis-near IR range and mid- and far-IR range, Figure 5.10. The stack demonstrates a broad solar absorptance from 300 nm up to 2500 nm. The calculated solar absorptance shows that the Ta:SiO_2 double cermet stack is capable of absorbing a remarkable 97.5% of incident solar radiation, with nearly 100% solar absorptance between 470 nm and 620 nm, demonstrating that this is the one of the highest solar absorptance that was achieved to date for the cermet-based spectrally selective solar absorbers that can endure high temperature exposure up to 1000ºC. As was shown in the literature review section, Pt:Al_2O_3 and Cr:Al_2O_3 cermet based solar absorbers also demonstrated solar absorptance of 98%, however, these stacks suffered degradation after low and mid temperature annealing, whereas the Ta:SiO_2 double cermet solar absorber not only demonstrates an initial high level of solar absorptance, but also shows a capacity to preserve it throughout the whole annealing process up to 1000ºC as will be shown further. The optical transition between high solar absorptance and high IR reflectance occurs within the range 2500 nm - 4500 nm range, resulting in a high degree of spectrally-selective response of the Ta:SiO_2 stack. The initial measured thermal emittance was low at 0.18 for the SSC with the Pt substrate and 0.21 for the one with the Ta substrate. The current stack was designed with a transition centered at 2500 nm, which is ideal for CSP applications up to 500ºC-600ºC. If the Ta:SiO_2 is to be used for the solar thermo-photovoltaic applications, the cut-off should be pushed towards shorter wavelengths, as shown in Figure 5.10, due to the shift in the black body radiation spectra at higher temperatures. This can be easily achieved by the modification of the volume percentage of Ta in both cermet layers plus thickness adjustment of each layer.

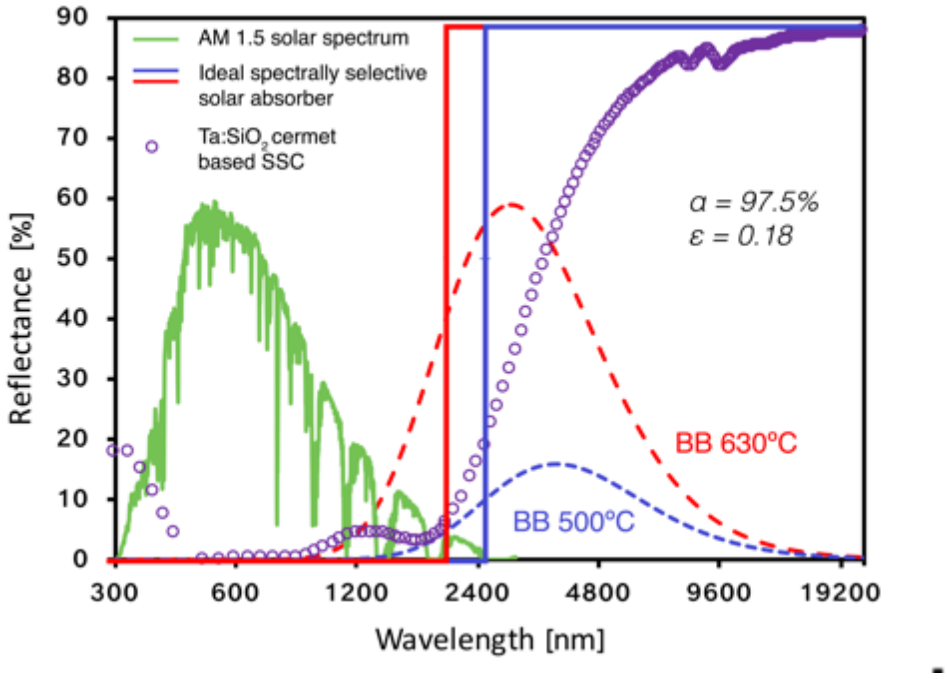

Figure 5.10 – Measured spectrally selective response of the Ta:SiO_2 on Pt reflector with a comparison to an ideal spectrally selective solar absorber

Figure 5.11 shows the reflectance of the Ta:SiO_2 cermet-based SSC using a Pt substrate. As was discussed in Chapter 5.1 for the Au/$AuAl_2$:AlN stack which was deposited, the angle of incidence dependence of solar absorptance of the SSC is one of the key characteristics when used in single axis tracking [94], but is rarely studied. The measurements show that Ta:SiO_2 is an excellent absorber over a broad angular range with solar absorptance of 97.5% up to 40º and 96.2% at 50º incidence with a strong solar absorptance from 350 nm to 2000 nm. These ranges match those in which the solar irradiation spectrum is most intense. At 60º incidence the solar absorptance is 93.2%, after which a decline is observed to 85% at 70º and 65% at 80°. These results are comparable to the Ni:Al_2O_3 solar absorber developed by Tesfamichael, which exhibited 95% solar absorptance at 50º and 80% at 70º [133], and for Mo:SiO_2 cermet based absorber developed by Zhang [96]. This angular dependence of solar absorptance for Ta:SiO_2 cermet absorbers is in agreement with Fresnel equation models of reflectance at each incidence where a rise in reflectance occurs with increase in the incidence angle. Additionally, a slight shift of the constructive interference maximum occurring for normal incidence at 640 nm, towards shorter wavelength is observed, and is attributed to the multilayer structure of the Ta:SiO_2 solar absorber. The constructive or destructive

interference patterns occur when incident electromagnetic waves at each angle interfere after refraction and reflection at the interfaces between internal layers.

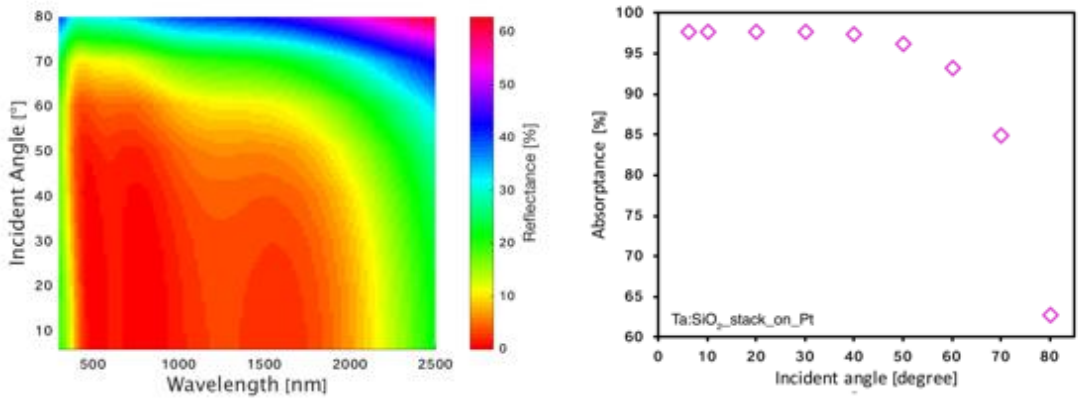

a) b)

Figure 5.11 – a) Measured reflectance of the Ta:SiO_2 stack on Pt reflector as function of the wave incident angle and b) calculated integrated solar absorptance

Figure 5.12 demonstrates the measured reflectance data for Ta:SiO_2 cermet-based stacks on Pt and Ta substrates before and after annealing. Both stacks show nearly identical reflectance patterns before annealing with the broad absorptance in the solar spectrum and two characteristic interference humps resulting from wave reflections at the boundaries of the four different layers with their particular *n* and *k*. The calculated solar absorptance values are 97.5% for the Ta:SiO_2 stack on Pt and 97.6% for the Ta:SiO_2 stack on Ta. An initial annealing in vacuum at 600ºC did not lead to any significant changes in either stack and only resulted in a minor reduction of the broad interference hump located around 1200 nm which slightly enhances solar absorptance by 0.2%. As discussed in the ellipsometric characterization section, this is due to an increase in the metallic fraction in the HMVF layer as a result of thermally activated diffusion of the metallic species from the back reflector, Pt or Ta. Annealing at 700ºC leads to a further reduction in the interference shoulder resulting in a remarkably high value of the solar absorptance for the Ta:SiO_2 stack on Pt of 98.2%. There was less change in the case of the Ta:SiO_2 stack on Ta. The slight increase in the reflectance in the near-IR range is attributed to two phenomena. Firstly, an increase in the metallic fraction in the HMVF layer due to migration of the metallic species from the back reflector during annealing contributes to more percolation in the cermet layer for higher reflectance in the near-IR range, as seen in Figure 5.8 and Figure 5.9. Secondly, the emittance measurements show reduction in

the thermal emittance for both stacks, from 0.19 to 0.17 (on Pt) and from 0.21 to 0.15 (on Ta). This is due to improved crystallinity of the back reflector which enhances reflectance due to reduced absorptance.

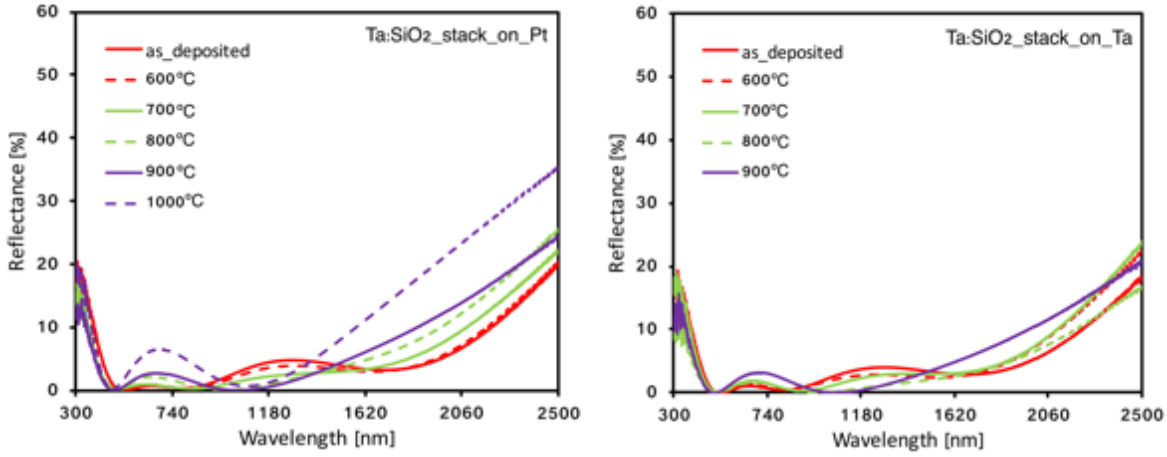

a) b)

Figure 5.12 – Reflectance spectra of the as-deposited and annealed for 1 hour in vacuum Ta:SiO_2 cermet based stacks using a) Pt and b) Ta reflectors

Annealing at 800ºC leads to a further change of optical constants in the HMVF cermet layer resulting in flattening of the constructive interference hump near 700 nm plus a further drop in the emittance values, to 0.156 (on Pt) and 0.11 (on Ta). This annealing of the Ta:SiO_2 solar absorber on Ta led to the highest value of solar absorptance achieved (98.4%) along with a low emittance, which is an excellent result, and due to a combination of an ideal amount of metal content in the HMVF cermet plus weakened interference effects between layers from the intrinsic absorptance in the cermets. Further annealing to 900ºC shows that both Ta:SiO_2 cermet-based stacks are stable, exhibiting very high solar absorptance near 97.4% with a further reduction in thermal emittance, 0.153 when on Pt. An excellent spectrally selective response is thus maintained. This impressive result indicates that the Ta:SiO_2 solar absorber can potentially be operated up to 900ºC in CSP applications without sacrificing the solar absorptance or spectral selectivity due to an associated reduction in thermal emittance. Annealing at 1000ºC demonstrated that the Ta:SiO_2 layers on Pt, despite the formation of platinum silicide (according to XRD analysis), preserved a low thermal emittance of $\varepsilon = 0.16$, but incurred a slight reduction in solar absorptance of 2.5% to 94.9%. This minor drop in the solar absorptance is due to a further increase in the Pt fraction in the HMVF layer as a result of

thermally activated diffusion. In the reflectance spectra, Figure 5.12a, this is the cause of a rise in the reflectance in the near-IR range. Exposure of the Ta:SiO_2 SSC on the Ta reflector at 1000ºC has a detrimental effect on the stability of this stack and, as was discussed before in the XRD section, leads to a rapid chemical reaction between Si substrate and the Ta reflector.

Table 5.1 – a) Calculated integrated solar absorptance and b) measured thermal emittance for as-deposited and annealed for 1 hour in the vacuum at corresponding temperatures Ta:SiO_2 cermet based stacks using Pt and Ta reflectors

Temperature, °C	Ta back-reflector		Pt back-reflector	
	α	*E*	α	*E*
As-deposited	97.6	0.21	97.5	0.18
500	97.8	0.18	97.7	0.18
600	97.7	0.15	98.2	0.17
700	98.4	0.11	97.7	0.16
800	97.4	-	97.5	0.15
900	-	-	94.9	0.15

5.8 Conclusions

In the current work novel Ta:SiO_2 double cermet spectrally-selective solar absorbers using Pt and Ta substrates were developed with a remarkably high value of solar absorptance (close to 97.5%) and a low thermal emittance. The high degree of spectral selectivity was achieved due to using a double layer cermet approach with varied metallic fractions in each cermet layer, topped with an antireflective layer. The Ta:SiO_2 stack demonstrated a flat angular solar absorptance, of 97% out to 40º incidence angle, and 93% out to 60º. The magnetron-sputtered solar absorbers were exposed to the series of thermal annealing tests up to 1100ºC in order to test the possibility of their use in advanced the high temperature CSP applications. Ellispometric and XRD characterization of the Ta:SiO_2 SSCs showed that the top LMVF cermet layer is stable at high temperatures in stacks deposited on Pt or Ta, while in the inner HMVF layer the Ta inclusions are alloyed by thermal diffusion of metallic species from the metal base layer.

In the case of the Pt IR reflector this leads to the formation of bimetallic particles composed of Ta and Pt, and in case of the Ta substrate, the Ta particles grow with a change in size and in shape. Both phenomena have a beneficial effect and solar absorptance rises after each of 100°C annealing steps up to 800ºC. This leads to a solar absorptance of up to 98.4%. After the 900ºC annealing tests, the absorptance of both stacks returned to their high initial value, 97.5%. Annealing of these stacks at 1000ºC showed that the material in the underlying substrate and the choice of the metallic IR on that substrate can both influence the upper limits of sample stability. It also shows that the Ta:SiO_2 stack on the Pt IR reflector shows thermo-optical stability, hence the preservation of its spectrally-selective response, despite the formation of platinum silicide at high temperatures underneath the Pt IR reflector. In contrast, the Ta:SiO_2 multilayer coating on the Ta IR reflector was not able to cope with vacuum exposure at 1000ºC due to a rapid chemical reaction between the Ta layer and the Si substrate below. The use of a diffusion barrier is desirable and should be tested in future. The initial thermal emittance of both cermet-based stacks was low, at 0.18 (with Pt IR reflector) and 0.21 (with Ta IR reflector). The annealing process has a positive influence on the thermal emittance of the both initially deposited reflectors, due to increased size of their crystallites for lower resistive loss. This was observed to a higher degree for the Ta IR reflector, and led to a final drop in thermal emittance of 0.15 and 0.04 in the two samples. Exploitation of the Ta:SiO_2 spectrally selective solar absorbing stacks when on Pt would thus be beneficial for efficient solar thermal conversion up to 1000ºC. If deposited on Ta then high efficiency to 900°C seems achievable.

Chapter 6
Selection of a back reflector for stable solar thermal collection at ultra-high temperature

A back infrared reflector is one of the key components in a spectrally selective solar absorbing coating and provides an ability to achieve a spectrally selective response by suppressing radiative heat loss. While a high degree of solar absorptance is undoubtedly a primary goal in securing a high efficiency of the solar absorber, low IR emittance also adds to the efficiency of the absorber according to formula (1.13). As briefly discussed in the introduction chapter, better solar absorbers are also IR reflectors and thus show spectral selectivity in the solar-IR range. They are up to 20% more efficient than non-selective coatings. To be of use for power generation at temperatures from 650°C to 1100°C this layer must maintain both a high solar absorptance and a low thermal emittance. Apart from the spectral selection, a back reflector must survive very prolonged exposure to high temperatures. One of the common reasons for a SSC failure is instability of the IR reflecting metallic layer as a result of diffusion, oxidation or reaction with a substrate. This chapter addresses the back reflector in greater detail, in particular the way in which deposition parameters influence its optical response. The issue of thermal stability is covered in chapter 5.

Metals and conducting nitrides and oxides are known to be good IR reflectors due to their high density of mobile carriers responsible for conduction processes, and are often used as IR mirrors in solar thermal applications. Overall, their difference in solar and IR spectral response depends on the substrate carrier density, whether these carriers are s- or d-band electrons, their Drude relaxation time, and their density-of-states as a function of energy since interband transitions depend on the joint density of states for photon absorption applicable at a particular energy interval as demonstrated in [134]. Band structure involved includes the width of the energy bands, their position relative to the Fermi level, and their overlap with other bands such as s-p hybrid bands if present. The distance of the d-band energy levels to the Fermi level, their population or filling at

temperature T Kelvin and the mechanism for interband transitions are also important. In general 3d and 4d metallic band structures are the focus in the present study as these metals have much higher melting points and oxidize less easily than s-carrier metals.

When excited by an incident electromagnetic wave, the mobile carriers located in the surface layer of a metal oscillate. This generates a secondary electromagnetic wave whose normal component is opposite to that of the incident electromagnetic wave, thus reflecting some or most of the incident light, especially in the IR. Due to the high density of the mobile carriers, even thin layers of metals both conduct electricity and reflect incident light, however, very thin layers, below about 20 nm depending on the element, are semi-transparent. A characteristic of metals is that they have a low reflectivity in the visible range and an abrupt rise in reflectivity in the near IR without any significant absorption dips. If dips do occur in experimental spectra then they might be due to the presence of oxides on the surface of the metal causing some partial IR absorptance. This is especially the case for Al films, which after deposition tend to form a thin Al_2O_3 layer on top due to a high reactivity of Al with oxygen. Thus, securing high vacuum and purity of the metal targets and using an inert gas during the sputtering process of the metal is a necessary condition to obtain a highly reflective surface.

Silver and aluminium are known to be the best IR reflectors due to their high conductivity and they reach almost 98% reflectance in the IR [135]. While an extremely high level of heat can be retained inside the solar absorbing coating using Ag or Al IR reflectors underneath the coating, the structural thermo-stability of the SSC may deteriorate at temperatures exceeding 630ºC due to the lower melting points of these metals (960ºC and 660ºC respectively), compared to the refractory metals. This creates a challenge in the selection of the reflective layer for high temperature CSP applications exceeding 630ºC.

Apart from this, as has been shown by Lampert, various reflectors affect the efficiency of the solar collector differently [14]. In that work, three different reflectors with black chrome on top were tested: copper, nickel plated steel and steel, in addition with a non-selective coating (black paint). Depending on the reflector used, the value for collector's efficiency ranged mainly between 50% - 70% and 40% - 60 % (black paint), respectively, Figure 6.1, with more details described in [14]. For the much higher temperatures needed for efficient power production, spectral selectivity is less important but still valuable, as the main requirement is then to maintain a high solar absorptance, while avoiding oxidation, inter-diffusion and undesirable chemical reactions. A stable substrate is also essential for achieving stable absorption.

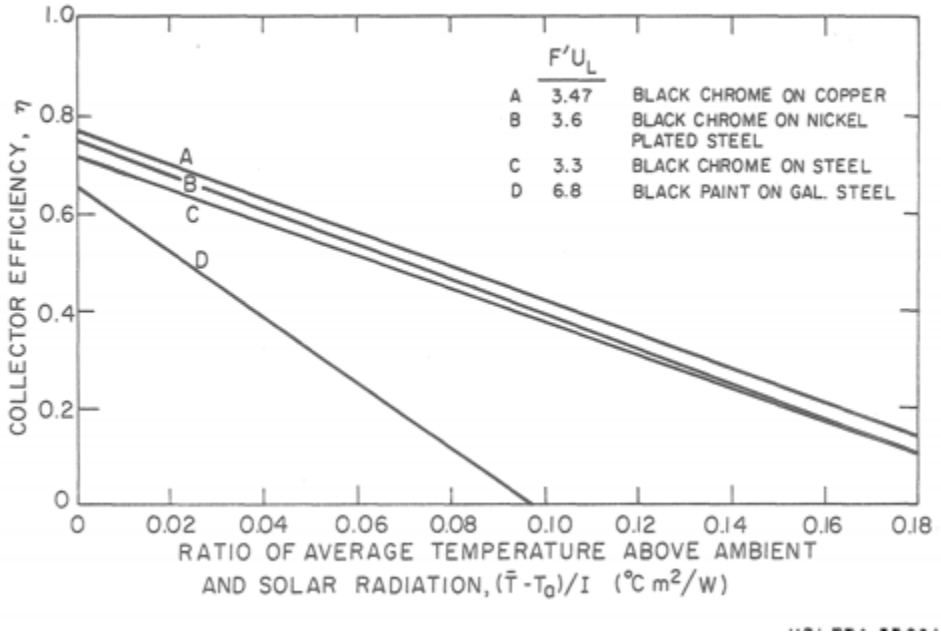

Figure 6.1 – Comparative efficiency plots for absorber surfaces using different reflectors. F' and U_L are the collector performance and heat loss coefficients [14].

The theoretical infrared reflectance of the metals as predicted by basic Drude theory compared to the real reflectance values of the metal derived from lab experiments often differ. In this study WVASE software was used to build a theoretical model of the SSC using the library of optical constants from Palik [15]. An example of W metal and its reflectance values provided theoretically and from experiment in this study is provided in Figure 6.2. As observed from Figure 6.2, there is a striking difference in the reflectance spectra. The experiment shows that the W deposited in the lab is less reflective than expected. This is very likely caused by a higher resistivity of the metal deposit, possibly due to a lower degree of crystallinity of the sputtered W. At the atomic level this can be understood as a decreased mean free path of the carriers from an increased number of electronic collusions with lattice imperfections [136]. The lower degree of crystallinity in the sputtered product is controlled by the deposition conditions, including factors such as degree of vacuum, substrate temperature, current, sputter gas pressure etc.

One of the ways to increase reflectivity is by polishing a surface of the metal, thus, decreasing the number of pores and nano-roughness which had caused both diffuse reflectivity and higher absorptance. This is a time consuming and not very practical option. Other solutions include changing the deposition parameters during metal

deposition or possibly fixing the deposition conditions but varying the element deposited in order to select the most IR reflective metal.

For annealing up to 500ºC for the Au/$AuAl_2$:AlN stack studied in Chapter 5, an Al-base reflector was chosen due it yielding a high and stable value of solar absorptance and an IR reflectance of ~98%. This was superior to other substrate metals trialed such as W or Ta. For other stacks that were intended for service above 500ºC the task was to find another metal for use in the base reflector that would be both temperature-resistant and have reasonably high IR reflectance. One of the challenges was to predict and prevent possible diffusion of the base metal layer into the supporting substrate at higher temperatures. A Si substrate was used due to its suitability for performing both optical measurements and annealing tests. Several metals were then excluded from these experiments as IR reflector candidates due to reaction with Si. For example, W and Cr, which are known to form WSi_2 and $CrSi_2$ at 650ºC and 400ºC, respectively [137, 138], were rejected.

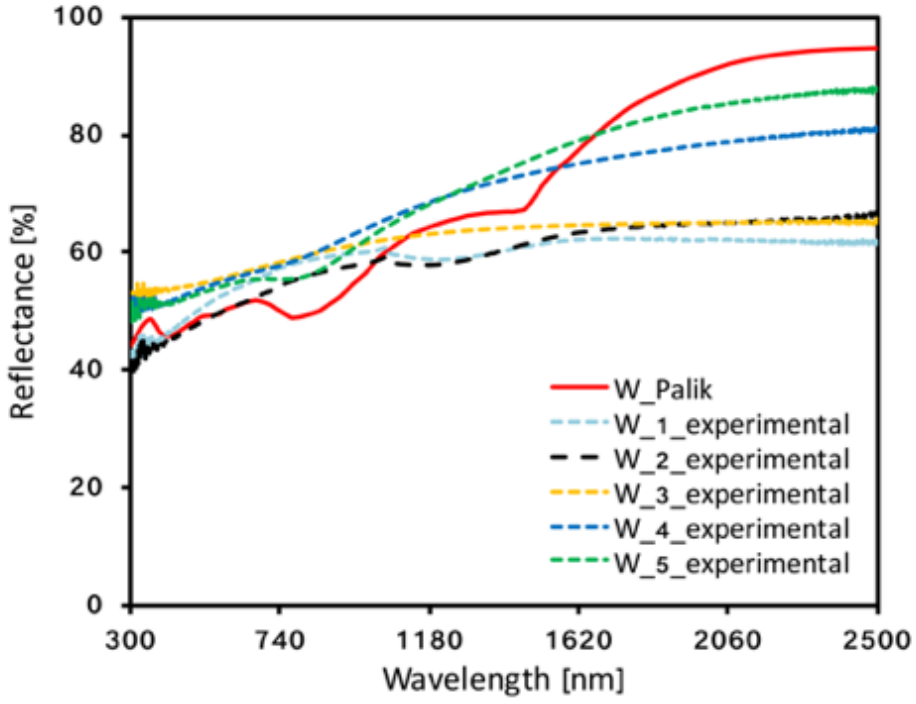

Figure 6.2 – Reflectance spectra for the W metal deposited in the lab using parameters from Table 6.1 vs library data obtained by Palik [15]

Table 6.1 – Influence of deposition conditions of W thin films on reflectance at 2500 nm compared to the modeled value using Palik data (W_Palik) of 95%.

Sample	Target current, A	Ar pressure, mTorr	Vacuum pressure	Deposition time, mins	Heater power, Watts	Max reflectivity at 2500 nm
W_Palik	-	-	-	-	-	**94.9%**
W_1	0.15	4×10^{-4}	7.7×10^{-6}	5	200	**61.7%**
W_2	0.25	1.4×10^{-3}	3.4×10^{-5}	5	215	**66.0%**
W_3	0.25	1.4×10^{-3}	3×10^{-5}	5	140	**65.0%**
W_4	0.25	1.4×10^{-3}	3.4×10^{-6}	10	215	**80.5%**
W_5	**0.25**	**1.4×10^{-3}**	**2.8×10^{-6}**	**10**	**215**	**88.0%**

Hence, other refractory d-metals were considered for high IR reflectivity including Ta, Pt, Ru, Mo and the alloys RuAl and Al-V.

The idea was to select a metal with both the highest $dR/d\lambda$ ramp-up in reflectivity and a high value at 2500 nm. As shown in Figure 16, an ideal SSC would be 100% reflective in the wavelength range starting from 2500 nm. In an ideal deposition of a SSC, the metallic back-reflecting material should be the same as the metal particles incorporated in the composite upper layer of the selective absorber in order to simplify the sputtering process as then replacing the targets is not required in between sputtering steps. This would be especially helpful in an industrial environment. However, this is not always the feasible due to various reasons, such as a reaction between the metal reflector and the substrate if heated during deposition, or difference in reflectance values of the deposited metallic films due to the kinetics of the sputtering process. For example, as has been shown by Rinnerbauer [126], an increase in deposition rate of a Ta thin film by a factor of two results in a reduced emissivity due to a formation of a denser structure.

In the current research, most of the reflectors were deposited using DC magnetron sputtering and a few (Ta_1, Ta_2, Mo, Table 6.2) were deposited in a separate chamber using RF sputtering. Although, RF is not a common practice for sputtering metallic materials, there has been scientific interest in the investigation of the structure and properties of the metals using this method and reported thin films were similar in quality to DC sputtered materials [139-142].

Figure 6.3 shows the reflectivity spectra of the range of the deposited metals. The least reflective metals were Ta_1, Ta_2 and Mo deposited using RF sputtering. The reflectance is affected by the different conditions of RF compared to DC sputtering.

Lower sputtering yield of metals using RF compared to DC is one possibility but it would require a separate investigation to fully investigate these issues. RuAl and V-Al yielded moderate reflectance of between 55% and 65% at 2500 nm. The alloying of V and Ru with Al was done for two reasons. The first was to use the increase in reflectivity of V and Ru by alloying them with the more conductive Al metal. As has been shown by Howell, RuAl alloys have a very low resistivity 19.3 $\mu\Omega$cm even after 1100°C annealing [143]. The second reason is to reduce surface roughness. It was shown that an alloy of aluminium and a transition metal is a good way of reducing the root mean square roughness to obtain a smoother and more reflective metallic surface [144]. It was demonstrated by Kylner by alloying Al and Cu, that reduced roughness by nearly 8Å occurred as a result of smaller grain size [144]. In the current work alloying of Ru with Al did increase reflectivity by 5% leading to 65% at 2500nm, however this is not high enough for an ideal spectrally selective solar absorber. The highest value of reflectance at 2500 nm was achieved by deposition of unalloyed Pt and Ta at conditions to be discussed later.

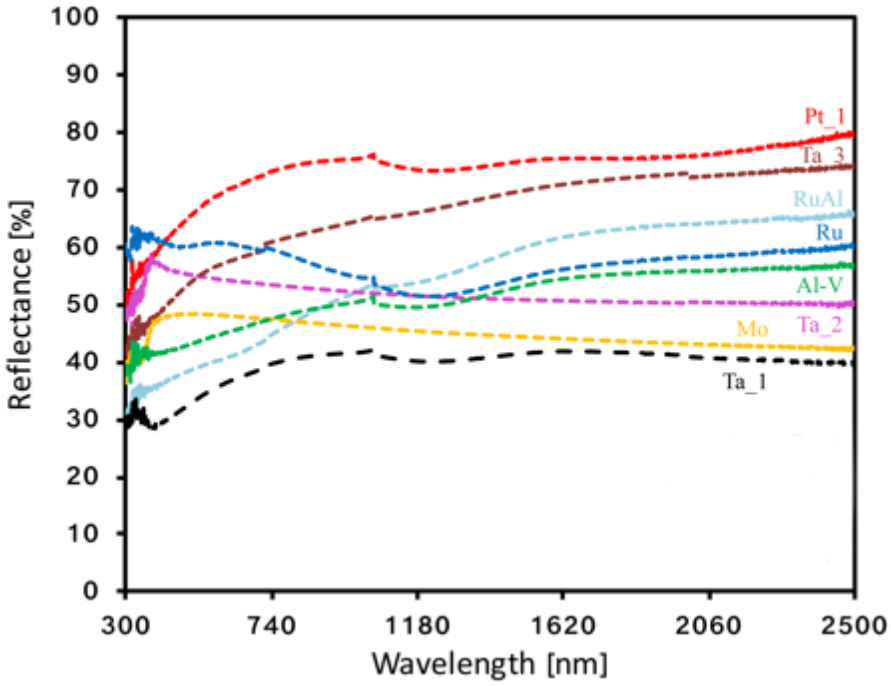

Figure 6.3 - Reflectance spectra for the Ta, Pt, Ru, Mo and RuAl, AlV thin films deposited using parameters in Table 6.2.

Table 6.2 - Deposition conditions of the metallic thin films using DC or RF sputtering

Sample	DC Current (A) or RF power (W)	Ar pressure, Torr	Vacuum pressure, Torr	Deposition time, mins	Heater power, Watts	Max reflectivity at 2500 nm
Pt_1	0.15(A)	1.3×10^{-3}	1.4×10^{-6}	12	-	79.8%
Ta_1	80(W)	2×10^{-3}	3.4×10^{-5}	15	-	39.9%
Ta_2	40(W)	2×10^{-3}	3.4×10^{-5}	6	-	50.1%
Ta_3	0.25(A)	1.4×10^{-3}	1.7×10^{-6}	8	-	74.2%
Ru	0.065(A)	1.3×10^{-3}	4×10^{-6}	10	-	60.2%
RuAl	0.196 (Ru)/0.25 (Al) (A)	1.4×10^{-3}	1.4×10^{-5}	5	200	65.4%
Al-V	0.196 (Ru)/0.25 (Al) (A)	1.4×10^{-3}	2.1×10^{-5}	5	200	56.8%
Mo	100 (W)	2	2×10^{-5}	20	-	42.5%

Both Pt and Ta thin films sputtered at a lower base pressure showed higher reflectance. This was also true for the W thin films of Table 6.1. Similar observations were made in Bennett's and Gelin's work for Al and Ni, Cu, V alloys respectively [145, 146]. As expected, the most reflective Al samples in Bennett's research were obtained in an ultra-high vacuum, followed by high-vacuum conditions, while Gelin showed that the reflectance of different types of alloys or pure metals might be insensitive to sputter power or Ar pressure, but is always affected by the vacuum pressure [145, 146]. This is due to higher directionality of the sputtered particles at higher vacuum, and the presence of less impurity particles that can deposit into a growing thin film during the sputtering process. The metallic film then has higher density. Another attempt (Table 6.3) to increase spectral reflectivity of Pt thin films was by heating the substrate,. This was done in order to trigger the formation of more highly crystalline phases, which ideally would have less defects and hence less scattering centres for the free carriers in the metallic layer. However, as observed in Figure 6.4, heating the substrate during deposition of the Pt_4 and Pt_5 samples did not lead to significant changes in spectral reflectance, instead, the lowest value of reflectance was observed for the Pt_4 sample. This might be attributed to the slower sputtering rate due to the desorption of gasses accumulated on the substrate holder or chamber walls when substrate heating is used, which also affects the level of vacuum as in Table 6.3. This highlights the importance of a low base pressure in the vacuum

chamber. For sample Pt_1, a faster sputtering rate was observed, which led to crystallization throughout the thin film growth taking on a random character, without any specific localization of the crystalline centres [147]. In the present work, this was also observed for the W films of Table 6.1, where heating of the substrate along with preservation of a good vacuum enabled achievement of highly reflective W films (~88%).

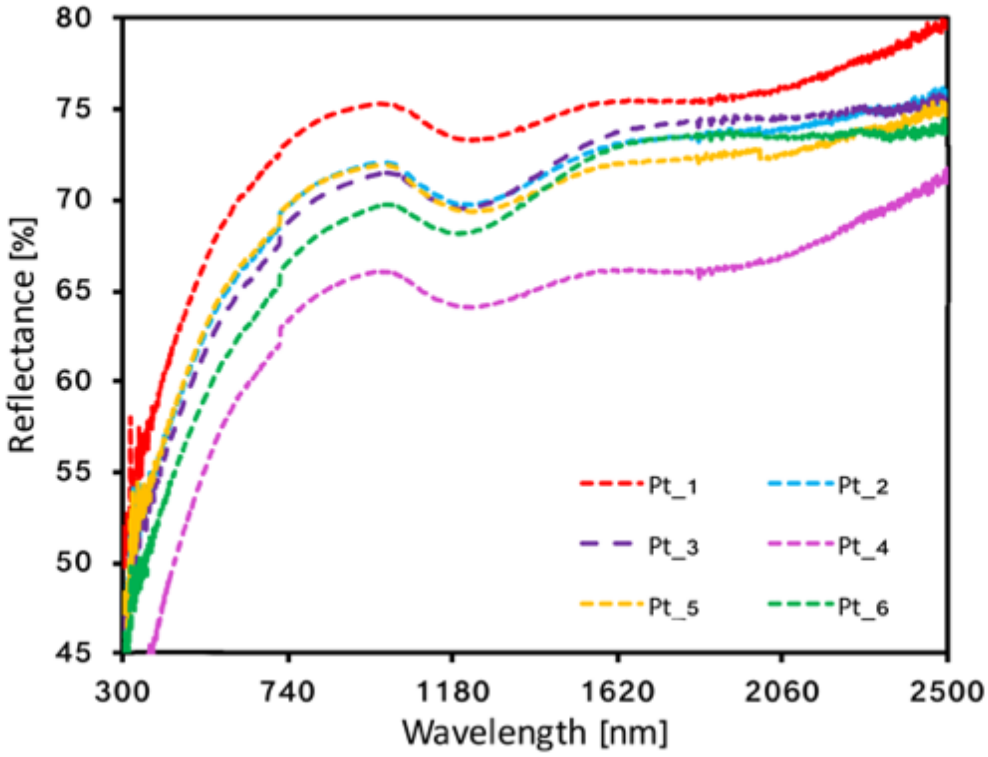

Figure 6.4 – Evolution of reflectivity of Pt thin films with the changing in deposition parameters of Table 6.2.

Hence, it can be concluded that the base pressure is a very important parameter in achieving high reflectance (and hence low emittance) for all metals and their alloys. The research conducted also showed that reaching a high value of reflectance at 2500 nm is achievable at the applied sputtering conditions without employing ultra-high vacuum. The implication of this is that our laboratory parameters can be easily transferred to large, industrial scale deposition.

Table 6.3 - Deposition conditions of the Pt thin films

Sample	Target current, A	Ar pressure, mTorr	Base pressure in the chamber before sputtering	Deposition time, mins	Heater power, Watts	Max reflectivity at 2500 nm
Pt_1	0.15(A)	1.3×10^{-3}	1.4×10^{-6}	12	-	**79.8%**
Pt_2	0.25	1.3×10^{-3}	3.6×10^{-6}	5	-	**76%**
Pt_3	0.15	0.4×10^{-3}	3.2×10^{-5}	5	-	**75.4%**
Pt_4	0.15	1.5×10^{-4}	1.1×10^{-5}	5	230	**71.3%**
Pt_5	0.25	1.4×10^{-3}	2.8×10^{-6}	10	215	**75.2%**
Pt_6	**0.15**	**4×10^{-4}**	**3.2×10^{-6}**	**5**	**-**	**74.4%**

Chapter 7

Conclusions and outlook

The current thesis has addressed issues related to the enhancement of photo-thermal conversion through using advanced spectrally-selective solar absorbing materials in high temperature concentrated solar power applications, with the main focus on the parabolic trough solar power plants and possible extension to STPV or solar thermo-electrics. There are still a few challenges remaining in these areas preventing achievement of maximum efficiency for these systems, which can be gained through pushing the limit of the current operating temperatures above 500ºC, with an ideal operating temperature of 630ºC for concentrated parabolic trough collectors (CPTC), and above 800ºC for STPV. Both strategies rely on the retaining the functionality of the solar absorbing surface at the higher temperatures. The main challenge includes achieving both structural integrity and excellent spectrally-selective response when exposed to a high temperature treatment. One of the approaches is to investigate new structures and designs containing refractory and/or noble metals within a thermally stable matrix. In the current work new cermet-based structures were proposed, optically designed and produced, including Al/AlN/Au-$AuAl_2$:AlN/AlN/SiO_2, Al/AlN/Au-$AuAl_2$:AlN/AlN/Au-$AuAl_2$:AlN/AlN/SiO_2, Pt/AlN/TiAlN/AlN/SiO_2, Pt/Ta:SiO_2/Ta:SiO_2/SiO_2, and Ta/Ta:SiO_2/Ta:SiO_2/SiO_2 which all achieved the main goals. In addition, a composite-based system Pt/Ta:SiO_2/Ta:SiO_2/SiO_2 with excellent spectrally selective properties was made and it had even higher temperature thermal stability, up to 1000ºC. While manufacturing of the stacks was realized using magnetron sputtering technique, other scalable approaches can be also utilized, such as newly appeared flame spray pyrolysis. This is especially useful for the production of the Au based stacks.

The first solar absorbing surface employed Au nanoparticles enclosed within a refractory AlN matrix as a part of the cermet-based design. Gold was selected due to its known strong oxidation resistant properties, which many other metals lack and thus they suffer rapid oxidation during a high temperature treatment. However, to date, the exploitation of the noble metal cermet-based spectrally selective coatings has been limited for high temperature CSP applications due to a rapid degradation of the absorber as a result of the Au NP's agglomeration after diffusion. A novel approach to stability was taken by alloying the Au NPs with another metal, which most importantly, should

not necessarily be a refractory metal. A remarkably high solar absorptance of 97% was achieved in one of the Au/$AuAl_2$:AlN-based stacks due to the simultaneous implementation of four separate mechanisms; thin film interference across one cermet layer, when it is sandwiched between two AlN dielectric layers, the absorption mechanism associated with the inter-band transitions in the final $AuAl_2$ metallic nanoparticles, a surface plasmon resonance when metallic NPs are placed into a dielectric host and, finally, an additional front surface reflectance reduction by the deposition of two AR coatings comprised of AlN and SiO_2. Another cermet-based stack used a more simple approach with a single Au/$AuAl_2$:AlN solar absorbing layer and two AR coatings resulting in the high solar absorptance of 92%. Both stacks used Al as the base IR reflector securing low thermal emittance and another additional and important function – stabilization of the Au nanoparticles present in the AlN matrix by formation of a more structurally and optically stable $AuAl_2$ bimetallic compound upon annealing. This resulted from a thermally-activated upward diffusion of Al atomic species into the neighboring cermet layer separated by the thin 8 nm AlN layer from the Al substrate, which occurred at 250ºC. High temperature ellipsometry showed that, at this temperature, the diffused Al atomic species would chemically combine with the Au NPs present in the AlN host and finalize the reaction at around 480ºC, when all the Au NPs had formed new and more optically and thermally stable $AuAl_2$ NPs. This, in its turn, has resulted in the beneficial boost of the solar absorptance in the single cermet stack by 3%, achieving 95% compared to its initial 92%, which is highly desirable if used in high concentration solar thermal applications as a small increase in α_s contributes to more efficient heat conversion by around 1%, compared to a small emittance reduction. This is attributed to the role of the weighting factor in a photo-thermal conversion containing the optical geometrical parameter, the concentration factor, showing that the efficiency of the heat conversion is much more dependent on the solar absorptance at higher concentration ratios, depending also on the operating temperature. For the double cermet stack, a slight reduction in solar absorptance was observed from 97% to 94%, which is attributed to the disruption of the optical interference in each cermet layer due to modified optical constants and thickness change of the bottom cermet layer, which was supported by the shift in the interference peak in the reflectance spectra. To avoid this, and to stabilize α_s at higher temperatures, the formation of the $AuAl_2$ nanoparticles in the upper cermet layer should be achieved. This can be accomplished by decreasing the thickness of the AlN chemical barrier layer between the two cermet layers, thus, weakening the barrier properties of the intermediate

AlN barrier layer and enabling Al diffusion from the back reflector through the first cermet layer and then through the thin AlN barrier layer. Both solar absorbers preserved low thermal emittance after annealing at 500ºC in vacuum, showing a consistently high spectrally selective response with ε_{82^oC} =0.13 (single cermet design) and ε_{82^oC}=0.21 (double cermet design). With these results in mind, the Au/$AuAl_2$:AlN single cermet solar absorber was selected for high temperature annealing at 500ºC for 168 hours in vacuum to test its long-term temperature stability. The stack showed no change in the optical and structural response and proved to be stable if annealed for one week. Of course, the designed single and double cermet SSCs need to be tested over longer times at well above 500ºC to fully simulate the service conditions. In all cases, the use of highly reflecting refractory metals as a base layer is desirable to prevent early degradation of the whole coating. This IR reflecting layer must still contain Al to enable $AuAl_2$ formation in the cermets. It would be interesting in future to investigate other nanoparticle bimetallic alloys using refractory metals enclosed within stable high temperature dielectric hosts such as HfN, which has being already extensively applied as an AR layer for photonic structures for the STPV applications.

Another spectrally-selective stack that was developed in the present project used a semiconductor as the absorber. Here a single $Ti_xAl_{1-x}N$ semiconducting layer was deposited on the Pt IR reflector, pre-coated by a 22 nm thick AlN diffusion barrier on an SS substrate. This was selected to test the potential of this type of coating for use in concentrated solar power applications. Two additional AR coatings were deposited on top to increase impedance matching between the absorber and the vacuum or air above, and were comprised of AlN and SiO_2 layers. The Pt IR base reflector was selected due to its high temperature stability and oxidation resistance properties. The selection of the $Ti_xAl_{1-x}N$ was made due to its solid diffusion barrier properties, high thermostability and the ability to adjust the Ti/Al ratio. Changing the Ti/Al ratio enabled wide tuning of the semiconductor optical response by a mix of transition \ metal-like and insulator-like behavior. Hence, Ti/Al ratio was carefully selected to enhance the overall optical performance of the stack. The theoretical model built using *n, k* of each single deposited $Ti_xAl_{1-x}N$ layer showed that the stack can achieve a solar absorptance of up to 95.6% with a designed cut-off at 2000 nm if used at 630ºC. The experimentally fabricated stack exhibited solar absorptance of 92%, which is still high. This difference between theory and experiment was attributed to a higher level of vacuum achieved during the sputtering process of the multilayer coating compared to the shorter time to deposit a single layer.

This lower pressure resulted in the greater directionality of the sputtered metallic species leading to a more reflective behavior in the near-IR solar spectral range. The initial emittance was 0.04. The magnetron sputtered $Ti_xAl_{1-x}N$ based solar absorber was annealed in vacuum up to 900ºC. Annealing for 24 hours was conducted at 600ºC, 700ºC, 750ºC and 800ºC, for 2 hours at 800ºC and for 3 hours at 900ºC. Despite some structural modifications of the main absorbing $Ti_xAl_{1-x}N$ layer during each stage of heat treatment up to 900ºC, the semiconductor based stack preserved its high solar absorptance, α_s = 92% with a minor increase in thermal emittance from its initial 0.04 to 0.15, which plays a secondary role if used in high concentration solar power applications where the concentration factor is *C*=100 (or more), resulting in 89% useful heat conversion efficiency at 630ºC. The diffusion of the Fe from the SS substrate was prevented by the AlN barrier layer, forming $FeN_{0.76}$ and showing that a diffusion barrier with only 22 nm thickness can decently perform its desired function.

Finally, two cermet-based stacks with the structure Pt/Ta:SiO_2/Ta:SiO_2/SiO_2 and Ta/Ta:SiO_2/Ta:SiO_2/SiO_2 were modelled and manufactured. These spectrally-selective solar absorbers were developed using a newly designed algorithm set up to achieve optimal spectrally selective response, with a minimum number of layers to avoid extra thermal stress generation during a high temperature heat treatment. This approach enabled achievement of a superior solar absorptance of 97.5% in both stacks with low initial thermal emittance $\varepsilon_{82ºC}$ =0.18 (on Pt) and $\varepsilon_{82ºC}$ =0.21 (on Ta). The multilayer absorbers were deposited on Si substrates pre-coated with Pt and Ta IR reflectors which were selected due to their high thermal stability and lower degree of chemical reaction with the Si when heated compared to other metals such as W, Mo or Ni, which form alloys with the Si already at 400ºC or 550ºC. The two stacks were identical apart from the IR reflectors used. The heart of these solar absorbers was a double cermet with the two different volume densities of Ta particle inclusions (24 vol% and 45 vol%) in the SiO_2 dielectric matrix. The Ta particles perform a double solar absorbing function while creating an index gradient throughout the coating by means of an increase in the refractive index from the top surface represented by the AR SiO_2 layer down to the substrate.

The stacks were heated up cyclically in vacuum up 1100ºC for 1 hour for each temperature treatment. The XRD data showed that there was an alloying of the Ta NPs with the atomic species thermally diffused from the back reflectors, Pt and Ta. In case of the Pt it led to the formation of the bimetallic nanoparticles composed of the Pt and Ta. The stack on the Pt back reflector proved to be more stable due to the lack of reaction of

the Pt with the Si, while in case of the Ta this reaction happens rapidly at 1000ºC, but for the Pt not until 1100ºC. An ellipsometric model was designed to fit the measured parameters and hence define the thermally induced structural modifications through adjustment of the depolarization factor in the top layer, the amount of the Ta present, and the possible additional inclusions in the bottom cermet layer as a result of the Ta or Pt diffusion from the back reflector. Two layers were designed using Maxwell-Garnett EMA approach for the top cermet layer and a Bruggeman EMA approach for the bottom layer. The model showed that the amount of the Ta within the low metal volume fraction (LMVF) cermet does not change, but it predicts that the Ta undergoes a slight modification in its shape, becoming more spherical- in order to reduce surface energy from its initial elongated shape when heated up to 1000ºC. For the bottom cermet layer the volume density of additional Pt or Ta varied between 0.45 vol% after 600ºC annealing to 9.5 vol% after 1000ºC, and between 0.28 vol% after 600ºC annealing to 5.38 vol% after 900ºC, respectively confirming the XRD results. The SEM cross-sectional pictures showed that the layers remained distinguishable preserving clear boundaries without any structural degradation up to 1000ºC for the Ta:SiO_2 based stack using the Pt IR reflector. The solar absorptance and emittance were calculated and measured after each cycle of the heat treatment showing increase in solar absorptance up to 98.4% at 800ºC due to an increased metallic fraction in the bottom cermet layer creating optimal values of *n,k* for this layer. At the same time, the thermal emittance kept decreasing in both stacks due to recrystallization of the metallic base reflectors leading to $\varepsilon_{82^oC} = 0.15$ (Pt) and $\varepsilon_{82^oC} = 0.04$ (Ta), which is beneficial in order to reduce heat loss by radiation. Hence, an improvement in optical response was observed in both stacks up to 900ºC with the final $\alpha_s/\varepsilon_{82^oC} = 6.5$ (on Pt) and $\alpha_s/\varepsilon_{82^oC} = 24$ (on Ta). The annealing of the Ta:SiO_2 based solar absorber on Pt at 1000ºC shows minor reduction in solar absorptance to 94.9%, which is still good enough to gain a high degree of useful heat conversion. The results obtained for the Ta:SiO_2 cermet-based SSCs designed in the present project suggest that these may be able to retain solar selective absorptance of 0.95 while operating at ultra-high temperatures of 1000ºC with a high level of spectral selectivity. This would provide a very competitive advantage compared to the coatings currently in commercial use. The initial solar absorptance of this stack can be further improved and future work could be devoted to the deposition of the porous SiO_2 or tilted structures in order to create a higher degree of impedance matching between the SiO_2 AR layer and the vacuum. Optical modelling

suggests that it would be possible to create a nearly absolutely black surface at solar wavelengths, with a solar absorptance of 99.5%.

Finally, the results of this project show that significant improvements in the performance spectrally-selective, solar absorbing surfaces are still possible. This bodes well for future development of solar-to-heat conversion as well as to future solar thermal photovoltaic applications.

Appendix

Appendix 1

Symbols

α_s	integrated solar absorptance
Γ	damping factor containing a drift velocity of the electrons and describes the number of collisions of free electrons per second when accelerated by the optical electric field
δ	phase of light
Δ	shift in the phase of polarized light after reflection from the sample
ε	hemispherical emittance
ε_1	real part of the complex dielectric constant
ε_2	imaginary parts of the complex dielectric constant
ε_∞	dielectric constant responsible for residual absorption above the frequency where ε_1 becomes negative
η_e	efficiency of the steam engine,
η	efficiency of heat generation
λ	wavelength
λ_0	wavelength of the incident light
λ_{lim}	boundary value of the wavelength which is sufficient to excite electrons with an absorption of the electromagnetic wave
π	constant

Ψ	amplitude of the polarized light after reflection from the sample
$\boldsymbol{\omega_p}$	resonance (plasma) frequency at which $\boldsymbol{\varepsilon_1 \rightarrow 0}$ and $\boldsymbol{\varepsilon_2 < 1}$
$\boldsymbol{\omega}$	angular frequency of the incident electromagnetic wave
$\boldsymbol{A_n}$	Drude oscillator strength related to plasma frequency
B	amount of energy emitted by a BB as a function of wavelength ($\boldsymbol{\lambda}$)
$\boldsymbol{Br_n}$	oscillator broadness
c	speed of light in a medium
f	frequency of light
h	Planck's constant
k	imaginary part of the complex refractive index (extinction coefficient)
I_a	intensity of absorbed light
I_i	intensity of incident light
$I(x)$	intensity of light at the point x below the
$I(x_0)$	intensity of incident light surface of the material
I_r	intensity of reflected light
I_i	intensity of incident light.
I_t	intensity of transmitted light
k_B	Boltzmann's constant
m	complex refractive index
n	real part of the complex refractive index (refractive index)
S_1	the AM1.5 or one sun insolation

$\boldsymbol{S_{total}}$	total incident solar flux with C the solar concentration factor from the mirror –absorber optics
$\boldsymbol{P_{\lambda}(T)}$	black body radiation as a function of temperature
$\boldsymbol{t}$	thickness of a thin film
$\boldsymbol{T}$	absolute temperature of the BB
$T_{ambient}$	ambient temperature
$\boldsymbol{T_C}$	temperature of the reservoir where the heat is released to
$\boldsymbol{T_H}$	temperature of the heat source

Appendix 2

Abbreviations

AR	anti reflection
BB	black body
DC	direct current
DF	depolarization factor
EMA	effective medium approximation
HMVF	high metal volume fraction
HTF	heat transfer fluid
CPTC	concentrated parabolic trough collector
CSP	concentrated solar power
M-G	Maxwell-Garnett
LMVF	low metal volume fraction
LSPR	localized surface plasmon resonance
NPs	nanoparticles
OPD	optical dense path
PhC	photonic crystal

SEM	scanning electron microscopy
SS	stainless steel
STEG	solar thermoelectrics
SSC	spectrally selective coating
STPV	solar thermophotovoltaics
SSSA	spectrally selective solar absorber
SSSAC	spectrally selective solar absorbing coating
RF	radio frequency
TEM	transmission electron microscopy
XRD	X-ray diffraction

Appendix 3

Design and simulation of spectrally selective solar absorbing stacks

Designing and optimization of a stack that corresponds to a satisfied spectrally selective response in the solar and IR range requires a detailed approach and clearly outlined steps. This, in its turn, serves as a reliable prediction of optical behavior and secures efficient deposition of the stack, reducing time and effort spent on the single layer sputtering and unnecessary deposition steps. In the current thesis, WVASE software was employed to build spectrally selective stacks with the following essential input parameters:

1. Constructing a layer with the known **optical constants** (can be derived in two ways: by using library data and/or determined experimentally). In the current research both approaches were used and were specified in thesis where needed. Derivation of the optical constants from the ellipsometric measurements can be conducted in two ways: 1) by building a general oscillator layer, where a number of applicable for the current layer oscillators are added characterizing the light matter interaction and 2) by building a layer using effective medium approximation (EMA), the details of which are described in the thesis.

2. Using known optical constants **a stack is built** with the defined thickness and number of layers

3. The **optical response** is generated in 300 nm – 2500 nm range. The optical response can be extrapolated further to the mid- and far IR range to predict emittance value.

Once the model of the stack is constructed, the single layers are deposited and obtained experimental optical constants in the lab are compared to the library data. If the optical constants match, the whole stack is deposited, if not, then the individual layer parameters are readjusted to achieve a desired spectrally selective response.

Once the newly designed stack is deposited, it can be characterized using the following approach:

As it is shown in Figure 2.7, the stack is firstly measured by the ellipsometer, where ellipsometric parameters psi and delta are recorded. Then, the stack's model is built, as a rule, using the original model developed for the stack design. After this, the psi and delta data is generated by the software and compared to the experimental one. If the fit is not exact, then the stack's model is further optimized by starting with the thickness adjustment. If the thickness adjustment is not sufficient for a perfect fit, the n,k can be further readjusted for each layer by modifying the oscillator parameters or EMA layer (if used).

A perfect or nearly perfect fit of the generated data to the experimental data provide information on the stacks' structure, optical constants of individual layers, their thickness and uniformity. The further details on the ellipsometry data analysis can be found in WVASE manual [148].

Appendix 4

Supporting data

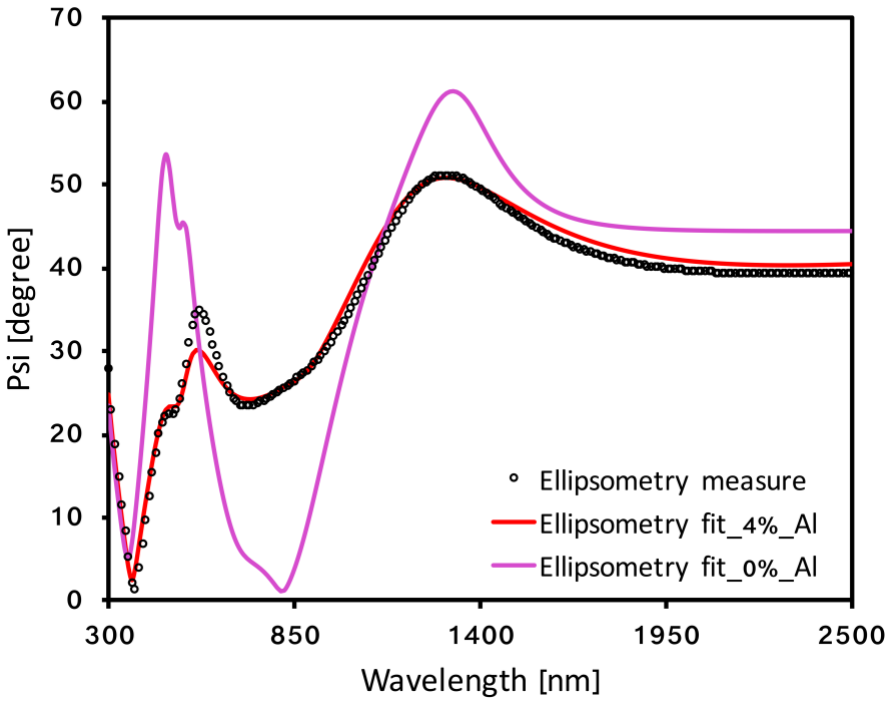

Figure A4.1 – The ellipsometric fit of the Au based stack (Chapter 3) with Al content in the AlN matrix and without

Bibliography

1. Randers, J., *2052: A global forecast for the next forty years*. 2012: Chelsea Green Publishing.
2. *2017 The World Bank, Solar resource data: Solargis*. https://solargis.com/.
3. Taylan, O. and H. Berberoglu, *Fuel production using concentrated solar energy*, in *Application of Solar Energy*. 2013, InTech.
4. Pitz-Paal, R. *Concentrating Solar Power Systems*. in *EPJ Web of Conferences*. 2017. EDP Sciences.
5. Lee, W.Y. and S.S. Kim, *Maximum power-conversion efficiency for the utilization of solar energy.* International Journal of Energy Research, 1991. **15**(4): p. 257-267.
6. Junovich, A.E. and M.V. Tchukichev, *Optical phenomena in semiconductors [In Russian]*. Moscow, 2007.
7. Cao, F., et al., *A review of cermet-based spectrally selective solar absorbers.* Energy & Environmental Science, 2014. **7**(5): p. 1615-1627.
8. Maaza, M., et al., *Surface-Interface Investigation and Stability of Cermet-Based Solar Absorbers by Grazing Angle X-Rays Reflectometry: Pt–Al 2 O 3 Case.* Arabian Journal for Science and Engineering, 2014. **39**(7): p. 5825-5846.
9. Selvakumar, N. and H.C. Barshilia, *Review of physical vapor deposited (PVD) spectrally selective coatings for mid-and high-temperature solar thermal applications.* Solar Energy Materials and Solar Cells, 2012. **98**: p. 1-23.
10. Weinstein, L.A., et al., *Concentrating solar power.* Chemical reviews, 2015. **115**(23): p. 12797-12838.
11. Bilokur, M., et al., *High Temperature Spectrally Selective Solar Absorbers Using Plasmonic AuAl2: AlN Nanoparticle Composites.* Solar RRL, 2017. **1**(10): p. 1700092.
12. *Ellipsometry Data Analysis*. Available from: http://www.jawoollam.com/ [cited 2018/09/10]

.

13. Tulchinsky, D., et al., *A novel non-selective coating material for solar thermal potential application formed by reaction between sol–gel titania and copper manganese spinel.* Solar Energy Materials and Solar Cells, 2014. **120**: p. 23-29.
14. Lampert, C.M., *A solar test collector for evaluation of both selective and non-selective absorbers.* International journal of energy research, 1987. **11**(3): p. 405-421.
15. Palik, E., *Handbook of Optical Constants of Solids (Academic, San Diego, 1998)*. Google Scholar: p. 597-602.
16. Coddington, O., et al., *A Solar Irradiance Climate Data Record.* Bulletin of the American Meteorological Society, 2016. **97**(7): p. 1265-1282.
17. Mercer, P., *Is Australia falling out of love with solar power.* BBC News, 2014.
18. Asif, M. and T. Muneer, *Energy supply, its demand and security issues for developed and emerging economies.* Renewable and Sustainable Energy Reviews, 2007. **11**(7): p. 1388-1413.
19. Kahia, M., M.S.B. Aïssa, and C. Lanouar, *Renewable and non-renewable energy use-economic growth nexus: The case of MENA Net Oil Importing Countries.* Renewable and Sustainable Energy Reviews, 2017. **71**: p. 127-140.

20. Johnston, W. and R. Egan, *National survey report of PV power applications in Australia 2015.* Report, Australian PV Institute (June 2016), 2017.
21. Price, H. and D. Kearney. *Reducing the cost of energy from parabolic trough solar power plants*. in *ASME 2003 International Solar Energy Conference*. 2003. American Society of Mechanical Engineers.
22. Rawlins, J. and M. Ashcroft, *Small-scale Concentrated Solar Power: A review of current activity and potential to accelerate deployment.* Carbon Trust, Stamford, London, 2013.
23. Padera, F., *Measuring absorptance (k) and refractive index (n) of thin films with the PerkinElmer Lambda 950/1050 high performance UV-Vis/NIR Spectrometers.* PerkinElmer Inc.: Application note: UV/Vis Spectroscopy, 2013: p. 43.
24. Hass, G., M.H. Francombe, and R.W. Hoffman, *Physics of thin films: advances in research and development*. 2013: Elsevier.
25. Pavlov, P.V. and A.F. Khokhlov, *Solid State Physics [in Russian]*. 2000: Novgorod State University.
26. Hahn, R. and B. Seraphin, *Spectrally selective surfaces for photothermal solar energy conversion.* Physics of thin films, 1978. **10**: p. 1-69.
27. Fahrenholtz, W.G., et al., *Refractory diborides of zirconium and hafnium.* Journal of the American Ceramic Society, 2007. **90**(5): p. 1347-1364.
28. Sun, Y., et al., *Microstructure, optical properties and thermal stability of ZrB2 and Zr–B–N thin films as high-temperature solar selective absorbers.* Materials Express, 2014. **4**(3): p. 205-212.
29. Sciti, D., et al., *Tantalum diboride-based ceramics for bulk solar absorbers.* Solar Energy Materials and Solar Cells, 2014. **130**: p. 208-216.
30. Sani, E., et al., *Porous and dense hafnium and zirconium ultra-high temperature ceramics for solar receivers.* Optical Materials, 2013. **36**(2): p. 163-168.
31. Sciti, D., et al., *Suitability of ultra-refractory diboride ceramics as absorbers for solar energy applications.* Solar Energy Materials and Solar Cells, 2013. **109**: p. 8-16.
32. Sani, E., et al., *Spectrally selective ultra-high temperature ceramic absorbers for high-temperature solar plants.* Journal of Renewable and Sustainable Energy, 2012. **4**(3): p. 033104.
33. Sani, E., et al., *Hafnium and tantalum carbides for high temperature solar receivers.* Journal of Renewable and Sustainable Energy, 2011. **3**(6): p. 063107.
34. Sani, E., et al., *Ultra-refractory ceramics for high-temperature solar absorbers.* Scripta Materialia, 2011. **65**(9): p. 775-778.
35. Seraphin, B.O., *Solar energy conversion: Solid-state physics aspects.* Solar Energy Conversion: Solid-state Physics Aspects, 1979.
36. Wu, Y., et al., *Colored solar selective absorbing coatings with metal Ti and dielectric AlN multilayer structure.* Solar Energy Materials and Solar Cells, 2013. **115**: p. 145-150.
37. Li, X.-F., et al., *High solar absorption of a multilayered thin film structure.* Optics Express, 2007. **15**(4): p. 1907-1912.
38. Zhou, W.-X., et al., *Nano-Cr-film-based solar selective absorber with high photo-thermal conversion efficiency and good thermal stability.* Optics Express, 2012. **20**(27): p. 28953-28962.
39. Thornton, J.A., A.S. Penfold, and J.L. Lamb, *Sputter-deposited Al2O3/Mo/Al2O3 selective absorber coatings.* Thin Solid Films, 1980. **72**(1): p. 101-110.

40. Valleti, K., D.M. Krishna, and S. Joshi, *Functional multi-layer nitride coatings for high temperature solar selective applications.* Solar Energy Materials and Solar Cells, 2014. **121**: p. 14-21.
41. Seraphin, B.O., *Chemical vapor deposition of thin semiconductor films for solar energy conversion.* Thin Solid Films, 1976. **39**: p. 87-94.
42. Lampert, C.M., *Coatings for enhanced photothermal energy collection I. Selective absorbers.* Solar Energy Materials, 1979. **1**(5-6): p. 319-341.
43. Thomas, L. and E. Chain, *Spectrally selective black tungsten films.* Thin solid films, 1983. **105**(3): p. 203-211.
44. Chain, E., G. Carver, and B. Seraphin, *Highly reflecting molybdenum thin films having significant solar absorptance.* Thin Solid Films, 1980. **72**(1): p. 59-64.
45. Lira-Cantu, M., et al., *Electrochemical deposition of black nickel solar absorber coatings on stainless steel AISI316L for thermal solar cells.* Solar energy materials and solar cells, 2005. **87**(1-4): p. 685-694.
46. Moon, J., et al., *High performance multi-scaled nanostructured spectrally selective coating for concentrating solar power.* Nano Energy, 2014. **8**: p. 238-246.
47. Kim, T.K., et al., *Tandem structured spectrally selective coating layer of copper oxide nanowires combined with cobalt oxide nanoparticles.* Nano Energy, 2015. **11**: p. 247-259.
48. Barshilia, H.C., S. John, and V. Mahajan, *Nanometric multi-scale rough, transparent and anti-reflective ZnO superhydrophobic coatings on high temperature solar absorber surfaces.* Solar Energy Materials and Solar Cells, 2012. **107**: p. 219-224.
49. Kennedy, C.E., *Review of mid-to high-temperature solar selective absorber materials*. Vol. 1617. 2002: National Renewable Energy Laboratory Golden, Colorado.
50. Wang, J., Z. Chen, and D. Li, *Simulation of two-dimensional Mo photonic crystal surface for high-temperature solar-selective absorber.* physica status solidi (a), 2010. **207**(8): p. 1988-1992.
51. Di Bartolo, B. and O. Forte, *Frontiers of optical spectroscopy: investigating extreme physical conditions with advanced optical techniques*. Vol. 168. 2006: Springer Science & Business Media.
52. Rinnerbauer, V., et al., *Metallic photonic crystal absorber-emitter for efficient spectral control in high-temperature solar thermophotovoltaics.* Advanced Energy Materials, 2014. **4**(12): p. 1400334.
53. Bermel, P., et al., *Selective solar absorbers.* Annual Review of Heat Transfer, 2012. **15**(15).
54. Hernández García, D., *Selective thermal emitters based on photonic crystals.* 2014.
55. Wang, C., et al., *High performance Al–AlN solar spectrally selective coatings with a self-assembled nanostructure AlN anti-reflective layer.* Journal of Materials Chemistry A, 2017. **5**(6): p. 2852-2860.
56. Zhang, Q.-C., et al., *Zr–ZrO2 cermet solar coatings designed by modelling calculations and deposited by dc magnetron sputtering.* Journal of Physics D: Applied Physics, 2003. **36**(6): p. 723.
57. Craighead, H., et al., *Graded-index Pt-Al2O3 composite solar absorbers.* Applied Physics Letters, 1981. **39**(1): p. 29-31.
58. Ritchie, I., et al., *Thermal degradation of chromium black solar selective absorbers.* Solar Energy Materials, 1979. **2**(2): p. 167-176.

59. Gesheva, K., E. Chain, and B. Seraphin, *Black molybdenum photothermal converter layers deposited by pyrolytic hydrogen reduction of MoO2Cl2.* Solar Energy Materials, 1980. **3**(3): p. 415-424.
60. Wang, J., et al., *Optical property and thermal stability of Mo/Mo–SiO2/SiO2 solar-selective coating prepared by magnetron sputtering.* physica status solidi (a), 2011. **208**(3): p. 664-667.
61. Zhang, Q.-C., *Direct current magnetron sputtered W–AlN cermet solar absorber films.* Journal of Vacuum Science & Technology A: Vacuum, Surfaces, and Films, 1997. **15**(6): p. 2842-2846.
62. Jyothi, J., et al., *Design and fabrication of spectrally selective TiAlC/TiAlCN/TiAlSiCN/TiAlSiCO/TiAlSiO tandem absorber for high-temperature solar thermal power applications.* Solar Energy Materials and Solar Cells, 2015. **140**: p. 209-216.
63. Cheng, J., et al., *Improvement of thermal stability in the solar selective absorbing Mo–Al2O3 coating.* Solar Energy Materials and Solar Cells, 2013. **109**: p. 204-208.
64. Antonaia, A., et al., *Stability of W-Al 2 O 3 cermet based solar coating for receiver tube operating at high temperature.* Solar Energy Materials and Solar Cells, 2010. **94**(10): p. 1604-1611.
65. Zhang, Q.C. and D.R. Mills, *Very low-emittance solar selective surfaces using new film structures.* Journal of applied physics, 1992. **72**(7): p. 3013-3021.
66. Fan, J.C. and P.M. Zavracky, *Selective black absorbers using MgO/Au cermet films.* Applied Physics Letters, 1976. **29**(8): p. 478-480.
67. Gusev, A.I. and A.A. Rempel′, *Nanocrystalline materials*. 2004: Cambridge Int Science Publishing.
68. Samsonov, G.V., *Nitrides*. 1970, FOREIGN TECHNOLOGY DIV WRIGHT-PATTERSON AFB OH.
69. Goldstein, J.I., et al., *Scanning electron microscopy and X-ray microanalysis*. 2017: Springer.
70. Williams, D.B. and C.B. Carter, *The transmission electron microscope*, in *Transmission electron microscopy*. 1996, Springer. p. 3-17.
71. Lvovsky, A.I., *Fresnel equations.* Encyclopedia of Optical Engineering, 2013: p. 1-6.
72. Fan, J.C.C. and P.M. Zavracky, *Selective black absorbers using MgO/Au cermet films.* Appl. Phys. Lett. 29, 478 (1976);, 1976. **29**(8): p. 478-480.
73. Gittleman, J.I., et al., *Optical properties and selective solar absorption of composite material films.* Thin Solid Films, 45 (1977) 1977. **45**: p. 9-18.
74. Dun, M., et al., *Microstructure and thermal stability of Al/Ti0.5Al0.5N/Ti0.25Al0.75N/AlN solar selective coating.* Solar Energy Mater. Solar Cells, 2013. **111**: p. 49–56.
75. Zhang, Q.C. and D.R. Mills, *Very low-emittance solar selective surfaces using new film structures.* J. Appl. Phys., 1992. **72**: p. 3013-3021.
76. Cao, F., et al., *Enhanced Thermal Stability of W-Ni-Al2O3 Cermet-Based Spectrally Selective Solar Absorbers with Tungsten Infrared Reflectors.* Advanced Energy Materials, 2015. **5**(2).
77. Zhang, K., et al., *A review on thermal stability and high temperature induced ageing mechanisms of solar absorber coatings.* Renewable and Sustainable Energy Reviews, 2017. **67**: p. 1282-1299.

78. Gao, J., et al., *Plasmonic AgAl Bimetallic Alloy Nanoparticle/Al2O3 Nanocermet Thin Films with Robust Thermal Stability for Solar Thermal Applications.* Advanced Materials Interfaces, 2016. **3**(16).
79. Nyberg, G.A. and R. Buhrman, *Macroscopic surface roughness in metal-dielectric composite films: photothermal absorber applications.* APpl. Phys. Lett., 1982. **40**: p. 129-131.
80. Xu, X., T. Gibbons, and M.B. Cortie, *Spectrally-selective gold nanorod coatings for window glass.* Gold Bull., 2006. **39**(4): p. 156-165.
81. Hahn, R.E. and B.O. Seraphin, *Spectrally selective surfaces for photothermal solar energy conversion.* Physics of Thin Films, 1978. **10**: p. 1-69.
82. Berthier, S. and J. Lafait, *Optical properties of Au-MgO cermet thin films: Percolation threshold and grain size effect*

. Thin Solid Films, 1982. **89**: p. 213-220.
83. Supansomboon, S., et al., *Thin films of PtAl 2 and AuAl 2 by solid-state reactive synthesis.* Thin Solid Films, 2015. **589**: p. 805-812.
84. Himpel, G., M. Herrmann, and S. Höhn, *Comparison of the high-temperature corrosion of aluminium nitride, alumina, magnesia and zirconia ceramics by coal ashes.* Ceramics International, 2015. **41**(7): p. 8288-8298.
85. Thornton, J.A. and J.L. Lamb, *Sputter-deposited Pt-Al2O3 selective absorber coatings.* Thin Solid Films, 1981. **83**(4): p. 377-385.
86. Barshilia, H.C., et al., *Structure and optical properties of Ag–Al 2 O 3 nanocermet solar selective coatings prepared using unbalanced magnetron sputtering.* Solar Energy Materials and Solar Cells, 2011. **95**(7): p. 1707-1715.
87. Koledintseva, M.Y., R.E. DuBroff, and R.W. Schwartz, *A Maxwell Garnett model for dielectric mixtures containing conducting particles at optical frequencies.* Progress In Electromagnetics Research, 2006. **63**: p. 223-242.
88. Supansomboon, S., A. Maaroof, and M. Cortie, *Purple glory": the optical properties and technology of AuAl2 coatings.* Gold Bull, 2008. **41**(4): p. 296-304.
89. Egami, T., K. Maeda, and V. Vitek, *Structural defects in amorphous solids A computer simulation study.* Philosophical Magazine A, 1980. **41**(6): p. 883-901.
90. Dean, J.A. and N.A. Lange, *Thermodynamic properties.* Lange's Handbook of Chemistry, 1999: p. 6.90-6.104.
91. Malgas, G.F., et al., *Investigation of the effects of different annealing ambients on Ag/Al bilayers: Electrical properties and morphology.* Journal of Applied Physics, 2001. **90**(11): p. 5591-5598.
92. Fan, H.J., et al., *Influence of surface diffusion on the formation of hollow nanostructures induced by the Kirkendall effect: the basic concept.* Nano letters, 2007. **7**(4): p. 993-997.
93. Keast, V., et al., *The effect of vacancies on the optical properties of AuAl2.* Journal of Physics: Condensed Matter, 2015. **27**(50): p. 505501.
94. Odeh, S.D. and H.I. Abu-Mulaweh, *Design and development of an educational solar tracking parabolic trough collector system.* Global journal of engineering education, 2013. **15**(1).
95. Wang, J., et al., *Performance Simulation Comparison for Parabolic Trough Solar Collectors in China.* International Journal of Photoenergy, 2016. **2016**.
96. Zheng, L., et al., *Angular solar absorptance and thermal stability of Mo–SiO 2 double cermet solar selective absorber coating.* Solar Energy, 2015. **115**: p. 341-346.

97. Tesfamichael, T. and E. Wäckelgård, *Angular solar absorptance and incident angle modifier of selective absorbers for solar thermal collectors.* Solar Energy, 2000. **68**(4): p. 335-341.
98. Kats, M.A., et al., *Nanometre optical coatings based on strong interference effects in highly absorbing media.* Nature materials, 2013. **12**(1): p. 20-24.
99. Galli, E., et al., Active Passive Electronic Components, 1980. **6**: p. 147.
100. Supansomboon, S., et al., *Thin films of $PtAl_2$ and $AuAl_2$ by solid-state reactive synthesis.* Thin Solid Films, 2015: p. 905-812.
101. Malgas, G.F., et al., *Investigation of the effects of different annealing ambients on Ag/Al bilayers: Electrical properties and morphology.* J. Appl. Phys., 2001. **90**: p. 5591-5598.
102. Sathiaraj, T.S., et al., Thin Solid Films, 1990. **190**: p. 241-**.
103. El Gharbi, N., et al., *A comparative study between parabolic trough collector and linear Fresnel reflector technologies.* Energy Procedia, 2011. **6**: p. 565-572.
104. Cao, F., et al., *A review of cermet-based spectrally selective solar absorbers.* Energy Environ. Sci., 2014. **7**: p. 1615-1627.
105. Du, M., et al., *Microstructure and thermal stability of Al/Ti0. 5Al0. 5N/Ti0. 25Al0. 75N/AlN solar selective coating.* Solar Energy Materials and Solar Cells, 2013. **111**: p. 49-56.
106. Feng, J., et al., *The spectral selective absorbing characteristics and thermal stability of SS/TiAlN/TiAlSiN/Si3N4 tandem absorber prepared by magnetron sputtering.* Solar Energy, 2015. **111**: p. 350-356.
107. Gao, X.-H., et al., *Enhanced optical properties of TiN-based spectrally selective solar absorbers deposited at a high substrate temperature.* Solar Energy Materials and Solar Cells, 2017. **163**: p. 91-97.
108. Soum-Glaude, A., et al., *Optical characterization of TiAlNx/TiAlNy/Al2O3 tandem solar selective absorber coatings.* Solar Energy Materials and Solar Cells, 2017. **170**: p. 254-262.
109. Liu, Y., C. Wang, and Y. Xue, *The spectral properties and thermal stability of NbTiON solar selective absorbing coating.* Solar Energy Materials and Solar Cells, 2012. **96**: p. 131-136.
110. Höglund, C., et al., *Effects of volume mismatch and electronic structure on the decomposition of ScAlN and TiAlN solid solutions.* Physical Review B, 2010. **81**(22): p. 224101.
111. Suh, C.-M., B.-W. Hwang, and R.-I. Murakami, *Behaviors of residual stress and high-temperature fatigue life in ceramic coatings produced by PVD.* Materials Science and Engineering: A, 2003. **343**(1-2): p. 1-7.
112. Roos, J., et al., *Interrelationship between processing, coatingproperties and functional properties of steered arc physically vapour deposited (Ti, AI) N and (Ti, Nb) N coatings.* Thin Solid Films, 1990. **193**: p. 547-556.
113. Münz, W.D., *Titanium aluminum nitride films: A new alternative to TiN coatings.* Journal of Vacuum Science & Technology A: Vacuum, Surfaces, and Films, 1986. **4**(6): p. 2717-2725.
114. Man, B., et al., *Microstructure, oxidation and H2-permeation resistance of TiAlN films deposited by DC magnetron sputtering technique.* Surface and Coatings Technology, 2004. **180**: p. 9-14.
115. Abrikosov, I.A., et al., *Phase stability and elasticity of TiAlN.* Materials, 2011. **4**(9): p. 1599-1618.

116. Hörling, A., et al., *Thermal stability of arc evaporated high aluminum-content Ti 1− x Al x N thin films.* Journal of Vacuum Science & Technology A: Vacuum, Surfaces, and Films, 2002. **20**(5): p. 1815-1823.
117. Cunha, L., et al., *Corrosion of CrN and TiAlN coatings in chloride-containing atmospheres.* Surface and Coatings Technology, 1999. **116**: p. 1152-1160.
118. Gunther, M., M. Joemann, and S. Csambor, *Advanced CSP Teaching Materials, Chapter 5: Parabolic Trough Technology*. 2011, Enermena.
119. Jurczak, P., et al., *Efficiency of GaInAs thermophotovoltaic cells: the effects of incident radiation, light trapping and recombinations.* Optics express, 2015. **23**(19): p. A1208-A1219.
120. Romero, M. and A. Steinfeld, *Concentrating solar thermal power and thermochemical fuels.* Energy & Environmental Science, 2012. **5**(11): p. 9234-9245.
121. Lenert, A., et al., *A nanophotonic solar thermophotovoltaic device.* Nature nanotechnology, 2014. **9**(2): p. 126.
122. Bermel, P., et al., *Design and global optimization of high-efficiency thermophotovoltaic systems.* Optics express, 2010. **18**(103): p. A314-A334.
123. Dias, D., et al., *Optical and structural analysis of solar selective absorbing coatings based on AlSiOx: W cermets.* Solar Energy, 2017. **150**: p. 335-344.
124. Nam, Y., et al., *Solar thermophotovoltaic energy conversion systems with two-dimensional tantalum photonic crystal absorbers and emitters.* Solar Energy Materials and Solar Cells, 2014. **122**: p. 287-296.
125. Rinnerbauer, V., et al., *High-temperature stability and selective thermal emission of polycrystalline tantalum photonic crystals.* Optics express, 2013. **21**(9): p. 11482-11491.
126. Rinnerbauer, V., et al., *Low emissivity high-temperature tantalum thin film coatings for silicon devices.* Journal of Vacuum Science & Technology A: Vacuum, Surfaces, and Films, 2013. **31**(1): p. 011501.
127. Nuru, Z., et al., *A Tantalum diffusion barrier layer to improve the thermal stability of AlxOy/Pt/AlxOy multilayer solar absorber.* Solar Energy, 2014. **107**: p. 89-96.
128. Murarka, S. and D. Fraser, *Silicide formation in thin cosputtered (titanium+ silicon) films on polycrystalline silicon and SiO2.* Journal of Applied Physics, 1980. **51**(1): p. 350-356.
129. Niklasson, G., *Materials Science for Solar Energy Conversion Systems, edited by CG Granqvist*. 1991, Pergamon Press, Oxford, UK.
130. *Guide to Using WVASE 32: Spectroscopic Ellipsometry Data Acquisition and Analysis Software*. 2008: J. A. Woollam Company, Incorporated.
131. Miller, O.D., et al., *Fundamental limits to extinction by metallic nanoparticles.* Physical review letters, 2014. **112**(12): p. 123903.
132. Jones, S.B. and S.P. Friedman, *Particle shape effects on the effective permittivity of anisotropic or isotropic media consisting of aligned or randomly oriented ellipsoidal particles.* Water Resources Research, 2000. **36**(10): p. 2821-2833.
133. Tesfamichael, T. and E. Wäckelgård, *Angular solar absorptance of absorbers used in solar thermal collectors.* Applied optics, 1999. **38**(19): p. 4189-4197.
134. Dresselhaus, M., *Solid Sate Physics, Part I, Transport Properties of Solids*. 2001, MIT Press.
135. Granqvist, C.G., *Solar energy materials.* Advanced Materials, 2003. **15**(21): p. 1789-1803.

136. Seitz, F., *The modern theory of solids*. 1940: McGraw-Hill Book Company, Inc; New York.
137. Yacobi, B., et al., *Compound formation between amorphous silicon and chromium.* Journal of Applied Physics, 1980. **51**(12): p. 6424-6425.
138. Locker, L. and C. Capio, *Reaction kinetics of tungsten thin films on silicon (100) surfaces.* Journal of Applied Physics, 1973. **44**(10): p. 4366-4369.
139. Tanaka, T. and K. Kawabata, *Growth kinetics of refractory-metal thin films sputtered by rf-dc coupled magnetron sputtering in Ar or Ne gas plasma.* Vacuum, 1995. **46**(8-10): p. 1059-1062.
140. d'Heurle, F., *Aluminum films deposited by rf sputtering.* Metallurgical and Materials Transactions B, 1970. **1**(3): p. 725-732.
141. Lee, S., et al., *Fabrication of high-quality single-crystal Cu thin films using radio-frequency sputtering.* Scientific reports, 2014. **4**: p. 6230.
142. Schauer, A. and M. Roschy, *RF sputtered β-tantalum and bcc tantalum films.* Thin Solid Films, 1972. **12**(2): p. 313-317.
143. Howell, J., *Deposition, characterization, and thermomechanical fatigue of nickel aluminide and ruthenium aluminide thin films.* 2010.
144. Kylner, C. and L. Mattsson, *Enhanced optical performance of aluminum films by copper inclusion.* Thin solid films, 1999. **348**(1-2): p. 222-226.
145. Bennett, H., M. Silver, and E. Ashley, *Infrared reflectance of aluminum evaporated in ultra-high vacuum.* JOSA, 1963. **53**(9): p. 1089-1095.
146. Gelin, K., T. Boström, and E. Wäckelgård, *Thermal emittance of sputter deposited infrared reflectors in spectrally selective tandem solar absorbers.* Solar energy, 2004. **77**(1): p. 115-119.
147. Sata, N., et al., *Crystallization process of perovskite type oxide thin films deposited by PLD without substrate heating: Influence of sputtering rate and densification-driven high tensile strain.* Solid State Ionics, 2015. **275**: p. 14-18.
148. Tompkins, H.G., *WVASE32® Software Training Manual.* JA Woollam Co., Inc., Lincoln NE, 2006. **210**.